LOCAL MAGNETIC SUSCEPTIBILITY OF THE POSITIVE MUON IN GRAPHITE AND THE QUASI 1D SPIN 1/2 CHAIN CPC

by

Jacques A. Chakhalian

M.Sc., The University of British Columbia, 1995

B.Sc., The St. Petersburg University, 1989

A THESIS SUBMITTED IN PARTIAL FULFILLMENT OF

THE REQUIREMENTS FOR THE DEGREE OF

DOCTOR OF PHILOSOPHY

in

THE FACULTY OF GRADUATE STUDIES

DEPARTMENT OF PHYSICS AND ASTRONOMY

We accept this thesis as conforming

to the required standard

.....

.....

.....

.....

THE UNIVERSITY OF BRITISH COLUMBIA

March 2002

Abstract

The local electronic structure of the positive muon has been investigated in semimetallic graphite using muon spin rotation/relaxation. Both the muon Knight shift and the spin relaxation rate in highly oriented pyrolytic graphite are anomalously large compared to those in simple metals and both have an unusual temperature dependence. These results indicate that a local moment forms around the muon due to the low carrier density. In contrast, measurements on metallic LiC_6 reveal a smaller muon Knight shift which is opposite in sign (negative) and almost temperature independent. We suggest this is due to core polarization of a $Mu^{-}Li^{+}$ complex.

The local magnetic susceptibility around a muon in the quasi one dimensional spin 1/2 antiferromagnetic chain compound CPC has been investigated using muon spin rotation/relaxation. A recent theory by Eggert and Affleck predicts that the local magnetic susceptibility near an impurity in a spin 1/2 chain is dramatically altered compared to the bulk magnetic response. This novel behavior can be attributed to a gapless spectrum of magnetic excitations which characterizes spin 1/2 chain compounds and may be considered the magnetic equivalent of the Kondo effect in metals. In this thesis we compare the local spin susceptibility as measured by the muon spin precession frequency with the bulk magnetic susceptibility measured in a SQUID magnetometer. There is a dramatic difference between the local and bulk magnetic response. In CPC, the perturbation due to the muon is in accordance with theory.

Table of Contents

List of Tables

List of Figures

Chapter 1

Introduction

This thesis presents $\mu\mathcal{SR}$ measurements of the local electronic and magnetic properties of the positive muon in semimetallic highly oriented pyrolytic graphite (HOPG), metallic first-stage lithium intercalated graphite (LiC_6) and in the insulating dichlorobis (pyridine) copper(II) salt (CPC). Although these materials have very different electrical and magnetic properties, there is at least one common feature – they each have a gapless excitation spectrum. This happens to be a key factor in the theory for how a system responds to an impurity. The main purpose of this thesis is to show how this feature affects local properties of a simple impurity such as a positive muon and to compare this behaviour with current theories.

Consider a point-like positively charged impurity in an otherwise perfect lattice. This problem has been the focus of a large number of theoretical and experimental investigations since the original work by Debye and Hückel published almost 70 years ago [1]. The practical interest is of course that even small amounts of impurities can dramatically alter bulk properties. The theoretical interest in the problem is driven by the fascinating cooperative many-body phenomena involved in the screening of such an impurity. Despite the remarkable success achieved in theory, the experimental investigation of this problem by using conventional magnetic resonance techniques is virtually impossible. Here the major difficulty is to find an appropriate technique that has the required sensitivity without requiring a large number of impurities to be present in the sample. Muon spin

rotation/relaxation is an ideal technique to investigate this problem since it has the required sensitivity – typically only one muon is in the sample at a time. Also the positive muon represents a simple point charge disturbance to the system.

Chapter 1 introduces the necessary theoretical background related to the mechanism of screening and local moment formation in metallic media and in addition discusses recent theory for impurities in 1D S=1/2 insulating antiferromagnets. In Chapter 2 the reader is provided with a review of $\mu\mathcal{SR}$ techniques and the muon relaxation mechanisms that have been used to analyze the experimental data. Chapter 3 includes the detailed description of a novel Knight shift apparatus and the electronics associated with it. Chapters 4 and 5 present the experimental results of the $\mu\mathcal{SR}$ frequency shift measurements in graphite and CPC. Chapter 6 provides the reader with a summary of the presented measurements.

1.1 Theoretical Background

1.1.1 General Consideration

The electronic and magnetic properties of an isolated positively charged impurity in a degenerate electron gas have been the subject of numerous theoretical studies because of their fundamental importance. Several independent techniques, including cluster calculations [2],[3], local-density calculations based on the Kohn-Sham formalism [4],[5],[6] and jellium model calculations [7],[8] have revealed the existence of a doubly-occupied bound state for a wide range of metallic densities starting with $r_s > 1.9$ a.u., where $r_s = [\frac{3}{4\pi n_c}]^{1/3}$ is the single electron radius and n_c is the density of carriers. The theoretically predicted bound state is very shallow, being deepest for $r_s \approx 4$ a.u. In principle one could test such theories experimentally by carrying out nuclear magnetic resonance (NMR) on isolated atomic hydrogen in conductors with different carrier concentrations. However, it is not

always possible to dissolve hydrogen in a given conductor. Furthermore, the concentration of hydrogen needed for NMR ($\sim 10^{19}$ cm^{-3}) is in general too high to guarantee isolation from other hydrogen atoms and/or residual impurities.

Alternatively, one can deduce information on isolated atomic hydrogen using the technique of muon spin rotation ($\mu\mathcal{SR}$), in which a positive muon is implanted into the material of interest. The muon (μ^+), is a lepton, an elementary particle which is closely related to the positron from a particle physics point of view since, like the positron, it has no discernible structure. However, the electronic structure around the positive muon in a solid is virtually identical to that of hydrogen because the muon mass, although only 1/9th that of a proton, is still much heavier than that of the electron. For example, the reduced mass for a muonium atom (μ^+e^-) in vacuum is almost identical to that of a hydrogen atom. Muons typically occupy interstitial lattice sites and are normally studied in the infinitely dilute limit – one muon in the sample at a time. Also, because of the short muon lifetime 2.197 μs, they typically remain isolated from residual impurities in the sample. For these reasons, muon implantation is an excellent way to simulate the behaviour of an isolated hydrogenic impurity.

These aspects of the muon have been used extensively in semiconductors, where the muon and its associated paramagnetic centres provide indirect information on isolated atomic hydrogen, a difficult impurity to isolate and study with conventional methods [10]. In intrinsic semiconductors, muonium centres exhibit hyperfine interactions between the unpaired electron and the muon spin which can be used to characterize the local electronic structure. In fact, almost all the information on isolated atomic hydrogen in semiconductors comes indirectly through work on muonium. Studies confirm that the local electronic structure of muonium is virtually identical to that of isolated atomic hydrogen in the few cases where both muonium and hydrogen can be studied [11], [12]. On the other hand, the dynamics of the muon can be very different from those of hydrogen

due to the much lighter mass of the muon.

It is not as easy to obtain equivalent information on muonium in conductive materials where the unpaired electron spin bound to the muon interacts strongly with the conduction electrons. In fact it can be difficult to even verify that a local electronic moment exists in a metallic environment. This is because the large *static* hyperfine fields which typify muonium in non-conductors are generally absent in conductors. Instead the strong exchange interaction between the bound electron on the muon and electrons in the conduction band is expected to mask any obvious signature of muonium. Nevertheless the presence of such a moment should produce detectable residual effects. For example, if a paramagnetic muonium atom exits in a simple metal it should behave as a Kondo impurity [14],[15],[16] and will have a characteristic temperature dependent local spin susceptibility. In this case the muon Knight shift (defined as $(B_{\rm hf} - H)/H$, where $B_{\rm hf}$ is the hyperfine field at the muon site and H is the external magnetic field) should be very large and temperature independent below the Kondo temperature (T_K), where the moment is effectively screened by the conduction electrons. At higher temperatures where the screening cloud is shaken off, the Knight shift should fall as $1/(T + T_K)$. It is interesting to note that in the strong coupling limit of the Kondo model a muonium atom would bind a second electron in a spin singlet state analogous to the Mu^- ion [17]. This may be related to the ground state predicted from density functional theory for a single positive charge in an electron gas [5],[6]. In addition to a large Knight shift one might also expect muonium in a metal to exhibit an unusually large muon spin relaxation (Korringa relaxation) due to the large hyperfine interaction between the muon and the bound electron. This acts to amplify the muon spin-flip scattering with electrons at the Fermi surface [18].

Empirically, the carrier density and location of the muon in the lattice are important factors in determining the behaviour of a local moment around the muon in a conductor.

For example, in metallic alkali metal doped fullerides a vacuum-like muonium atom (μ^+e^-) (endohedral muonium) is stable on the inside of the C_{60} cage. This is evidenced by the characteristic field dependent spin relaxation rate of muonium undergoing rapid spin exchange with conduction electrons at the Fermi surface [19]. The interaction of this local moment with the conduction electrons is very weak, likely due to the low electron density inside the C_{60} cage. In other words, the Kondo temperature is negligibly small and no appreciable screening of the moment is seen. On the other hand muons on the outside of the C_{60} cage (tetrahedral muoniums) do not show any evidence for a local moment. It seems likely that a spin singlet state such as Mu^- is formed for this muon site(s). Such a state may be considered a Kondo impurity but in the strong coupling limit where the electronic moment is heavily screened. Recently paramagnetic muonium has also been identified in heavily doped n-type Si [20] with a carrier concentration in the range $\sim 10^{19}$ cm^{-3}. The magnitude and the temperature dependence of the local spin susceptibility are clear signatures of the same bond-centered muonium seen in intrinsic Si. Furthermore, the simple Curie-like local susceptibility indicates that the Kondo temperature in very small; thus one is in the weak coupling limit. It is interesting to note that the muon-electron hyperfine interaction in heavily doped n-type material is reduced compared to that of the same centre in intrinsic Si, implying that the electronic structure depends on the carrier concentrations. A signal with no appreciable frequency shift was also observed in this experiment; said signal is attributed to the Mu^- ion at the tetrahedral interstitial site. Theoretically this is the predicted stable charge state for muonium/hydrogen in n-type silicon.

One can interpret the results on doped C_{60} and n-type silicon as follows: Depending on the muon site, the Kondo coupling constant $J(T)$ goes from weak to strong. More specifically, for muons at the centre of the C_{60} cage or muons at the centre of the Si–Si bond one is in the weak coupling limit and thus the full moment is seen down to very

low temperatures. This can be understood from a local structural point of view since it may be energetically unfavorable for the muonium atom to bind a second electron, due to the strong onsite Coulomb repulsion. On the other hand, if the muon is at a site where the onsite Coulomb repulsion is not too strong, then muonium can bind a second electron (*e.g.* Mu^-), forming a zero-spin singlet. Under these circumstances the moment is screened until the singlet state is ionized. This would correspond to the strong coupling limit of the Kondo model [17]. In normal metals, where the electron density is

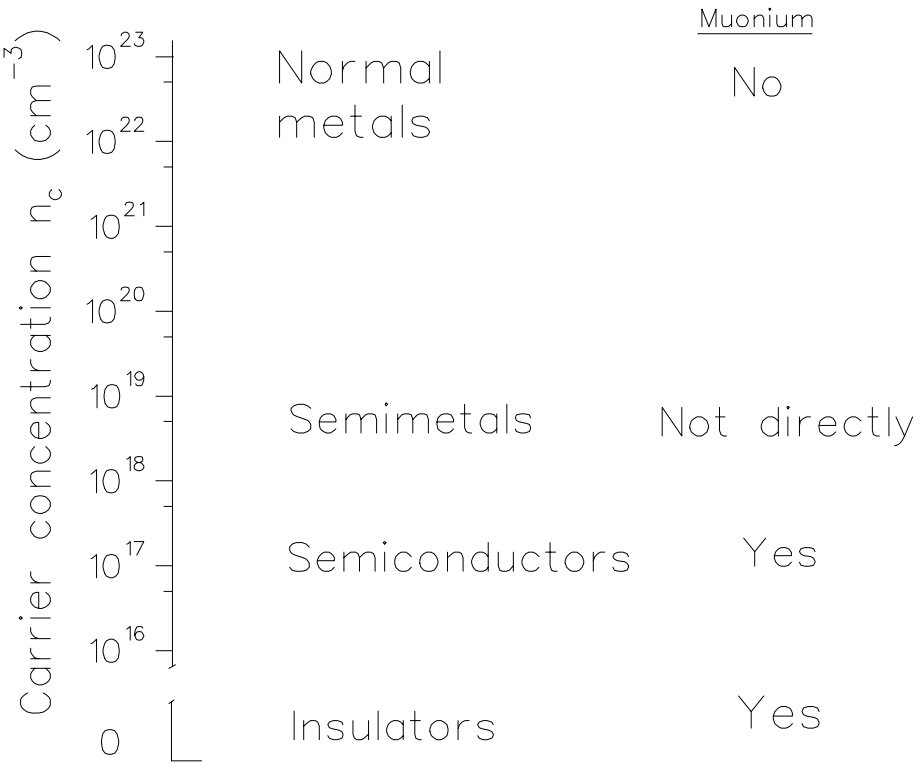

Figure 1.1: The range of carrier concentrations n_c in various groups of material with their characterization with respect to experimentally observed muonium.

much higher ($\sim 10^{22}$ cm^{-3}), no clear evidence of a moment on the muon can be found. For example in silver the muon Knight shift is small, positive (94 ppm) and temperature independent, like the Pauli spin susceptibility. This suggests that the local electronic

structure is a spin singlet (*e.g.* something like the Mu^- ion in which the muon might bind two electrons in a $1s-$like orbit). In the Kondo picture, one is in the strong coupling limit. The observed Knight shift is then attributed to a small overlap between the muon and the polarized conduction electron states at the Fermi surface.

Semimetals lie in an intermediate region between a doped semiconductor, where localized bound states of the muon clearly exist, and good metals, where no such moments are apparent (see Fig.1.1). Although semimetals have carrier concentrations typical of a heavily doped semiconductor, at low temperatures they have a well defined Fermi surface. For example, at low temperatures they exhibit de Haas–van Alphen (dHvA) oscillations of the magnetic susceptibility from Landau levels crossing the Fermi surface. On the other hand, at relatively moderate temperatures (above 50 K) they cannot be considered a degenerate electron gas since k_BT becomes comparable to the small Fermi energy. Indeed, in the semimetal antimony the muon Knight shift is anomalously large at low temperatures [21] and has a temperature dependence which follows qualitatively what one expects for a simple Kondo impurity up to about 100 K [22].

1.1.2 Screening in Metallic Media

It is clear that the presence of freely moving charges dramatically alters the charge screening around a positive impurity compared to an insulator. From the classical electrodynamics standpoint we know that there is no macroscopic electric field inside a metal; thus a single positive charge must be effectively screened within a few angstroms. To quantify this statement, we will briefly review the main results of the Thomas-Fermi (T-F) theory of screening in three dimensions [23].

The semi-classical Thomas-Fermi approximation describes the static response ($\omega = 0$) at long wavelengths ($k \ll k_F$), which corresponds to a slowly varying potential $\phi(\boldsymbol{r})$ as a function of position $\boldsymbol{r}$ relative to the impurity charge. In this limit, the dielectric function

can be approximated by

$$\epsilon(k,\omega=0)_{\mathrm{T-F}} = 1 + \frac{k_{\mathrm{T-F}}^2}{k^2} \tag{1.1}$$

where $k_{\mathrm{T-F}} = \sqrt{\frac{e^2}{\epsilon_o \epsilon}\frac{dn}{d\mu}}$ is the Thomas-Fermi screening wave number,

$$\frac{dn}{d\mu} = \int g(E)\frac{\partial f(E-\mu)}{\partial \mu}dE = \int g(E)\left(-\frac{\partial f(E-\mu)}{\partial E}\right)dE \tag{1.2}$$

is the thermodynamic density of states,

$$f(E-\mu) = \frac{1}{\exp[(E-\mu)/k_B T]+1} \tag{1.3}$$

is the Fermi-Dirac distribution, n is the electron density, μ is the chemical potential and $g(E)$ is the density of states.

Now consider the screening of a positive charge. The screened potential is just the bare Coulomb potential divided by $\epsilon_{\mathrm{T-F}}(k,\omega=0)$:

$$V_{\mathrm{scr}}(\boldsymbol{k}) = -\frac{e^2}{\epsilon_o \epsilon}\frac{1}{\boldsymbol{k}^2 + \boldsymbol{k}_{\mathrm{T-F}}^2}. \tag{1.4}$$

The real space potential is given by the Fourier transform of this potential,

$$V_{\mathrm{scr}}(\boldsymbol{r}) = -\frac{e^2}{4\pi\epsilon_o \epsilon}\frac{\exp(-\boldsymbol{k}_{\mathrm{T-F}}\cdot\boldsymbol{r})}{|\boldsymbol{r}|}, \tag{1.5}$$

and has the same form as the Yukawa potential in nuclear physics. The important feature of this potential is that the long-range nature of the bare Coulomb potential is *exponentially* suppressed with a screening length scale of $l_{\mathrm{scr}} = 1/k_{\mathrm{T-F}}$.

At low temperature where the distribution of electrons is highly degenerate, $f(E,\mu) = \Theta(\mu - E)$ and its derivative with respect to E is the delta function $-\partial f/\partial E = \delta(E-\mu)$, Eq.(1.2) can be written as $dn/d\mu = g(\mu)$. In this limit the thermodynamic density of states is equal to the density of states $g(E)$ taken at the Fermi level E_F and

$$l_{\mathrm{scr}} = 1/k_{\mathrm{T-F}} \approx 0.5\left(\frac{n_c}{a_B^3}\right)^{-1/6} \qquad \text{(3D free electron gas)} \tag{1.6}$$

where $a_B = 0.529$ Åis the Bohr radius [23]. For a typical metal (*e.g.* Cu) Eq. (1.6) gives $k_{\mathrm{T-F}}^{-1} \approx 0.54$ Å. This indicates that the Coulomb potential range is cut off within a lattice parameter. In a semiconductor, the screening length can be considerably longer because the carrier concentration is much smaller; for a typical value of $n_c = 10^{14}$ cm^{-3}, $k_{\mathrm{T-F}}^{-1} \approx 16.8$ Å. The opposite limit is at high temperature and low carrier density, where the electron gas is non-degenerate and follows the Boltzmann distribution. In this case $dn/d\mu = n_c/k_BT$ and

$$k_{\mathrm{D-H}} = \sqrt{\frac{e^2}{\epsilon_o \epsilon} \frac{n_c}{k_B T}} \tag{1.7}$$

This limit is also known as the Debye-Hückel screening limit [1].

It is also interesting to ask what happens in the simple quantum mechanical problem of a free electron moving in the impurity potential when the screening length l_{scr} gets long. The impurity potential $V(\boldsymbol{r})$ then correspondingly deepens and one can expect that it will be able to bind an electron, *i.e.* the electron 'pops out' of the continuum into an orbital bound to the impurity site. In poor metals (*e.g.* YBCO) and semimetals (*e.g.* graphite or antimony), the decreasing number of carriers will increase the screening length and this in turn will extend the range of the impurity potential to the extent that it may be able to trap or bind an electron.

Historically, the first result which was not based on the T-F approximation was the erroneous prediction by Mott about the absence of a bound state on a proton. Later, Sach and Goepert-Mayer concluded that a bound state is still possible if the *electron-electron* interaction is taken into account. A further refinement to the original T-F calculations was done within the Lindhard [24] approximation and within the random phase approximation (RPA), both predicting a lesser degree of screening and an oscillating structure at larger distances from the impurity. Since the Thomas-Fermi approximation is a long range approximation it cannot adequately describe the response of the electron gas to a

short-range perturbation caused by a point-like charge. In order to get a more accurate description, Lindhard replaced the T-F dielectric function $\epsilon(k,0)_{\mathrm{T-F}}$ with

$$\epsilon_L(k,0) = 1 - \frac{k_{\mathrm{T-F}}}{k^2}\mathcal{F}\Big(\frac{k}{2k_F}\Big) \tag{1.8}$$

$$\text{where} \qquad \mathcal{F}(z) = \frac{1-z^2}{4z}\log|\frac{1+z}{1-z}| + \frac{1}{2}$$

and obtained the following expression for the screened impurity potential

$$V_{\mathrm{scr}}(\boldsymbol{r}) \propto \frac{x}{(2+x^2)^2}\frac{\cos(2\boldsymbol{k}_F\boldsymbol{r})}{\boldsymbol{r}^3} \tag{1.9}$$

where $x = k_{\mathrm{T-F}}/(2k_F)$ and k_F is the Fermi momentum. The main feature of this potential is the oscillatory $1/r^3$ behaviour also known as Freidel or RKKY oscillations [25]. Ultimately they originate from the sharp cut-off of the Fermi surface.

The common problem with all the calculations mentioned above is in the assumption that only conduction electrons contribute to the screening cloud. However, it is clear that if an electron becomes localized into a bound state with the impurity then the interactions it experiences are very different from those of the free electrons. Thus, in order to develop a proper screening theory, one must abandon the simplified single-particle approximation and take into account collective *many-body* effects present in the bound state as well as the extended nature of all electron states within the conduction band in a self-consistent way. Cluster calculations [2],[3], density-functional calculations based on the Hohenberg-Kohn-Sham formalism [26] , and the 'jellium' model provide a foundation for the present theoretical understanding of the screening problem.

In the early eighties, Popovic and Scott [4] and Almabladh and von Barth [27] published the first results which included the non-linear response to screening on a proton within the local-density formalism. Despite the differences in calculation procedures the results are in complete agreement: namely, in contrast to the conventional linear response models, the pile-up charge increases with decreasing r_s ($r_s = [\frac{3}{4\pi n_c}]^{1/3}$) and the proton

is typically screened within 0.6 a.u. independently from r_s in the metallic range of densities. Also, all models predicted a *very shallow doubly-occupied bound state* that can be regarded as a heavily screened hydrogen ion H^-. Furthermore, the hydrogen-like H^o solution in metals is *always* found to have higher total energy compared to that of H^-. Note that an extra electron attached to this shallow bound state is screened by the low energy and hence the long wavelength electrons from the bottom of the conduction band. Because of this, the screening cloud is rather extended and broadened even further by the collisions with itinerant electrons. For this reason, this state should be regarded as a shallow *resonance*. At the same time, in a different area of condensed matter physics,

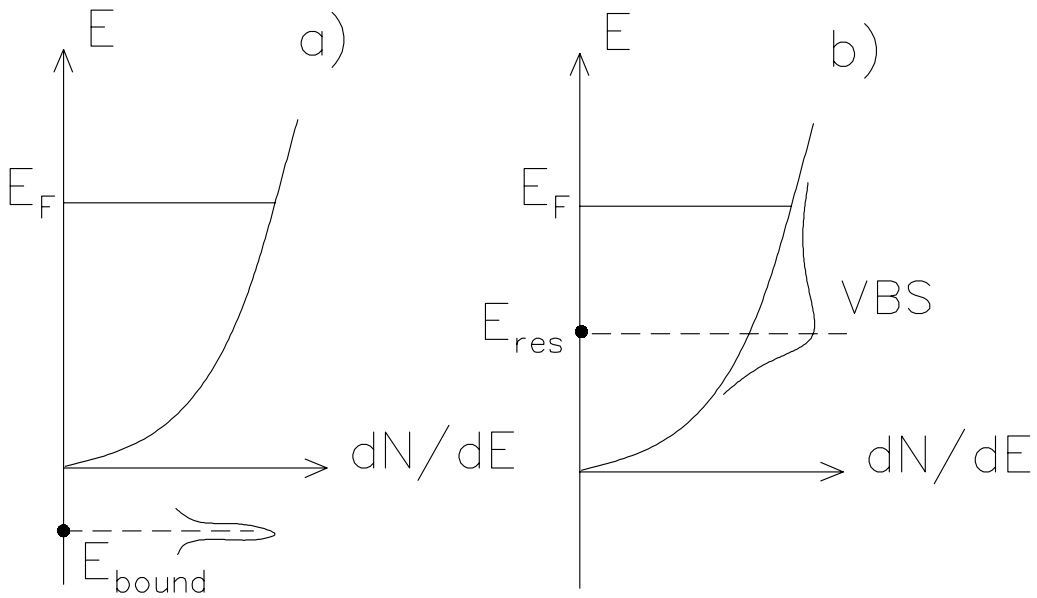

Figure 1.2: When the localized state is formed below the continuum of conduction electrons we have a bound state. However, if the state is *within* the continuum then it is more appropriate to view this state as a broad resonance or a virtual bound state (VBS).

a remarkably similar concept of *the virtual bound state* (VBS) was developed to explain the transport properties of transition and rare earth metals diluted in a non-magnetic host. The idea of VBS is based on the assumption that if the local impurity potential is

not sufficient to bind an electron below the conduction band then the electron still can be localized for a limited period of time in the vicinity of the impurity. This model also predicted that the effect of resonance scattering would induce a rather narrow peak in the density of states, also known as the VBS resonance. Fig. 1.2 illustrates the concept of VBS that if occurs close to the Fermi surface may contribute significantly to specific heat and resistivity.

1.1.3 Local Moment Formation - Kondo Effect

So far we have considered the results influenced by the impurity charge alone. However in a real metal, spin degrees of freedom are as important as the charge and under certain conditions may even modify the properties of the host itself. One of the examples where such a modification occurs is when an impurity with an electronic moment is submerged into a non-magnetic host. Because the calculations described in Sec. 1.1.2 unambiguously predict that the stable state for a hydrogen atom in metals is H^- the problem of how the local moment 'survives' in the metallic environment is of great interest. The theoretical framework for understanding of the local moment phenomena in a non-magnetic host was put forward by Anderson and later became known as the Anderson model [28]. The model is described by the following Hamiltonian

$$\mathcal{H}_A = \sum_{\mathbf{k}s} \epsilon_{\mathbf{k}} c^\dagger_{\mathbf{k}s} c_{\mathbf{k}s} + \epsilon_o \sum_s c^\dagger_{ds} c_{ds} + \frac{U}{2} \sum_s n_{ds} n_{d-s} + V \sum_{\mathbf{k}s} (c^\dagger_{ds} c_{\mathbf{k}s} + c_{\mathbf{k}s} c^\dagger_{ds}) \qquad (1.10)$$

where $n_{ds} = c^\dagger_{ds} c_{ds}$ is the number of electrons on the impurity site and c_{ds} and $c^\dagger_{ds}$ are the creation and annihilation operators. Because of its importance we describe the model in detail. For simplicity, we consider a non-magnetic metallic system (*e.g.* Al) with a single $3d-$transition metal ion (*e.g.* Fe or Ni) with only one spin-up $3d$ electron. First, Anderson introduced a U term which is the increase in the electron energy if another spin-down electron already occupies the same $3d$ orbital. He also noted that in the atomic $3d$

orbitals the Coulomb repulsion can be rather large and is of the order of 30 eV. In normal metals because of the screening and delocalization effects this value is reduced to 1-7 eV and is still large compared to other interactions. The matrix element V from the last term from Eq.(1.10) describes the mixture between the $3d$ electron and the conduction electron entering or escaping the $3d$ orbital. Based on this Hamiltonian Anderson predicted that the local moment formation occurs when the following conditions are satisfied (see Figs. 1.3 and 1.4):

$$\epsilon_o + U \gg E_F \qquad \text{and } \epsilon_o \ll E_F \tag{1.11}$$

$$|\epsilon_o + U - E_F| \gg \Delta \qquad \text{and } |E_F - \epsilon_o| \gg \Delta \tag{1.12}$$

where ϵ_o is the energy of the $3d$ orbital and Δ is the resonance state width. Since the

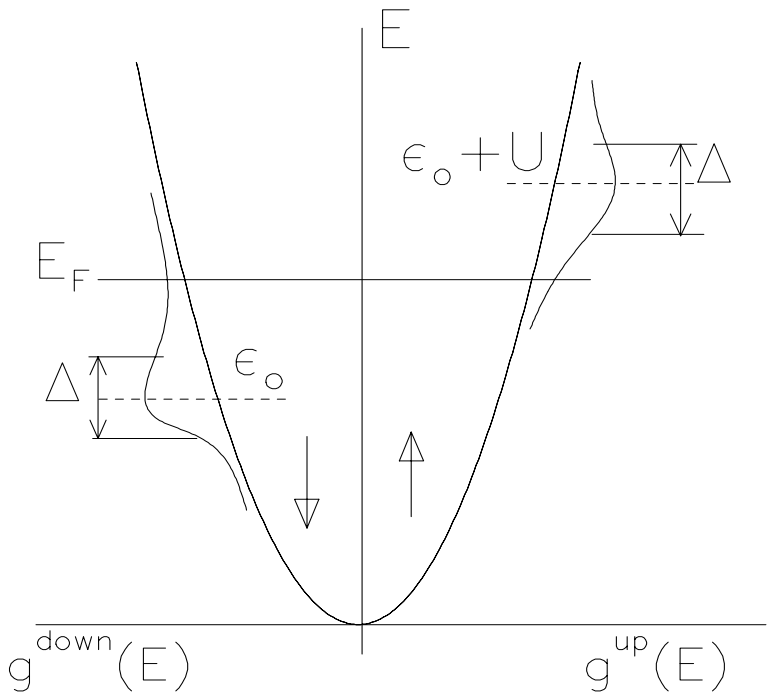

Figure 1.3: Anderson model of local moment formation (from Ref.[28]).

second spin-up electron has energy $\epsilon_o + U$ this state is not occupied and therefore only

the spin-up electron fills in the $3d$ orbital resulting in the local moment formation. On the other hand, if both ϵ_o and $\epsilon_o + U$ levels are above or below the Fermi level E_F the local moment will not appear (see Fig. 1.4). The effective exchange coupling between the localized spin and the conduction electrons can be expressed in terms of U and V and is found to be negative. The width Δ of the virtual (or resonance) bound state depends on the density of states at the Fermi level of the host metal and the value of mixing V as $\Delta \propto \pi V^2 g(E_F)$. Anderson also introduced the $\pi\Delta/U$ ratio. He showed that if this ratio is less than unity then the local moment will form. The magnetic susceptibility of a magnetically

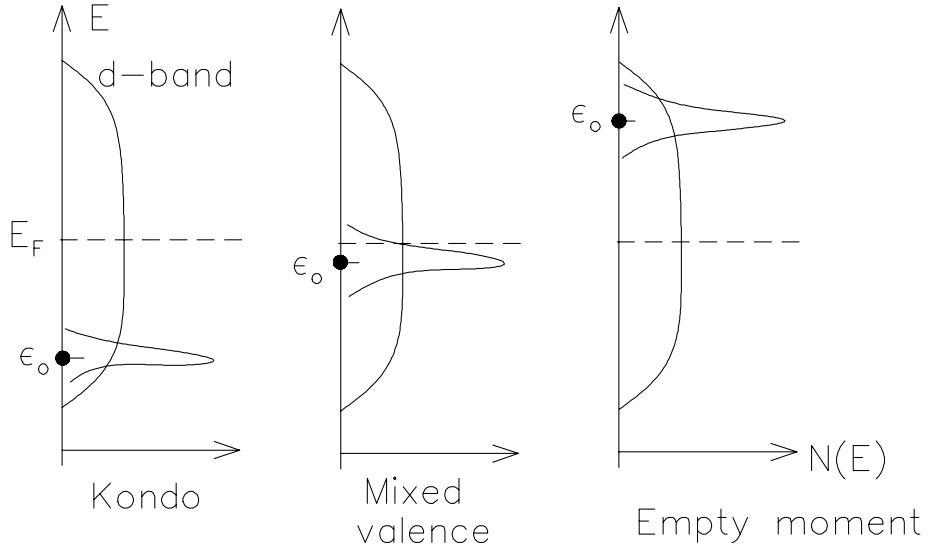

Figure 1.4: Different regimes of the Anderson model depending on a position of a bare level ϵ_o and a magnitude of the U term. In Kondo regime ($\epsilon_o \ll E_F$) a large moment forms at high T but is screened at low T. In the mixed valence regime, the occupancy of the impurity level is fractional and moment formation is marginal. In the case of $\epsilon_o > E_F$ the impurity level is empty and no local moment forms.

dilute alloy as a function of temperature and the U energy was calculated later by Kondo [30]. Obviously, the local moment will not appear if U=0 and the susceptibility will be temperature independent reflecting the Pauli paramagnetism ($\chi_s = N(E_F)\mu_B^2$). When

U becomes larger and the ratio $\pi\Delta/U < 1$ a localized moment will appear and the magnetic susceptibility will follow the Curie law. However, as the temperature is lowered the local moment will disappear due to the dynamic screening involving the interaction with conduction electrons and the localized spin (see Fig.1.5).

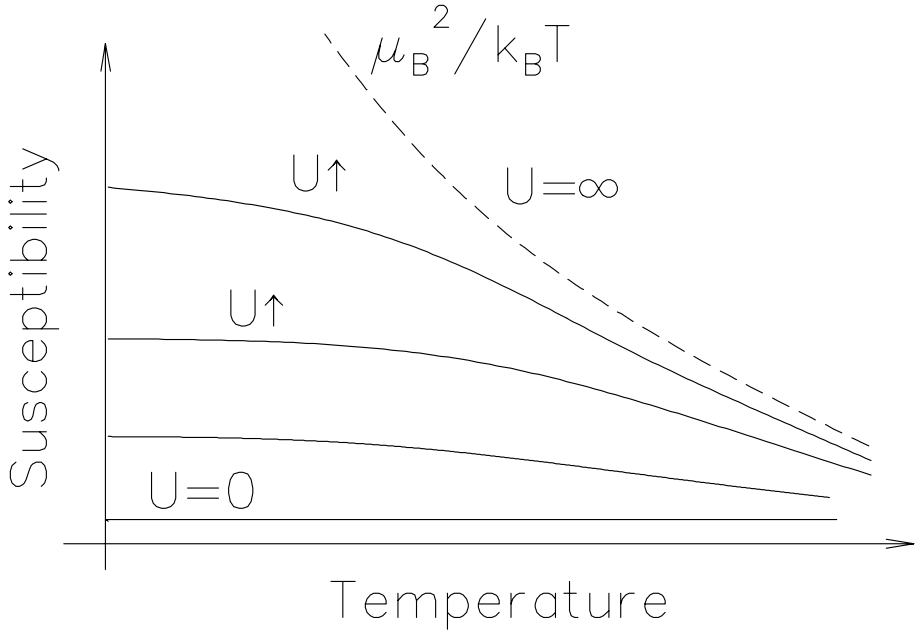

Figure 1.5: Temperature dependence of magnetic susceptibility as a function of the Coulomb energy U. From ref. [30].

In 1964, Kondo used a concept similar to the Anderson model to explain the existence of a resistivity minimum in metals at low temperatures. Later, the model became known as the $s-d$ or Kondo model and is based on the Kondo exchange Hamiltonian [29]

$$\mathcal{H}_K = \sum_{\mathbf{k}s} \epsilon_{\mathbf{k}} n_{\mathbf{k}s} - J(\boldsymbol{R}-\boldsymbol{r})\boldsymbol{S}(\boldsymbol{R}_d)\cdot\boldsymbol{s}(\boldsymbol{r}) \tag{1.13}$$

where $\boldsymbol{s}(\boldsymbol{r})$ is the conduction electron spin density on the impurity located at point $\boldsymbol{R}$, $\boldsymbol{S}(\boldsymbol{R}_d)$ is the impurity spin and $J(\boldsymbol{R}-\boldsymbol{r})$ is the electron-impurity coupling constant. In this approximation a local moment is antiferromagnetically coupled to the conduction

electrons *via* the exchange interaction J as illustrated in Fig. 1.6. Among the noteworthy results of this model are:

- Within a certain range of parameters there exists a local moment region which is indicated by the Curie like susceptibility

$$\chi(T \gg T_K) \propto \frac{1}{4}\frac{(g\mu_B)^2}{k_B T} \tag{1.14}$$

- At very low temperatures the local moment is always compensated by the itinerant electrons.

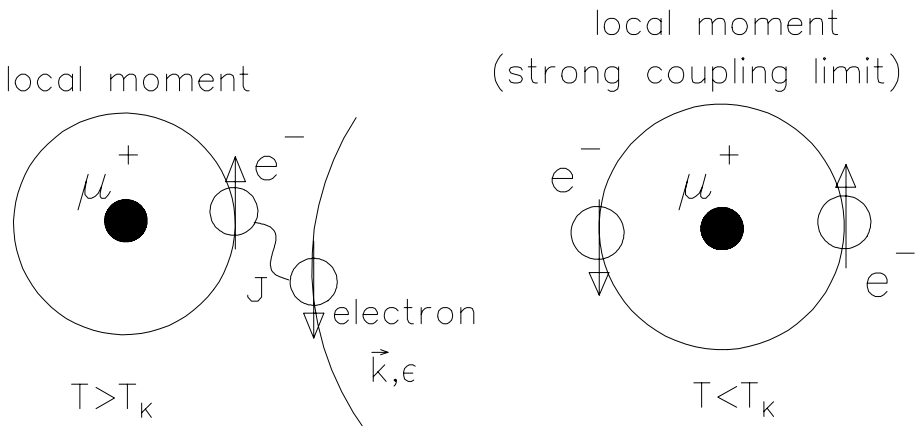

Figure 1.6: Local moment formation in strong coupling limit. At high temperatures a local moment scatters the itinerant electrons. When the temperature decreases the interaction between the impurity and conduction electrons increases eventually leading to the spin-singlet bound state formation at $T \ll T_K$.

Later it was shown that the Kondo model is a special case of the Anderson model with an appropriate choice of the U parameter and $J = 2V^2/\epsilon_o$. At the same time the original Anderson model was proven to be inadequate at low temperatures where the perturbative calculations are not valid anymore. The characteristic temperature T_K which separate a perturbative regime from the non-perturbative is called the Kondo temperature. The

understanding of the region below T_K was achieved later by Anderson and coworkers by applying ideas of scaling. The scaling argument revealed that as the temperature is lowered below T_K, the coupling J will increase and for $T \to 0$ K $J \to \infty$. In this *strong-coupling limit*, the ground state for the system is a singlet (*e.g.* non-magnetic impurity + $[e^{\uparrow}e^{\downarrow}]$, where arrows up and down indicate the itinerant electron spin direction, see Fig. 1.6) and thus the local moment is effectively quenched which in turn implies $\chi(T \to 0) = 0$. For the rest of the conduction electrons the local moment in the ground state acts as a *non-magnetic* impurity with infinite repulsive potential.

However, the transport measurements in alloys with rare-earth and transition ions unambiguously demonstrated that even at very low temperatures the magnetic susceptibility $\chi(T)$ is not zero and approaches a small but finite value. This contradiction with the experiments is removed if the residual magnetic excitations to the triplet excited state are taken into account. The impurity singlet has become polarizable which gives rise to the impurity-induced electron-electron interaction. An independent confirmation of those results was provided by Wilson [31] within the 'numerical renormalization group' approximation, who studied the low energy excitations of a many-body system on the simplified Anderson model. With the power of renormalization technique Wilson confirmed that if the impurity-electron interaction $-J\boldsymbol{S}_d \cdot \boldsymbol{s}$ is characterized by the coupling

$$J = 2 \mid V \mid \frac{U}{E_{\rm res}(E_{\rm res} + U)} \tag{1.15}$$

which is antiferromagnetic because $E_{\rm res} < 0$ then above T_K the susceptibility $\chi(T)$ is Curie-Weiss like with a reduced effective moment

$$\chi(T) \simeq 0.17 \frac{(g\mu_B)^2}{k_B} \frac{1}{T + 2T_K} \qquad \text{for } T_K < T < 20T_K \tag{1.16}$$

whereas below T_K the local moment is compensated and the impurity susceptibility $\chi(T)$

reaches the following limit

$$\lim_{T\to 0} \chi(T) = 0.103(g\mu_B)^2/k_B T_K \tag{1.17}$$

$$k_B T_K \propto D(g(E_F)J)^{1/2} e^{-1/g(E_F)J} \tag{1.18}$$

where $g(E_F)$ is the density of state at the Fermi level and g is the electron $g-$factor.

Another particularly important approximation based on the Fermi liquid theory was developed by Nozieres [32] and Yamada [33]. In this approximation, the Landau phenomenology was successfully applied to the impurity problem below T_K and allowed one to calculate the various transport properties, magnetic susceptibility and specific heat. Nozieres showed that that the low temperature properties are significantly affected by the impurity which produces a phase shift for the conduction electrons that reaches $\delta_o(\boldsymbol{k}_F) = \pi/2$ at the Fermi energy E_F. On the other hand, the most recent theoretical efforts have been focused on obtaining *rigorous* results pioneered by the work of Wiegmann [34] and Andrei [35]. One of the most remarkable features of these calculations is that the termodynamic properties of the Kondo system only depend on a single energy scale given by the Kondo temperature T_K. Also a different approach based on the renormalization group improved perturbation theory was recently developed by Affleck and co–workers [36],[37] and shed new light on the nature of a screening cloud, its size and interior dynamics.

1.1.4 μ^+ Screening

Self-consistent theoretical treatment of the local moment formation specific to the muon was developed by Jena and Singwi [38], Ellis and Lindgren [39] and Estreicher and Meier [40] within the 'jellium' model framework. The most surprising result of their investigation is that the local enhancement of spin density on μ^+ does not scale with the charge density. Figure 1.7 illustrates the difference. The somewhat oversimplified 'jellium'

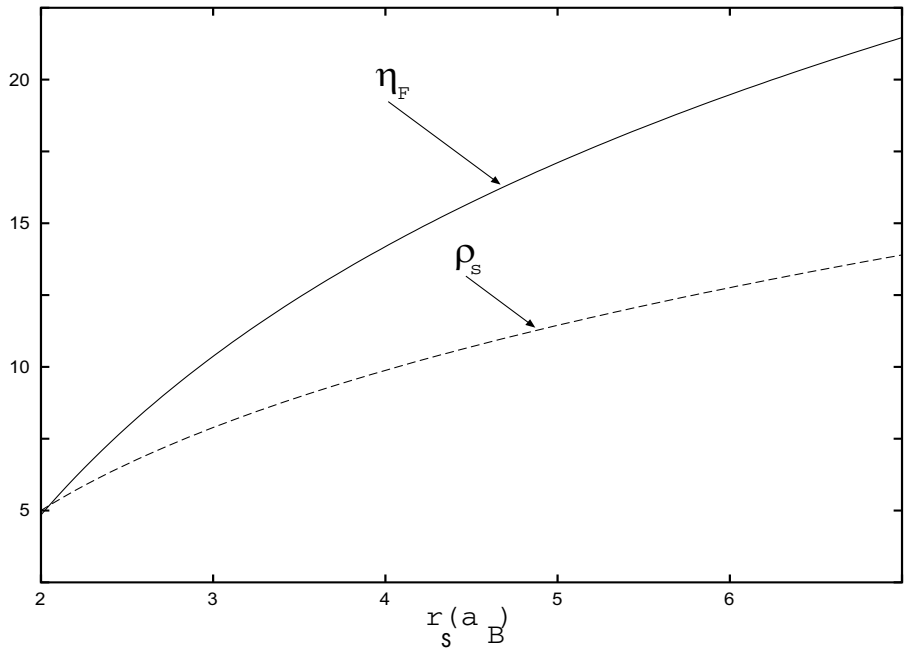

Figure 1.7: The spin $\rho_s(\boldsymbol{r}_\mu)$ density and the charge density $\eta_F(\boldsymbol{r}_\mu) = \Omega_e\langle|\ \psi(\boldsymbol{r}_\mu)\ |^2\rangle$ enhancement factors *v.s.* the electron spin density. From ref. [9].

model was refined later by the microscopic cluster calculations and the band structure techniques developed by Mainwood and Stoneham [41], Adachi and Keller [42] and by Gellat [43], Gupta and Freeman [44], Klein and Pickett [45] and others. In complete agreement with the generalized calculations for a proton and hydrogen diluted in metals, the muon calculations revealed that:

- Muon spin density enhancement

$$\rho_s(\boldsymbol{r}_\mu) = [n^+(\boldsymbol{r}_\mu) - n^-(\boldsymbol{r}_\mu)]/(n_o^+ - n_o^-) \tag{1.19}$$

  (where $n_o^\pm$ are the unperturbed spin densities and $n^\pm(\boldsymbol{r}_\mu)$ are the perturbed spin densities on the muon) does not scale linearly with the charge density $\eta_F(\boldsymbol{r}_\mu)$ enhancement.

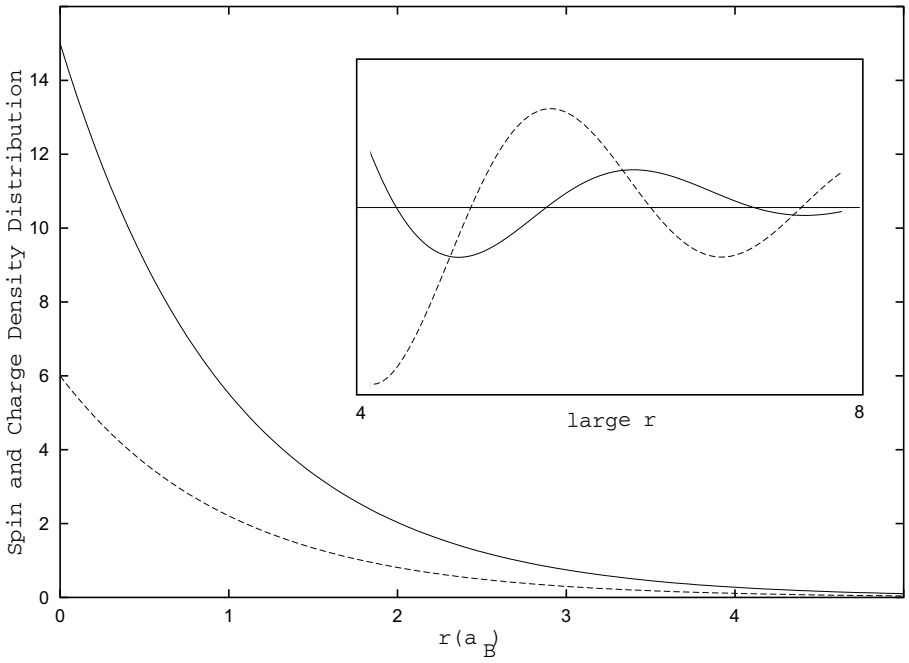

Figure 1.8: The total charge and spin densities around the muon according to the 'jellium' model calculations in an applied magnetic field. The solid line represents the charge density. From ref. [38].

- The difference between $\rho_s(\boldsymbol{r}_\mu)$ and $\eta_F(\boldsymbol{r}_\mu)$ increases with r_s (see Fig 1.8).
- At low carrier concentration such that $r_s > 1.9$ a.u. ($r_s \propto n^{-1/3}$) the shallow bound state forms. No bound state was found below this threshold value.
- Above $r_s > 1.9$ a.u. the contribution to the total spin density from core polarization can be rather large and *negative* in sign.

1.1.5 Impurities in 1D S=1/2 Antiferromagnets

Recent theoretical work [46],[47] on 1D spin 1/2 AFM chains suggests that there is a strong connection between behaviour of an impurity in such a system and in a normal metal. Although the physics of a spin chain has been a traditional testing ground for

theorists for the past few decades, only recently with advances in conformal field theory it has become possible to calculate the correlation functions, the low energy excitation spectrum and the effects imposed by an impurity [48]. These results based on a theory of conformally invariant boundary conditions revealed an unexpected behaviour in a S=1/2 antiferromagnetic chain interacting with a *non-magnetic* single charge impurity.

Traditionally, the magnetic properties of 1D S=1/2 AFM insulators are well described by the Heisenberg model with anisotropic exchange coupling between the ion spins. By neglecting the interchain coupling, the model Hamiltonian can be written as

$$\mathcal{H} = \sum_{i=1}^{l-1} \left(\frac{J}{2}(S_i^+ S_{i+1}^-) + J_z S_i^z S_{i+1}^z \right) \tag{1.20}$$

where S_i^+ and S_{i+1}^- are the S=1/2 raising and lowering operators at site i, l is the total number of sites and J is the intrachain coupling taken to be positive. However, unlike S=1 quasi 1D chains where low-energy magnetic excitations exhibit a well known Haldane gap, these systems can only have a *gapless* spectrum of magnetic excitations. The interesting quantum critical phenomena occur when the gapless bulk excitations interact with a single quantum impurity. For example, it has been shown [49] that the effects of a non-magnetic impurity can propagate deep into the chain a distance which is essentially determined by the strength of coupling J between neighboring ions. It is also predicted that any generic and not site-symmetric perturbation should result in a renormalization to the completely broken chain. On the other hand, for the site-parity symmetric perturbation where two adjacent links are equally weakened (see Fig. 1.9), the impurity effect is considered to be irrelevant and the chain effectively 'heals' itself as $T \rightarrow 0$.

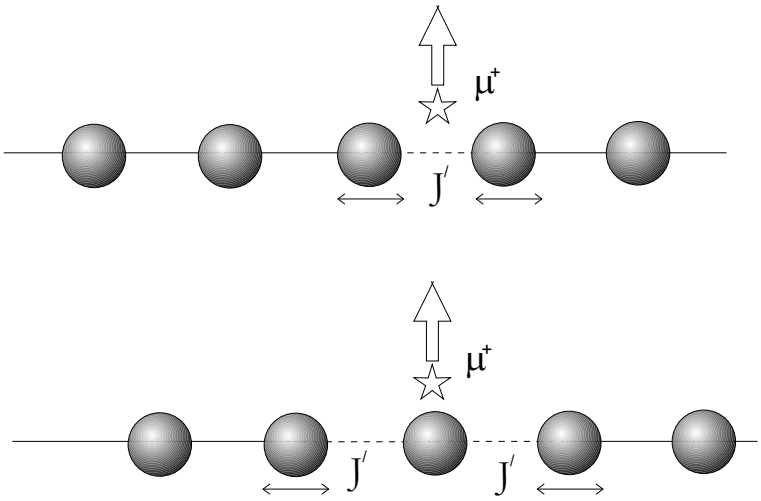

Figure 1.9: Top: A quantum spin chain with one altered link. Bottom: A quantum spin chain with two altered links. The possible position of the muon is indicated by the arrow.

From the experimental point of view, the impurity effects will modify the local susceptibility at any site i of the chain

$$\chi_i(T) = \frac{\partial \langle S_i^z \rangle}{\partial H}|_{H=0} = \frac{1}{T}\sum_j \langle S_j^z S_i^z \rangle \tag{1.21}$$

where H is the applied magnetic field and $g\mu_B = k_B = 1$. Clearly, this local susceptibility is very different in the bulk and near the perturbed site since the open ends are more susceptible. As follows from the mean field theory [49], in the case of a completely broken chain, the local susceptibility has a non-zero alternating part which is a function of the site index i and temperature

$$\chi(i,T) = \chi_{\text{uni}} + (-1)^i \chi_{\text{alt}} \qquad . \tag{1.22}$$

Perhaps, the most unexpected theoretical result is a large magnitude of the alternating part of the susceptibility in the completely broken chain (*i.e.* $J' = 0$ as shown in Fig. 1.10a). The theoretically predicted staggered part of the susceptibility is analogous to

Freidel oscillations, but for a Heisenberg S=1/2 chain these oscillations *increase* as one goes away from the impurity location. This oscillating behaviour is observed to be present even for small perturbations of one link (see Fig. 1.10b).

In a $\mu\mathcal{SR}$ experiment the positive muon charge should perturb the spin 1/2 chain. Furthermore, the frequency shift should be a direct measure of the local spin susceptibility which can be compared with the theory. The local magnetic field $\boldsymbol{B}_{\rm loc}(\boldsymbol{r}_\mu)$ at the muon site is given by the sum of the dipolar fields from all spins of the chains and by the contact hyperfine field $\boldsymbol{B}_c(\boldsymbol{r}_\mu)$ on the muon

$$\boldsymbol{B}_{\rm loc}(\boldsymbol{r}_\mu) = \Big(\boldsymbol{z} + \sum_j \frac{3\boldsymbol{r}_j[\boldsymbol{r}_j \cdot \boldsymbol{z}\chi_j] - \boldsymbol{z}\chi_j}{|\boldsymbol{r}_j^3|}\Big) H^z + \boldsymbol{B}_c(\boldsymbol{r}_\mu). \tag{1.23}$$

Equation (1.23) is simplified if one performs measurements on a powdered sample where the dipolar part of the local field $\boldsymbol{B}_{\rm loc}(\boldsymbol{r}_\mu)$ averages to zero and the frequency shift will depend only on the contact hyperfine field $\boldsymbol{B}_c(\boldsymbol{r}_\mu)$.

Recently it became possible to study the effects of the muon perturbation using quantum Monte-Carlo (QMC) simulations. The theoretically predicted curves are shown in Fig. 1.11 in comparison to the unperturbed chain susceptibility. Few observations are in order:

- Because of the renormalization effects, a characteristic maximum observed in the unperturbed d.c. susceptibility is shifted down to lower temperatures and the overall susceptibility is increased.

- The location of the maximum and a ratio of the maximum and the zero temperature susceptibility indicate the perturbation strength.

- For strong perturbations the maximum vanishes completely as shown in Fig. 1.11a.

A special case of the site-parity symmetric perturbation was also theoretically studied by modeling it with two perturbed links. In this case the logarithmic impurity susceptibility

at the origin is dominant at low temperatures and the alternating susceptibility χ_{alt} only plays a secondary role. Because of this, the resulting muon signal will effectively measure the $\ln(T)$ behaviour which has been predicted for the two channel Kondo effect (see below).

The impurity problem in 1D S=1/2 AFM chains has also been studied in a different context, namely in its relationship to the Kondo problem in normal metals [47],[51]. The theoretical description of impurities in a chain can be translated into the Kondo problem by direct mapping the perturbed link coupling constant J' to the Kondo coupling $J(T)$. Then the two ends of the completely broken chain can be described by the two-spin (two–channel) Kondo problem and a semi-infinite chain with an open-end spin coupled to the impurity is identified with the single–channel Kondo problem. These analogies are very important since they allow to apply theoretical models and techniques developed for 1D insulating spin chains to the Kondo problem in metals.

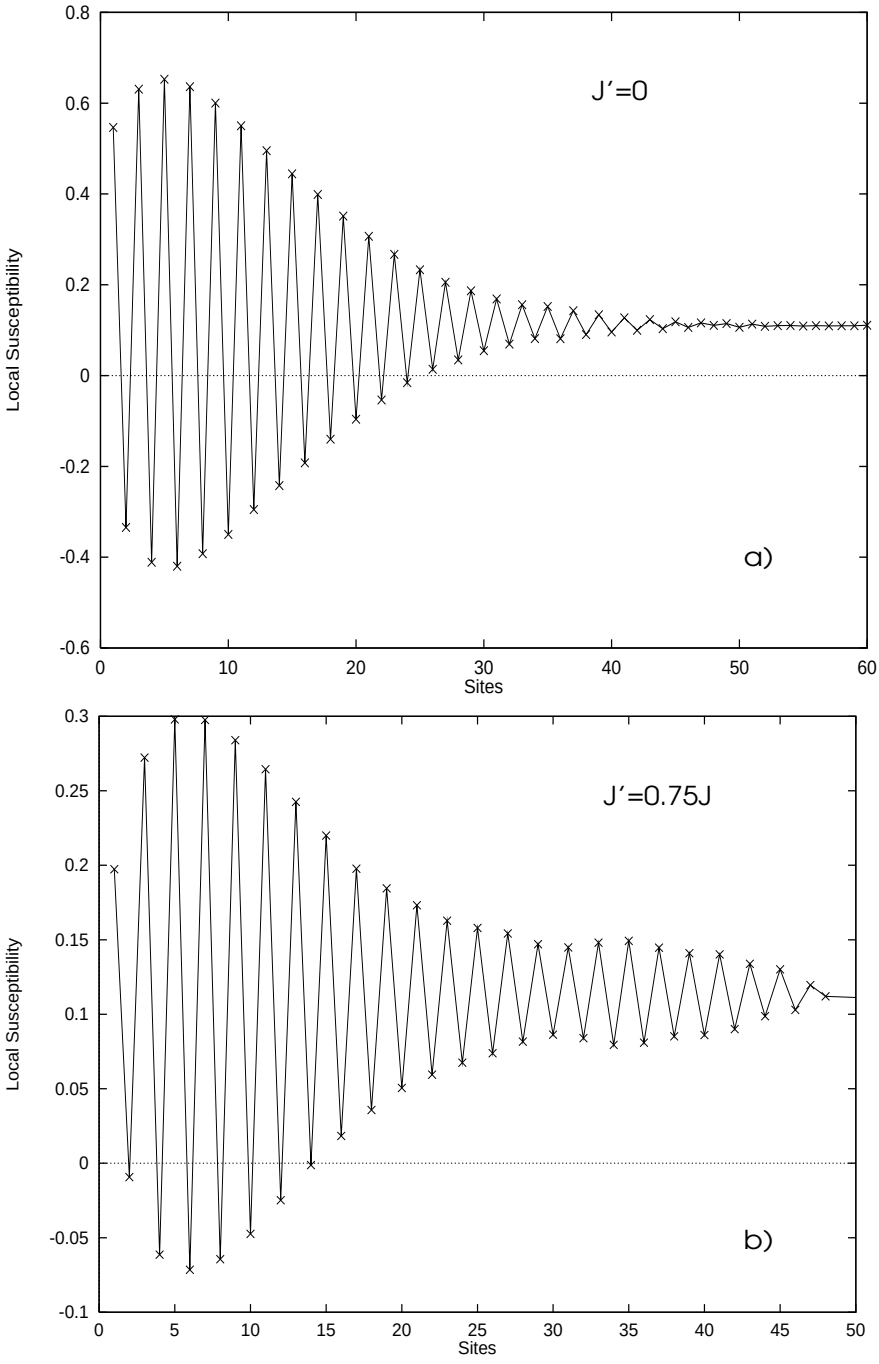

Figure 1.10: a) The local susceptibility near an open end from a Monte Carlo simulation for $\beta = 1/T = 15/J$ and $J' = 0$. b) The local susceptibility near open ends; a Monte Carlo simulation for $\beta = 15/J$ and $J' = 0.75J$ (from Ref. [52]). Crosses are the QMC data.

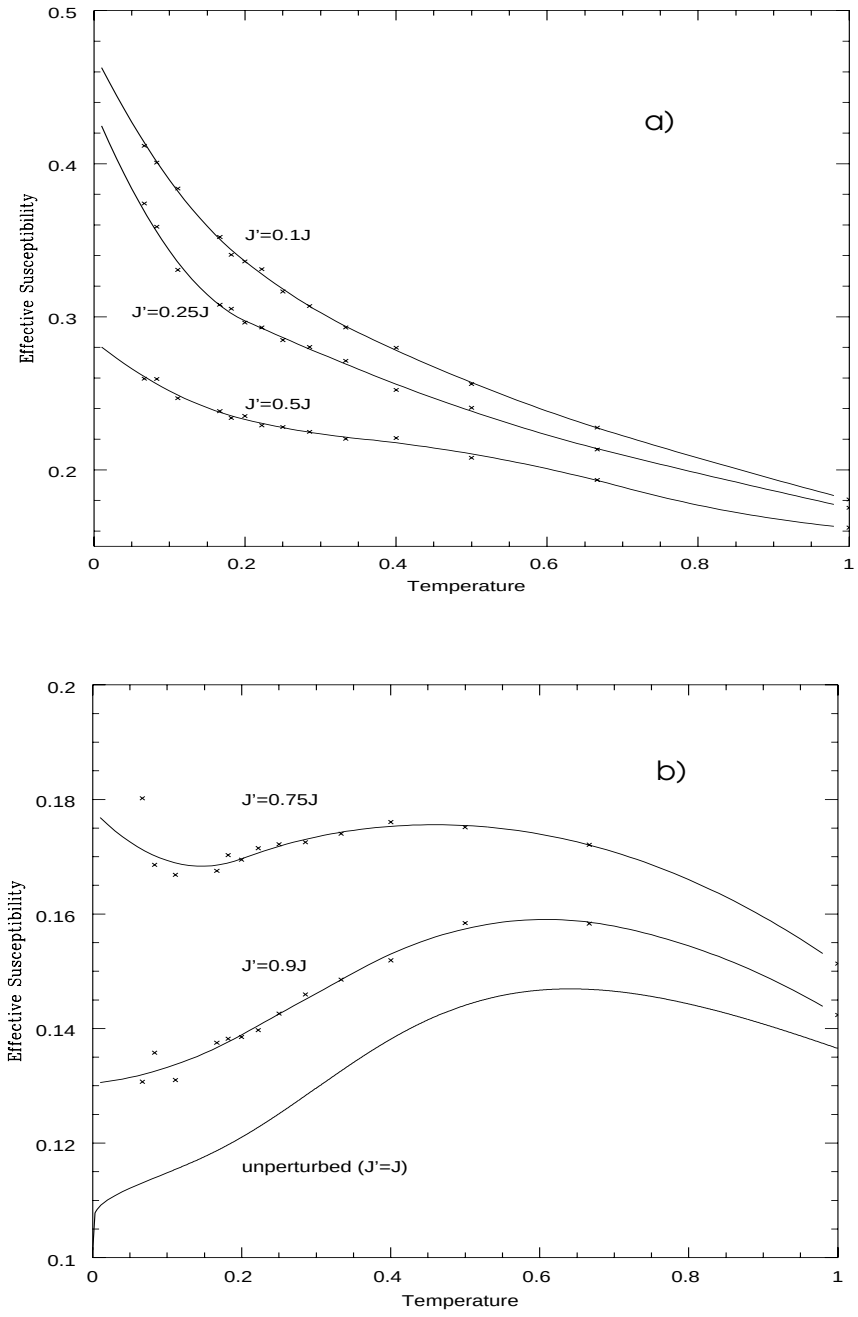

Figure 1.11: a) The local effective susceptibility as a function of temperature for strong perturbations of one link. b) The effective susceptibility as a function of temperature for weak perturbations of one link and J'=0.9 and J'=0.75. A value of J' closer to J corresponds to less perturbation (from Ref. [52]). Crosses are the QMC data.

Chapter 2

$\mu\mathcal{SR}$

In this chapter, we will introduce the $\mu\mathcal{SR}$ (μ^+ **S**pin **R**otation, **R**elaxation or **R**esonance) techniques used to obtain the data presented in this thesis[1]. Sections 2.1 and 2.2 describe properties of the muon and the fundamentals of muon decay. Section 2.3 deals with the various $\mu\mathcal{SR}$ signals observed under different experimental conditions, namely transverse field (TF), longitudinal field (LF) and zero field (ZF). In our experiments, time-differential LF technique was used to obtain the necessary information on localization and mobility of the muon in a graphite lattice. The Knight shift measurements were used to acquire information on the local electronic structure in the vicinity of a muon in graphite and LiC_6. The TF technique was also used to measure the muon frequency shift in CPC.

2.1 The Positive Muon as a Magnetic Probe

The muon is the most well studied unstable elementary particle. In this section we concentrate on the muon properties which are essential for its applications in condensed matter physics. The muon μ^- and its antiparticle μ^+ belong to the family of leptons and are well understood in the framework of the standard electroweak model [53]. The muon is a spin 1/2 particle and it possesses a magnetic moment $\mu_\mu = 3.18334539(10)\mu_p$ [54] and a gyromagnetic factor $\gamma_\mu/2\pi = 135.534$ MHz/T. Muons, like electrons, have no internal

[1] Although $\mu\mathcal{SR}$ generally includes both $\mu^+\mathcal{SR}$ (employing the positive muon , μ^+) and $\mu^-\mathcal{SR}$ (using the negative muon μ^-), throughout this thesis we refer only to the former.

Muon Properties	
Electric charge ($\mu^{\pm}$)	$\pm e$
Spin S_μ	$\mp\hbar/2$
Mass m_μ	105.659389(34) MeV/c^2
Muon/electron ratio m_μ/m_e	206.768262(30)
Gyromagnetic factor $\gamma_\mu/2\pi$	135.534 MHz/T
Magnetic moment μ_μ	$4.4904514(15) \times 10^{-26}$ J/T $4.84197097(71) \times 10^{-3}\mu_B$ $3.18334539(10)\mu_p$
$g-$factor g_μ	2.002331846(17)
Mean lifetime τ_μ	2.19703(4)μsec
Main decay modes in free space:	$\mu^- \rightarrow e^- + \overline{\nu}_e + \nu_\mu$ $\mu^+ \rightarrow e^+ + \nu_e + \overline{\nu}_\mu$

Table 2.1: Muon properties (from Ref. [55]).

structure and are considered to be true point-like particles. However, unlike electrons, the muon is not a stable particle and decays with a mean lifetime τ_μ of 2.19703(4) μsec [54] *via* the weak interaction. Properties of the muon are listed in Table 2.1. Despite the close similarity between the μ^+ and μ^- properties, their behaviour in matter is completely different. The negative muon μ^- is typically captured in high elliptical orbits and quickly (though not quickly enough to avoid partial depolarization through spin-orbit couplings) moves down to the $1S$ ground state *via* radiative transitions and Auger emission. Moreover, since the μ^- is about 207 times heavier than an electron, its ground state wave function has a significant overlap with nucleus, where it has high a probability of nuclear capture in the process $\mu^- + p \rightarrow n + \nu_\mu$. This in turn considerably reduces the bound μ^- lifetime compared to its free value, which is the same as that of the μ^+. Because of these difficulties, the negatively charged muon is not a popular tool in condensed matter physics, although it still plays a crucial role in nuclear and particle physics experiments.

Unlike its negative counterpart, the positive muon may be regarded as a light proton isotope with a mass of $\approx 1/9 m_p$. Upon implantation in condensed media, the μ^+ losses its energy primarily *via* ionization and scattering until it reaches an energy range on the order of a few KeV. This part of the thermalization process occurs within about 50 ps. The subsequent moderation occurs *via* a series of charge exchange reactions involving muonium atom $\mu^+ + e^- \leftrightarrow \mathrm{Mu}^o$. These captures and losses of the electron occur so rapidly in solids that within a time of about $5{\times}10^{-13}$ sec [56] the positive muon is either neutralized or stabilized as a positive ion. During this stage of the thermalization process the typical energy of the muon is ∼200 eV. Then inelastic collisions take place between Mu^{*o} or the epithermal μ^+ and the host atoms, leading to further rapid decrease in the muon energy down to $\leq$ 15 eV. The subsequent character of the muon state depends strictly on the nature of its electronic surrounding. For example, in insulators and semiconductors under certain conditions, epithermally-formed 'prompt' muonium remains stable; in other cases the stopped μ^+ captures one of its own ionization track electrons to form delayed muonium [57]. Muonium can also participate in chemical reactions leading to stable diamagnetic compounds or 'muoniated' radicals. In normal metals, because of the rapid charge exchange with free carriers, the muonium state is ill-defined. The μ^+ charge is screened by a cloud of itinerant electrons and its Coulomb interaction is considerably weakened. Because most of the energy loss occurs through both elastic and inelastic Coulomb scattering, the muon spin direction remains almost unaffected and thus the original muon polarization is preserved.

Another important issue is the radiation damage produced by the muon in a sample. During the thermalization process, the muon collides with atoms and produces interstitial Frenkel pairs. Therefore, there is a probability that the μ^+ might interact with these lattice defects, which in turn may complicate the interpretation of experimental data. The resolution of this concern comes from the fact that the process of vacancy creation has

a significant energy threshold and the vacancy pairs are produced only during the initial 'hot' stage of the thermalization process when the muon kinetic energy is high enough to produce such defects. Beyond that point, the muon will still penetrate deeper into the sample without creating any more vacancies. The simulations made for graphite assuming that the displacement threshold is set at $E_d = 50$ eV indicate that a distance between the last displacement and the thermalized μ^+ is on the order of 9000 Å. Therefore, in our interpretation of experimental data on graphite, one can neglect the muon-defect interaction.

2.2 Muon Production

In order to conduct $\mu\mathcal{SR}$ experiments, a high purity, highly polarized muon beam is required. In modern accelerators (*e.g* TRIUMF), the beam of polarized muons is generally produced by bombarding a target (*e.g.* carbon or beryllium) with high energy protons $E_p \geq 500$ MeV. The dominant nuclear reactions for μ^+ production and decay are:

$$p + p \rightarrow \pi^+ + p + n \tag{2.24}$$

$$p + n \rightarrow \pi^+ + n + n \tag{2.25}$$

$$\pi^+ \rightarrow \mu^+ + \nu_\mu \tag{2.26}$$

$$\mu^+ \rightarrow e^+ + \nu_e + \overline{\nu}_\mu \tag{2.27}$$

The π^+ mesons decay into positive muons and muon neutrinos. Consider this decay in the pion rest frame. Since the pions have no spin and neutrinos have helicity -1 then, by conservation of angular momentum, the muon spin S_μ must be aligned opposite to its momentum $\boldsymbol{p}_\mu$ (see Fig. 2.12 and Table 2.2) and the μ^+ acquires a 100% left–handed polarization in the rest frame of the pion (*i.e.* each muon's spin is aligned opposite to its momentum). If the pion is not at rest in the laboratory frame then

the beam polarization and its direction will depend on the tune of the beamline. So called 'backward' muons are produced by tuning the last part of the beamline for lower momentum than the front end where the pions are selected. This yields a μ^+ beam with right-handed polarization of $80-90\%$ and a typical momentum of $50-90$ MeV/c, useful for thick-walled pressure vessels and glass containers for liquids. Polarized negative muon beams are always produced from π^- decay in flight due to the immediate nuclear capture of negative pions stopped in the production target.

Properties	
$\pi^+ \rightarrow \mu^+ + \nu_\mu$	
Energy conservation	$E_\pi = m_\pi c^2 = E_\mu + E_\nu$
Momentum conservation	$\boldsymbol{p}_\pi = 0 \Longrightarrow \boldsymbol{p}_\mu = -\boldsymbol{p}_\nu$
Angular momentum conservation	$\boldsymbol{S}_\pi = 0 \Longrightarrow \boldsymbol{S}_\mu = -\boldsymbol{S}_\nu$

Table 2.2: Positive pion decay and associated conservation laws.

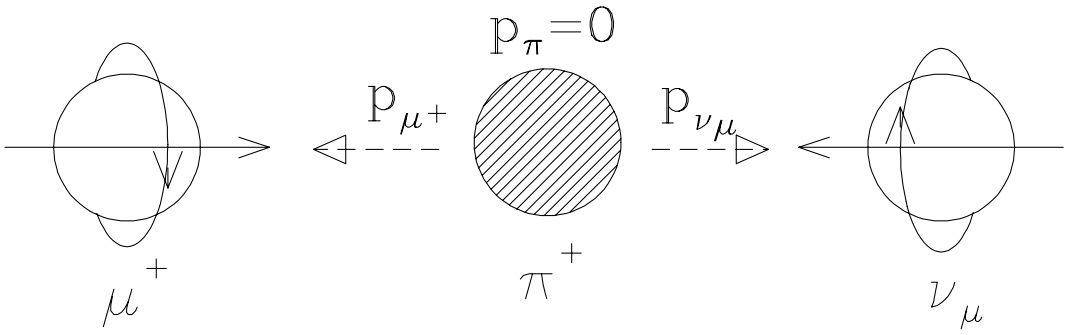

Figure 2.12: Pion decay as viewed in the rest frame.

These stopped positive pions decaying near the surface produce the high quality low-energy μ^+ beams also known as 'Arizona' or 'surface' muons [58]. Such a beam has several advantages. First, the surface muons have their spins pointing backwards with respect to their momentum, with a polarization close to 100% ($|\boldsymbol{P}_\mu| = 1$). Second, the muons

are low energy ($\langle|\boldsymbol{p}_\mu|\rangle$=29.8 MeV/c and have a stopping range $R_{\mu^+} = 140$ mg/cm^2 in water) that allow the performance of experiments on thin samples, thick superconducting films, organic materials and gases. One disadvantage is the beam contamination by positrons. To solve this problem, electrostatic velocity selectors utilizing crossed magnetic and electric fields are used [59].

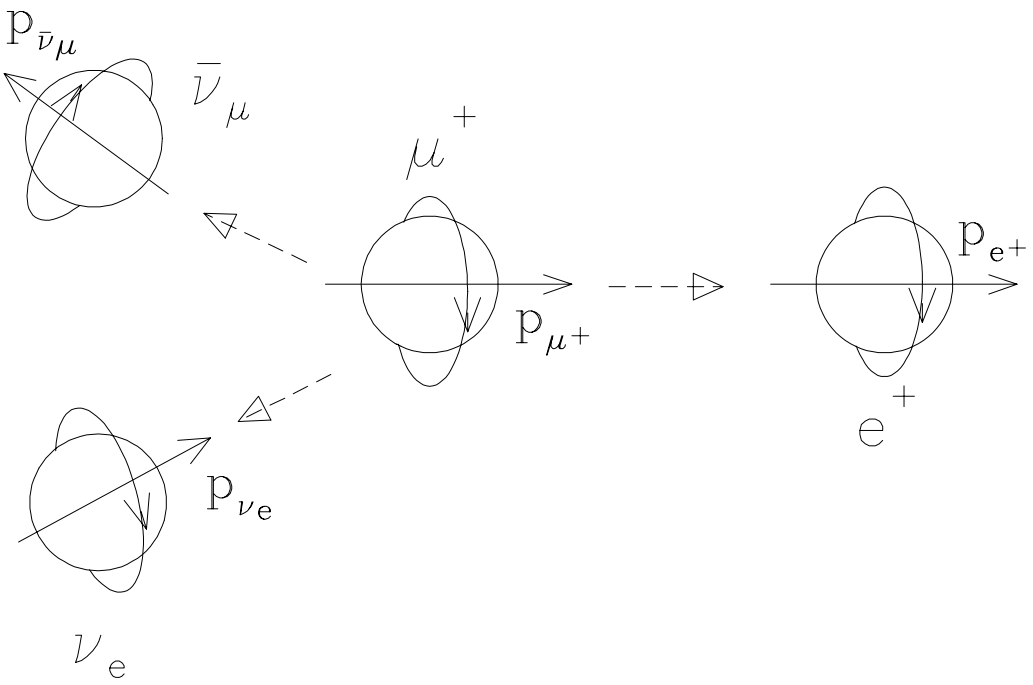

Figure 2.13: Muon decay.

A positive muon stopped in a sample decays according to the following reaction: $\mu^+ \rightarrow e^+ + \nu_e + \overline{\nu}_\mu$. Because of the 3-body nature of the decay, a positron leaving the sample can have a range of kinetic energies ranging between 0 and $E_{\max} = 1/2 m_\mu c^2[1 + (m_e/m_\mu)^2] - m_e c^2 = 52.320$ MeV. The maximum energy $E_{\max}$ is achieved when the neutrino ν_e and antineutrino $\overline{\nu}_\mu$ are emitted in the same direction (see Fig. 2.13). The only particle detected in $\mu\mathcal{SR}$ experiments (other than the muon itself) is the decay positron. The positron is preferentially emitted in the direction of the muon spin; this

allows the reconstruction of the muon polarization in the sample. This is a remarkable consequence of parity violation in weak decays. It follows from the electroweak theory that the probability of positron emission with an energy range $\epsilon, \epsilon + d\epsilon$ and solid angle $\Omega, \Omega + d\Omega$, at time $t, t + dt$ obeys

$$dW(\theta, \epsilon, t) = W(t)\Theta(\theta)\mathcal{E}(\epsilon)d\epsilon\frac{d\Omega}{4\pi}\frac{dt}{\tau_\mu} \tag{2.28}$$

$$W(t) = \exp(-t/\tau_\mu) \tag{2.29}$$

$$\Theta(\theta) = 1 + A(\epsilon)\cos(\theta) \tag{2.30}$$

$$\mathcal{E}(\epsilon) = 2\epsilon^2(3 - 2\epsilon) \tag{2.31}$$

$$A(\epsilon) = (2\epsilon - 1)/(3 - 2\epsilon) \tag{2.32}$$

where τ_μ is the muon mean lifetime, $\epsilon = E/E_{\max}$ is the reduced positron energy, the angle of positron emission θ is measured relative to the muon spin orientation (which defines $\theta = 0^o$) and $A(\epsilon)$ is the energy dependent asymmetry in the $\Theta(\theta)$ distribution (see Fig. 2.14).

A simple analysis shows that the asymmetry reaches its maximum value when positrons are emitted with $E_{\max} = 52.320$ MeV. The same asymmetry factor averaged over all possible values of ϵ ($\langle E \rangle = 35$ MeV) is equal to $\langle A \rangle = 1/3$ (see Fig. 2.15). The low energy positrons with kinetic energies ϵ <0.5 are preferentially emitted in the direction opposite to the muon spin, reducing the asymmetry factor; thus the average asymmetry factor A_o can be effectively increased by removing these low energy positrons using a degrader.

2.3 $\boldsymbol{\mu\mathcal{SR}}$ Signals: LF, ZF and TF Measurements

The muon polarization $\boldsymbol{P}_\mu(t)$ evolves in time according to the distribution of internal magnetic fields. The purpose of a typical TF $\mu\mathcal{SR}$ experiment is to reveal this information *via* the measurement of the asymmetry of decay positron as a function of time.

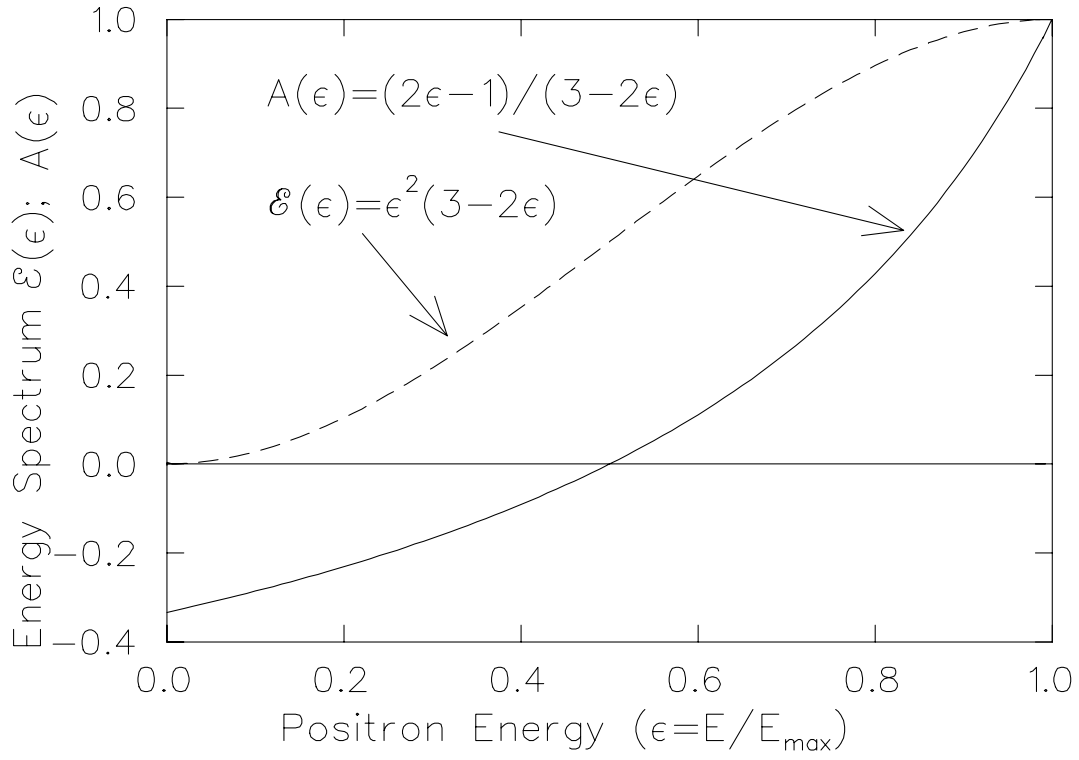

Figure 2.14: Muon energy spectrum.

A simplified sketch of a typical setup used in $\mu\mathcal{SR}$ experiments is shown in Fig. 2.16a. The incoming muons are detected in a thin scintillator (M) which triggers 'start' ($t = 0$) signal on a TDC ('clock') and opens a data gate (typically <10 μsec). Upon implantation the muon spin is aligned opposite to its momentum and the positron emission follows the $\Theta(\theta)$ distribution. This pattern evolves in time according to the distribution of internal magnetic fields. A positron produced in the muon's decay is registered by another scintillator (E) designed for this purpose. The signal from the positron counter is used to stop the clock. Each muon lifetime is then individually recorded in a time histogram on the on-line computer. The length of the data gate sets a limit on the rate of incoming muons which is typically on the order of 10^5 events/sec or less.

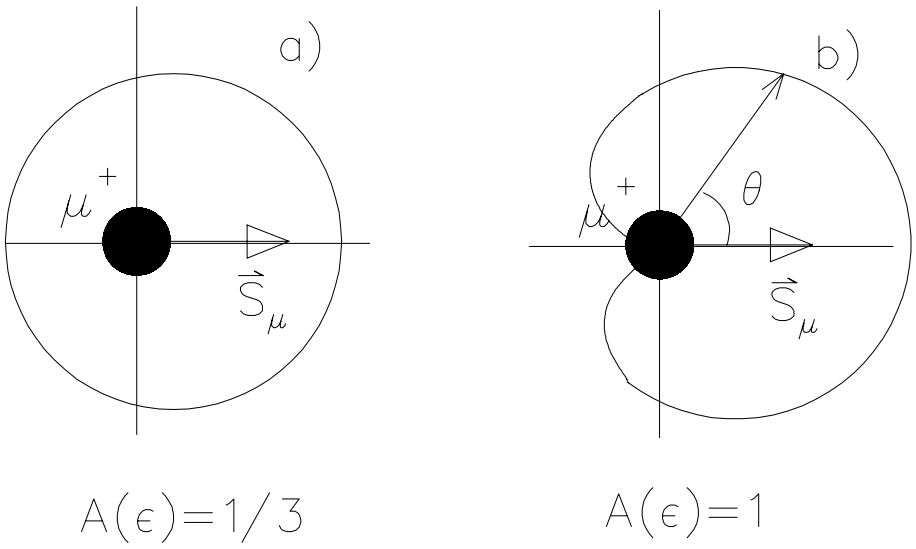

Figure 2.15: $\Theta(\theta)$ distribution of positrons: a) integrated over all energies and b) with maximum energy $E_{\max}$ of 52.320 MeV.

In the absence of any external or internal magnetic fields, the i^{th} positron counter whose effective angle makes an average angle ϕ_i with respect to the muon polarization will register the following distribution of decay times

$$N_i(t) = N_i^o\{\exp(t/\tau_\mu)[1 + A_i^o \cos(\phi_i)] + \mathcal{B}_i\} \tag{2.33}$$

where N_i^o is a normalization constant, A_i^o is the average positron asymmetry and $\mathcal{B}_i$ is the time-independent background fraction of uncorrelated 'noise' events. In an applied magnetic field $\boldsymbol{H}$, the muon spin starts precessing with the Larmor frequency $\omega_\mu = \gamma_\mu|\boldsymbol{H}|$. If $\boldsymbol{H}$ is perpendicular to the initial muon polarization $\boldsymbol{P}(0)$ then the $\Theta(\theta)$ distribution rotates as a whole with the same angular frequency ω_μ which is reflected in $N_i(t)$ as

$$N_i = N_i^o\{\exp(-t/\tau_\mu)[1 + A_i^o \cos(\omega_\mu t + \phi_i)] + \mathcal{B}_i\} \tag{2.34}$$

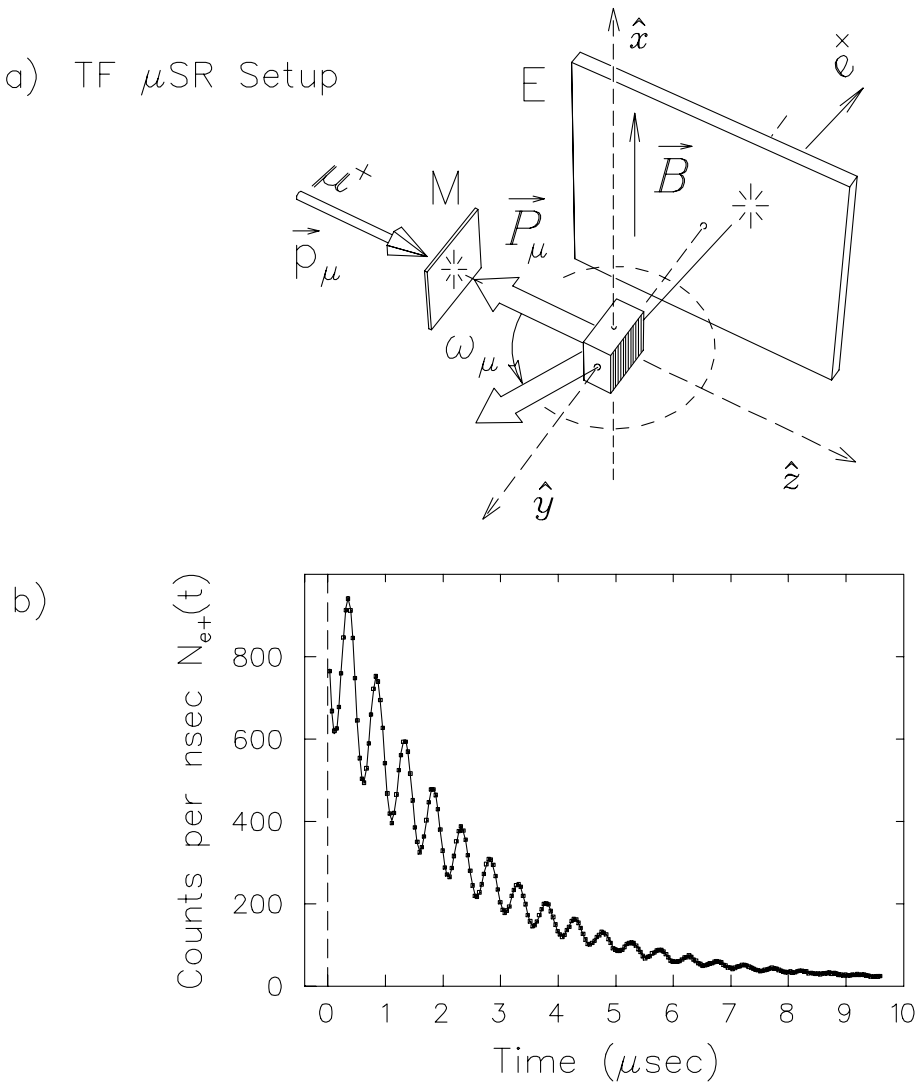

Figure 2.16: a) A conventional TF $\mu\mathcal{SR}$ setup. The magnet is omitted for clarity. b) A histogram of time differences between muon implantation and decay as detected by the single positron counter (courtesy of J. Brewer).

In a real $\mu\mathcal{SR}$ experiment, the implanted muon 'feels' the magnetic environment $\boldsymbol{B}_{\text{int}}$ of a sample which includes, but not limited to, the externally applied magnetic field $\boldsymbol{H}$. The internal field is often random in direction, magnitude or time, and usually fluctuates and depolarizes the muon spin. In order to account for this effect we need

to modify Eq. (2.34) by replacing the $\cos(\omega_\mu + \phi)$ term with a spectrum of frequencies, *i.e.* $G_{xx}(t)\cos(\langle\omega_\mu\rangle t + \phi_i)$. The envelope of these oscillations is called the transverse relaxation function $G_{xx}(t)$. If the average precession frequency is given by [60]

$$\langle\omega_\mu\rangle = \gamma_\mu \langle B_{int}^{\perp}\rangle \tag{2.35}$$

then the number of positron counts $N_i(t)$ is

$$N_i(\phi, t) = N_i^o\{\exp(-t/\tau_\mu)[1 + A_i^o G_{xx}(t)\cos(\langle\omega_\mu\rangle t + \phi_i)] + \mathcal{B}_i\} \tag{2.36}$$

Equation (2.36) is a foundation of $\mu\mathcal{SR}$ data analysis. By fitting the $N_i(t)$ histograms in the time domain one can obtain the two fundamental quantities of interest: the average frequency $\langle\omega_\mu\rangle$ and the relaxation function $G_{xx}(t)$. The latter gives us important clues about the nature of the internal magnetic fields; it can be of static or dynamic origin. For example, the simplest case of static depolarization corresponds to inhomogeneous broadening, where, instead of a single Larmor frequency ω_o one observes a spectrum of frequencies distributed around ω_o with a width σ.

The overall richness of magnetic phenomena studied by muons is vividly illustrated by the large number of theoretical depolarization functions available to experimenters. A particularly important case is the effect of randomly oriented static dipole moments on the $\mu\mathcal{SR}$ signal measured in an applied transverse field (TF) $\boldsymbol{H} = H\boldsymbol{z}$. The dipolar fields $\boldsymbol{B}_{\rm dip}$ from the surrounding magnetic moments are weak, typically not more than a few gauss. Assuming that the applied magnetic field $\boldsymbol{H}$ is much bigger than the average sum $B_{z_{\rm dip}}$ of the z components of the dipolar fields and that these components have a Gaussian distribution with [60]

$$\langle\overline{\Delta B}_{z_{\rm dip}}^2\rangle = \frac{1}{6}I(I+1)\mu_N^2 g_I^2\Big(\frac{\mu_o}{4\pi}\Big)^2 \sum_i \frac{[1 - 3\cos^2(\theta_i)]^2}{r_i^6}, \tag{2.37}$$

where r_i is the distance to nuclear spin I_i and θ_i is its angle with respect to the direction

of $\boldsymbol{H}$, the muon precession frequencies will be distributed with a mean square deviation

$$\sigma^2 = \frac{1}{2}\langle\overline{\Delta\omega_\mu}^2\rangle = \frac{1}{2}\gamma_\mu^2\langle\overline{\Delta B}^2_{z_{\rm dip}}\rangle \tag{2.38}$$

and the superposition of the precession signals will have the following time dependence

$$\langle\cos(\omega_\mu t)\rangle = \exp\left(-\sigma^2 t^2\right)\cos(\omega_o t). \tag{2.39}$$

As seen from Eq. (2.39), the $\mu\mathcal{SR}$ signal is still precessing at the mean Larmor frequency ω_o but is damped by the Gaussian factor (see Fig. 2.17)

$$G^G_{xx}(t) = \exp\left(-\sigma^2 t^2\right). \tag{2.40}$$

This effect of random static dipoles on the muon can also be described as a process

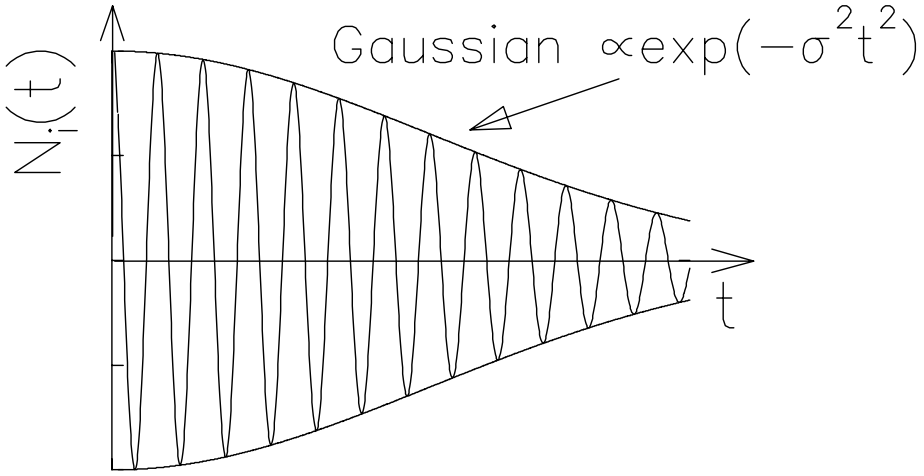

Figure 2.17: Typical Gaussian relaxation envelope function used to analyze TF data.

in which the muon spin is subjected to the different internal fields $B^i_{z_{\rm dip}}$ whose effect is to gradually decrease the phase coherence (dephasing) in the plane perpendicular to applied magnetic field $\boldsymbol{H}$. Since this dephasing can be reversed by a 'π pulse' of RF at the resonant frequency, resulting in a 'spin echo' [61], it is technically incorrect to refer to it as 'relaxation'; nevertheless, this terminology is virtually universal in $\mu\mathcal{SR}$.

2.3.1 Longitudinal and Zero Field Measurements

All the relaxation mechanisms presented so far have a direct analogy in NMR. However, with the introduction of μ^+ beams, a new class of condensed matter experiments has been successfully developed. In this section we introduce zero field (ZF) and longitudinal field (LF) techniques. In the case of longitudinal field (applied field $\boldsymbol{H}$ in the direction of the initial muon polarization) the natural quantization axis is also in the beam direction. For conventional LF measurements, the positron detectors are arranged in front of and behind the sample (as 'seen' by the muon beam) and are usually labeled as forward (F) and backward (B) (see Fig. 2.18). The number of registered positrons is described by Eq. (2.36) with $\phi_B = 0^o$, $\phi_F = 180^o$ and $\omega_\mu = 0$:

$$N_{B,F}(\phi, t) = N_o^{B,F}\{\exp(-t/\tau_\mu)[1 + A_o^{B,F} G_{zz}(t)\cos(\phi_{B,F})] + \mathcal{B}_{\mathcal{B},\mathcal{F}}\}. \tag{2.41}$$

In the zero field case, the muon spin will precess around *local* axes in the j^{th} site with angle δ_j and with frequency ω_j. The time evolution of the longitudinal components of the polarization vector $G_{zz}^{(j)}(t)$ in the j^{th} site is then given by

$$G_{zz}^{(j)}(t) = \cos^2(\delta_j) + \sin^2\delta_j \cos(\omega_j t). \tag{2.42}$$

Averaging over all possible directions of the local magnetic fields gives

$$\langle G_{zz}^{(j)}(t)\rangle = \frac{1}{3} + \frac{2}{3}\langle\cos(\omega_j t)\rangle \tag{2.43}$$

and averaging over a Gaussian frequency distribution gives the famous Kubo-Toyabe result [65]

$$G_{zz}^{GKT}(t) = \frac{1}{3} + \frac{2}{3}\Big(-1 - \Delta^2 t^2\Big)\exp\Big[-\frac{1}{2}\Delta^2 t^2\Big] \tag{2.44}$$

where $\Delta^2 = \gamma_\mu^2\langle B_{\text{loc},x}^2\rangle + \gamma_\mu^2\langle B_{\text{loc},y}^2\rangle = 2\gamma_\mu^2\langle B_{\text{loc},z}^2\rangle$. By inspecting Eq.(2.44) one can see that initially $G_{zz}^{GKT}(t)$ decays faster than $G_{xx}^{G}(t)$ (see Eq. 2.40) with the effective $\Delta =$

$\sqrt{2\gamma_\mu^2\langle B_{\mathrm{loc},z}^2\rangle} = \sqrt{2}\sigma$. This can be intuitively understood since in the strong transverse field only the z components contribute to the dephasing of the muon spin, whereas both the x and y components participate in the LF relaxation process. In other words, LF measurements provide the same information as TF measurements but with higher sensitivity [66].

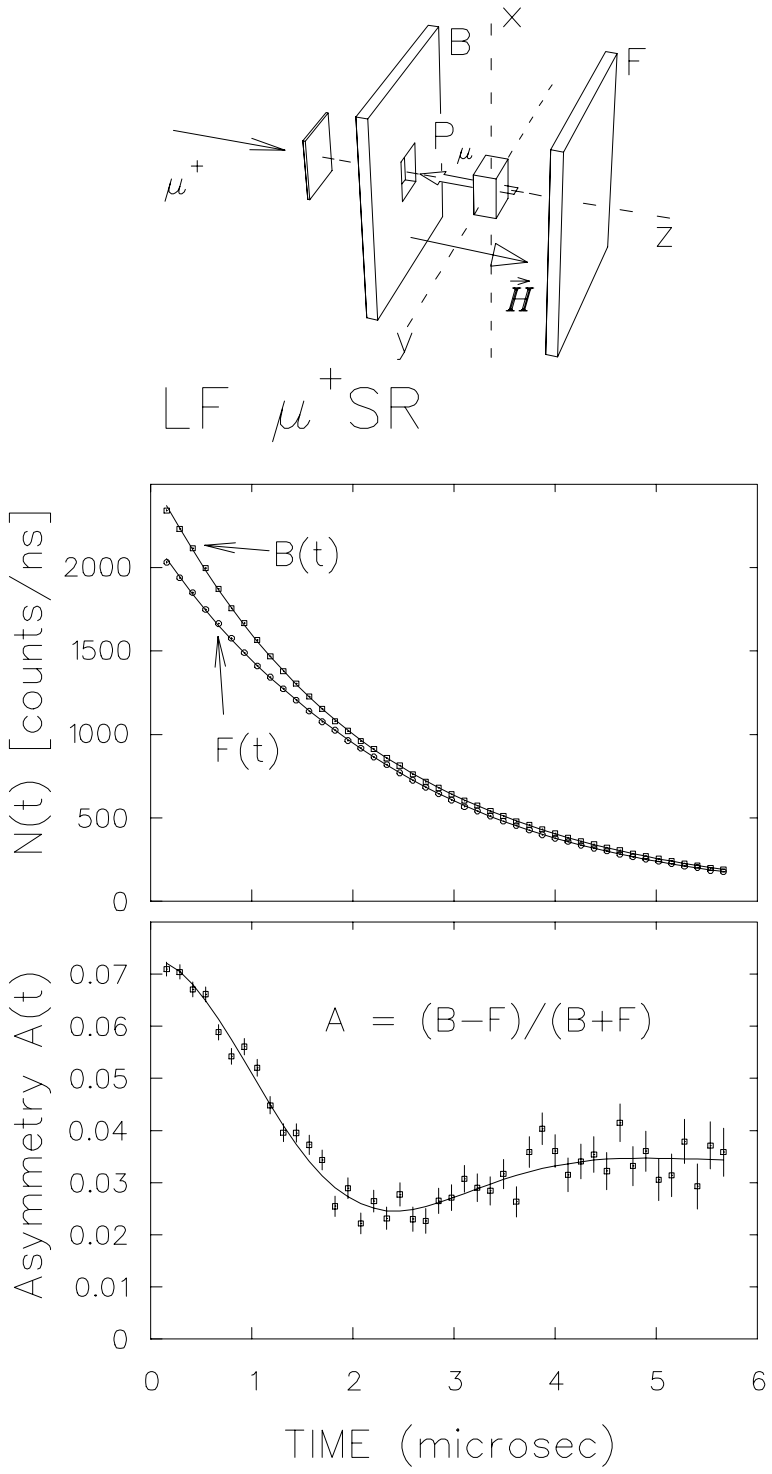

Figure 2.18: General LF $\mu\mathcal{SR}$ setup showing the sample and three counters. The magnetic field is applied parallel to $\boldsymbol{P}_\mu$ (courtesy of J. Brewer).

2.3.2 Relaxation due to itinerant electrons

Typically, in a normal metal the relaxation processes due to conduction electrons play an important role and can be dominant when there are no localized electronic moments. In the case of the muon, the relaxation process can be pictured as a muon spin flip by conduction electron spins. In the Born approximation, the relaxation rate $1/T_1$ is given by [62]

$$\frac{1}{T_1} = \frac{4\pi}{9}\hbar^3\mu_o^2\gamma_\mu^2\gamma_e^2 \mid \psi(0) \mid^4 g(E_F)^2 k_B T \tag{2.45}$$

where $\psi(0)$ is the s electron spin density on a muon and $g(E_F)$ is the density of states at the Fermi level. However, it can be shown [67] that the effect of the *direct* spin relaxation by free carriers is practically undetectable on the $\mu\mathcal{SR}$ timescale. On the other hand, the μ^+ spin still can be relaxed indirectly if the system contains paramagnetic spins strongly coupled with the muon spin. In Section 4 this type of relaxation will be discussed in more detail.

2.3.3 Muon Knight Shift

In the presence of an external magnetic field $\boldsymbol{H}$, the total field $\boldsymbol{B}_\mu(\boldsymbol{r}_\mu)$ at the muon site consists of the following macroscopic and microscopic or hyperfine contributions (in this section we follow discussion presented in [68] by Schenck and Gygax)

$$\boldsymbol{B}_\mu(\boldsymbol{r}_\mu) = \boldsymbol{H} + \boldsymbol{B}_{\text{macro}} + \boldsymbol{B}_{\text{micro}}(\boldsymbol{r}_\mu) \tag{2.46}$$

$$\boldsymbol{B}_{\text{macro}} \equiv \boldsymbol{B}_L(\boldsymbol{M}) + \boldsymbol{B}_{\text{demag}}(\mathcal{N}, \boldsymbol{M}) \tag{2.47}$$

The terms in $\boldsymbol{B}_{\text{macro}}$ are proportional to the bulk magnetization $\boldsymbol{M}$ and represent the macroscopic part of the total field and will be discussed in Sec. 2.3.4. The microscopic part is composed of dipolar fields and the contact hyperfine field

$$\boldsymbol{B}_{\text{micro}}(\boldsymbol{r}_\mu) = \boldsymbol{B}_{\text{dip}}(\boldsymbol{r}_\mu) + \boldsymbol{B}_c(\boldsymbol{r}_\mu) \tag{2.48}$$

$$\boldsymbol{B}_{\rm dip}(\boldsymbol{r}_\mu) = \frac{\mu_o}{4\pi}\sum_{\boldsymbol{r}_i}\frac{3\boldsymbol{r}_i(\boldsymbol{\mu}_i\cdot\boldsymbol{r}_i)-\boldsymbol{\mu}_i(\boldsymbol{r}_i\cdot\boldsymbol{r}_i)}{\boldsymbol{r}_i^5} \tag{2.49}$$

$$\boldsymbol{B}_c(\boldsymbol{r}_\mu) = \frac{8\pi}{3}\langle|\psi_e(\boldsymbol{r}_\mu)|^2\rangle_F\chi\boldsymbol{H} \tag{2.50}$$

where $\boldsymbol{\mu}_i$ is a dipole moment at a distance $\boldsymbol{r}_i$ from the muon, $\langle|\psi_e(\boldsymbol{r}_\mu)|\rangle_F$ is the spin density of conduction electrons at the μ^+ averaged over the Fermi surface and χ is the local electronic spin susceptibility. Clearly the contact term is only present when there is a finite s electron spin density at the muon site.

Let us consider the effect of the induced hyperfine field on the muon spin. In the free electron approximation, the contact hyperfine field on the μ^+ induced by the polarized conduction electrons is [69]

$$\boldsymbol{B}_c(\boldsymbol{r}_\mu) = \frac{8\pi}{3}\mu_B\Big[n^+(\boldsymbol{r}_\mu)-n^-(\boldsymbol{r}_\mu)\Big] \tag{2.51}$$

where $n^+(\boldsymbol{r}_\mu)$ and $n^-(\boldsymbol{r}_\mu)$ are the corresponding perturbed electron spin-up and spin-down densities at the muon site $\boldsymbol{r}_\mu$ and their difference is the net induced spin density on the muon. As a result there will be a small addition to the Larmor frequency $\omega_\mu = \omega_o+\omega_c$ and ω_c will be proportional to the applied magnetic field . This frequency shift can be conveniently expressed as the dimesioneless ratio

$$\mathcal{K}_c = \frac{\omega_c-\omega_o}{\omega_o} = \frac{B_c(\boldsymbol{r}_\mu)-H}{H} \tag{2.52}$$

known as the Knight shift. Within the free electron gas approximation, one can also derive a relationship between electron spin susceptibility χ_s and the Knight shift [60]

$$\mathcal{K}_c = \frac{8\pi}{3}\mu_B\frac{[n^+(\boldsymbol{r}_\mu)-n^-(\boldsymbol{r}_\mu)]}{n_o^+-n_o^-}\Big(\frac{n_o^+-n_o^-}{H}\Big) \tag{2.53}$$

$$\text{where}\qquad n_o^+-n_o^- = \chi_s H/\mu_B \tag{2.54}$$

where we have introduced the average unperturbed conduction electron spin density n_o. Finally, the Knight shift can be expressed in terms of the spin density enhancement factor

$\rho_s(\boldsymbol{r}_\mu)$

$$\mathcal{K}_c = \frac{8\pi}{3}\frac{[n^+(\boldsymbol{r}_\mu) - n^-(\boldsymbol{r}_\mu)]}{n_o^+ - n_o^-}\chi_s \equiv \frac{8\pi}{3}\rho(\boldsymbol{r}_\mu)\chi_s. \tag{2.55}$$

Equation (2.55) means that if the only effect of the applied external field is the re-population of spin-up and spin-down conduction electrons and if $\rho(\mathbf{r}_\mu)$ is temperature independent then the Knight shift will follow the Pauli paramagnetic susceptibility. This result is confirmed by the majority of measurements on simple metals [70],[71],[72],[73], where with a few exceptions (*i.e.* Bi, Sr, Ga and Sb), the measured Knight shift is found to be small (< 100 ppm), positive and almost independent of temperature and magnetic field. On the other hand, any deviations from Eq. (2.55) would indicate that the local spin susceptibility is different than that of the bulk.

To gain an insight into some other possibilities [67], we will rearrange the spin density:

$$\begin{aligned} n^+(\boldsymbol{r}_\mu) - n^-(\boldsymbol{r}_\mu) &\equiv n^+ \mid \psi^+(\boldsymbol{r}_\mu) \mid^2 - n^- \mid \psi^-(\boldsymbol{r}_\mu) \mid^2 \\ &= 1/2(n^+ - n^-)\left\{\mid \psi^+(\boldsymbol{r}_\mu) \mid^2 + \mid \psi^-(\boldsymbol{r}_\mu) \mid^2\right\} \\ &+1/2(n^+ + n^-)\left\{\mid \psi^+(\boldsymbol{r}_\mu) \mid^2 - \mid \psi^-(\boldsymbol{r}_\mu) \mid^2\right\}. \end{aligned} \tag{2.56}$$

The first term in Eq. (2.56) only needs to be evaluated at the Fermi surface; by neglecting any difference between the wave functions of spin-up and spin-down electrons and assuming that $(n^+ - n^-) \propto H$ [*via* the spin susceptibility, see Eq. (2.54)] we arrive at the same result as in Eq. (2.55), which represents a direct or 'contact' interaction on the muon. However, the *exchange* interaction between spin polarized electrons on the Fermi surface and the electrons occupying levels below the Fermi level can lead to wavefunction distortions and result in a spin polarization at the μ^+ opposite in sign to that of the electrons at the Fermi surface [60]. This effect is known as *core polarization* and is often used to explain a *negative* sign of the measured Knight shift; the core polarization is then considered to be a dominant factor. The second exchange term in Eq. (2.56) describes this core polarization effect.

A few notes on the specifics of Knight shift measurements with muons are in order. In a conventional TF $\mu\mathcal{SR}$ experiment the muon frequency shift is determined by measuring the μ^+ Larmor frequency ω_μ with respect to a well defined reference signal ω_r. The μ^+ Larmor frequency is given by $\omega_\mu = \gamma_\mu |\boldsymbol{B}_\mu(\boldsymbol{r}_\mu)|$ where $\gamma_\mu/2\pi = 135.5387$ MHz/T. If we neglect the 'macro' contributions to the total field $\boldsymbol{B}_\mu(\boldsymbol{r}_\mu)$ at the muon site, the μ^+ frequency ω_μ can be expressed in terms of the known internal fields as

$$\begin{aligned} \omega_\mu &= \gamma_\mu \sqrt{|\boldsymbol{H} + \boldsymbol{B}_{\rm dip}(\boldsymbol{r}_\mu) + \boldsymbol{B}_c(\boldsymbol{r}_\mu)|^2} \\ &= \gamma_\mu H \sqrt{1 + \frac{2}{H^2}(\boldsymbol{B}_{\rm dip} + \boldsymbol{B}_c)\cdot\boldsymbol{H} + \frac{1}{H^2}(\boldsymbol{B}_{\rm dip} + \boldsymbol{B}_c)^2} \end{aligned} \tag{2.57}$$

If we assume that $|\boldsymbol{H}| \gg |\boldsymbol{B}_{\rm dip}|$ and $|\boldsymbol{H}| \gg |\boldsymbol{B}_c|$, the expression for ω_μ can be simplified:

$$\begin{aligned} \omega_\mu &\approx \gamma_\mu H \sqrt{1 + \frac{2}{H^2}(\boldsymbol{B}_{\rm dip} + \boldsymbol{B}_c)\cdot\boldsymbol{H})} \\ &\approx \gamma_\mu \Big(H + \frac{1}{H}(\boldsymbol{B}_{\rm dip} + \boldsymbol{B}_c)\cdot\boldsymbol{H} \Big). \end{aligned} \tag{2.58}$$

The extra field $(\boldsymbol{B}_{\rm dip} + \boldsymbol{B}_c)\cdot\boldsymbol{H}/H$ induced at the muon site causes the muon frequency shift. One can define a muon Knight shift constant $\mathcal{K}_\mu = \boldsymbol{B}_c \cdot \boldsymbol{H}/H^2$ which depends only on the contact interaction[2] [60]. For the purpose of practical calculations, in the common case of axially symmetric systems, the muon Knight shift is given by the following standard expressions [60]

$$\mathcal{K}_\mu = \frac{1}{3}\mathcal{K}_{\rm iso}\Big[(\chi_\parallel + 2\chi_\perp) + 2(\chi_\parallel - \chi_\perp)P_2(\cos\theta)\Big] + \frac{1}{3}\mathcal{K}_{\rm dip}\Big[(\chi_\parallel - \chi_\perp) + 2(\chi_\perp + 2\chi_\parallel)P_2(\cos\theta)\Big] \tag{2.59}$$

where

$$\mathcal{K}_{\rm iso} = \frac{1}{3}(\mathcal{K}_\parallel + 2\mathcal{K}_\perp) \tag{2.60}$$

$$\text{and} \qquad \mathcal{K}_{\rm dip} = \frac{1}{3}(\mathcal{K}_\parallel - \mathcal{K}_\perp) \tag{2.61}$$

[2] Alternatively, one could also include a dipolar term as a part of the Knight shift [68].

are the contact and dipolar parts of the Knight shift, measured *via* $\mathcal{K}_\perp$ and $\mathcal{K}_\parallel$ by applying an external magnetic field $\boldsymbol{H}$ parallel and perpendicular to the crystal axis, and θ is the angle between the applied magnetic field and the axis of crystal symmetry.

A few general comments on the Knight shift are in order. First, it is important to realize that the measured Knight shift $\mathcal{K}_\mu$ carries a wealth of information on the local electronic structure in the vicinity of a muon; the main difficulty is to separate the various contributions to the shift. For instance, at muon sites in materials with cubic symmetry, or in powders, the sum of dipolar fields averages to zero. Therefore in powdered samples the Knight shift is not influenced by the dipolar interactions and the only contribution comes directly from the contact interactions. On the other hand, there will be a distribution of dipolar fields which broadens the $\mu\mathcal{SR}$ line (so called powder broadening [61]). Second, in the presence of a local moment $\mathcal{K}_{\rm iso}$ carries the information on the exchange interaction between itinerant electrons and the local magnetic moment. Unfortunately, the detailed interpretation of $\mathcal{K}_{\rm iso}$ is complicated by the specifics of the electronic structure in the vicinity of the muon. On the other hand, the dipolar part $\mathcal{K}_{\rm dip}$ is less susceptible to the disturbances introduced by the muon and is a measure of the atomic susceptibility (or local moment) of the *nearest* neighbors to the implanted μ^+.

2.3.4 Macroscopic (Bulk) Contributions

In addition to the microscopic fields seen by an implanted μ^+ there will be another important contribution specifically attributed to the *macroscopic* demagnetization fields induced by an external magnetic field. This macroscopic contribution to the local magnetic field found in homogeneously magnetized medium is proportional to the *bulk* magnetization and can be conveniently subdivided into two parts: the demagnetization field $\boldsymbol{B}_{\rm demag}$

and the Lorentz field $\boldsymbol{B}_L$

$$\boldsymbol{B}_{\text{demag}} = \mu_o \mathcal{N} \boldsymbol{M}_M \tag{2.62}$$

$$\boldsymbol{B}_L = \frac{1}{3}\mu_o \boldsymbol{M}_D \tag{2.63}$$

where $\mathcal{N}\boldsymbol{M}_M$ is bulk magnetization and and $\boldsymbol{M}_D$ is the magnetization inside the Lorentz sphere. The Lorentz sphere is a fictitious construction that provides an interface between the continuum magnetization picture and its microscopic components. The Lorentz construction and the magnetic fields associated with it are schematically illustrated in Fig. 2.19. Note that the magnetic field outside of the Lorentz volume Ω_L depends on the bulk macroscopic magnetization $\boldsymbol{M}_M$ and therefore is *shape* dependent. The shape dependence is introduced *via* the demagnetization factor $\mathcal{N}$ which is generally a tensor quantity. In practice its value can be calculated analytically only for a very limited number of shapes (*e.g.* ellipsoids, certain types of cylinders and planes) and generally must be evaluated numerically [74],[75]. The volume V outside of the Lorentz sphere is treated as a continuum, whereas the residual magnetic field

$$\boldsymbol{B'}_{\text{dip}}(\boldsymbol{r}_\mu) = \frac{\mu_o}{4\pi} \sum_{\Omega_L} \frac{3\boldsymbol{r}_j(\boldsymbol{\mu}_j \cdot \boldsymbol{r}_j) - \boldsymbol{\mu}_j(\boldsymbol{r}_j \cdot \boldsymbol{r}_j)}{r_j^5} \tag{2.64}$$

within the volume Ω_L is a subject of microscopic calculations and typically requires numerical summation over the large number of dipolar moments. Notice that for a spherical volume Ω_L the residual dipolar field $\boldsymbol{B'}_{\text{dip}}$ must be independent of Ω_L, given a sufficiently large volume. In practice, under certain conditions listed in Table 2.3.4, the overall macroscopic contribution is significantly simplified.

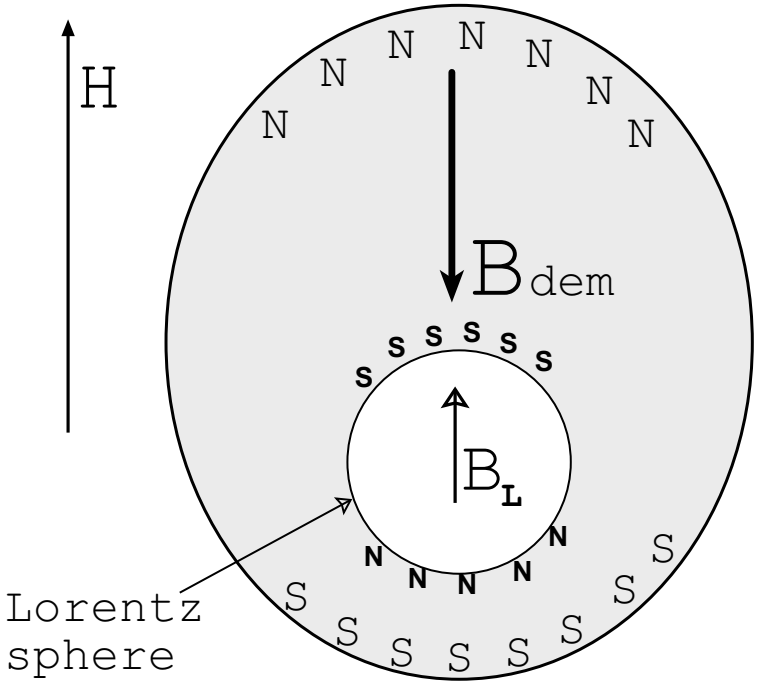

Figure 2.19: Macroscopic fields in the Lorentz sphere.

$\boldsymbol{B'}_{\rm dip} = 0$	a lattice site with cubic symmetry (*e.g.* octahedral or tetrahedral interstitial sites)
$\langle \boldsymbol{B'}_{\rm dip} \rangle = 0$	for an isotropic distribution of dipolar moments (for example, polycrystals in the paramagnetic state)
$\boldsymbol{B}_L + \boldsymbol{B}_{\rm demag} = 0$	for spherically shaped samples ($\mathcal{N}$=1/3) and completely saturated magnetization ($\boldsymbol{M}_M = \boldsymbol{M}_D \equiv \boldsymbol{M}_{\rm sat}$) or for paramagnets with $\boldsymbol{M}_M = \boldsymbol{M}_D \propto \chi_s \boldsymbol{H}$
$\boldsymbol{H} = \boldsymbol{B}_{\rm demag} = 0$	in the absence of any external magnetic field ($\boldsymbol{H} = 0$) in non-magnetic samples ($\boldsymbol{M}_M = 0$)
$\boldsymbol{M}_D = \boldsymbol{M}_S$	in ferromagnets with spontaneous magnetization $\boldsymbol{M}_S$
$\boldsymbol{M}_M = \boldsymbol{M}_D = \boldsymbol{M}_{\rm sat}$	for perfectly saturated magnets at $T = 0$
$\boldsymbol{M}_M = \boldsymbol{M}_D \propto \chi_s \boldsymbol{H}$	for paramagnetic samples in an applied magnetic field $\boldsymbol{H}$ with paramagnetic susceptibility χ_s

Table 2.3: Macroscopic contributions to the local field in some special cases.

Chapter 3

Apparatus and Electronics

3.1 Knight Shift Apparatus

All the Knight shift measurements reported in this thesis have been performed on the M20 and M15 beamlines at TRIUMF, which provide a beam of nearly 100% spin polarized positive surface muons with a momentum of 29.8 MeV/c. The muon spin polarization was rotated perpendicular to the axis of the superconducting solenoid and the muon beam direction. The graphite samples were cut from high purity, highly oriented pyrolytic graphite (HOPG) with $\boldsymbol{c}$ axis aligned to better than 2 degrees. A single piece or five pieces were used depending on whether the field was applied in parallel or perpendicular to the average $\boldsymbol{c}$ direction respectively. Although the frequency shift scales with magnetic field the amplitude of the $\mu\mathcal{SR}$ signal decreases at higher fields when the period of the Larmor precession frequency becomes comparable to the timing resolution of the detectors. Thus, the magnitude of the applied magnetic field was chosen to be 1.45 T.

In order to make precise Knight shift measurements a novel $\mu\mathcal{SR}$ technique was used to collect the data on a sample and a reference simultaneously [76]. Figure 3.20 shows a schematic of the apparatus used for frequency measurements at low temperatures. The helium flow cryostat has been omitted for the purpose of clarity. The collimated muon beam passes through a thin plastic scintillator (M) before entering the cryostat. The crucial element of the setup is the second thin muon counter (M_s) in the sample space of the cryostat. Light from the edges of the M_s counter is reflected down the axis of a

hollow light guide (covered with silverized mylar) and out the back end of the cryostat to a photomultiplier (not shown). The M_s scintillator is tightly sandwiched between the sample on the downstream and the reference just upstream. The reference is an annular disk of high purity silver foil (99.99%) with a 1 cm diameter hole at the centre. About half of the incoming muons stop in the reference without triggering M_s while half pass through the hole, trigger the M_s counter and then stop in the sample. This allows us to cleanly distinguish muons stopping in the sample from those stopping in the reference.

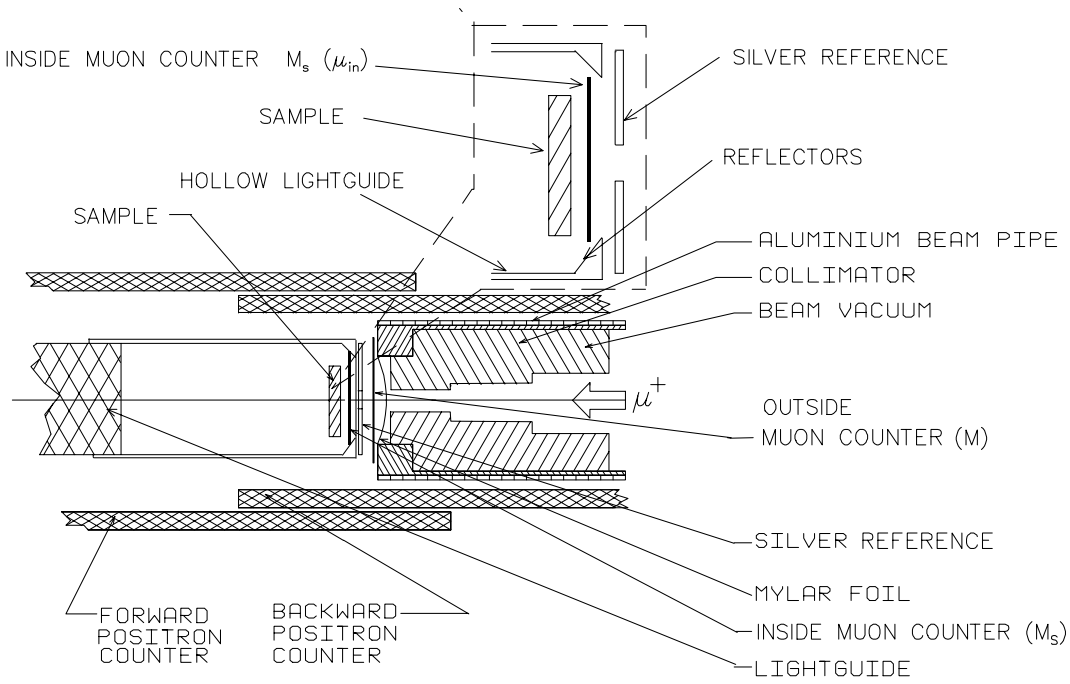

Figure 3.20: Schematic of the apparatus for precise measuring two $\mu\mathcal{SR}$ spectra simultaneously.

Such a detector arrangement has several advantages. Most importantly, it allows us to collect $\mu\mathcal{SR}$ spectra on the reference and the sample simultaneously, thus eliminating many of the systematic effects (*e.g.* drift in an external magnetic field, thermal contraction, instabilities in electronics, changes in the beam properties, *etc.*). Second, the

sample spectra are exceptionally clean and have no detectable signal from the reference or elsewhere. This eliminates other errors due to the variations in background to foreground ratio which can influence the frequency measurement. Note, in general, the background and foreground signals are very close in frequency and are thus not easily distinguished. The statistical accuracy on individual frequencies is about 2 ppm after about an hour of data collection ($\sim 10^7$ events) and the systematic error on the frequency shift is estimated to be at about the same level.

A similar geometry was used for measurements above room temperature. However, in this case the second muon counter and a silver mask were placed just outside the oven and 20 mm in front of the sample. This was necessary since it is not possible to use a plastic scintillator at high temperatures.

In order to test for 'cross talk' between the two channels (sample-reference) we ran a control experiment with Al_2O_3 at the sample position. Since Al_2O_3 at RT produces no muon precession signal at the Larmor frequency, any observed signal can be attributed to false routing or range strangling in the thin M_s detector. Figure 3.21 shows the Fourier transforms for the sample and the reference respectively. A very small precession signal in the top picture demonstrates that there is at most a 3% background signal in the sample histograms. In order to keep the background small at low temperatures, where the He gas density can be rather large, it is important to pump hard on the sample space in order to minimize range straggling. Muons which stop in the M_s counter give rise to a background signal in the sample histograms from the plastic scintillator. 'Cross talk' in the other direction is also quite small as evidenced by the fact that the asymmetry in the reference spectrum ($A_\mu = 0.211$) is consistent with the maximum experimental value (obtained with Ag at the sample position) indicating that there is a little Al_2O_3 signal ($< 5\%$) in the reference histograms. False routing in this direction is mostly attributed to inefficiency in the M_s counter.

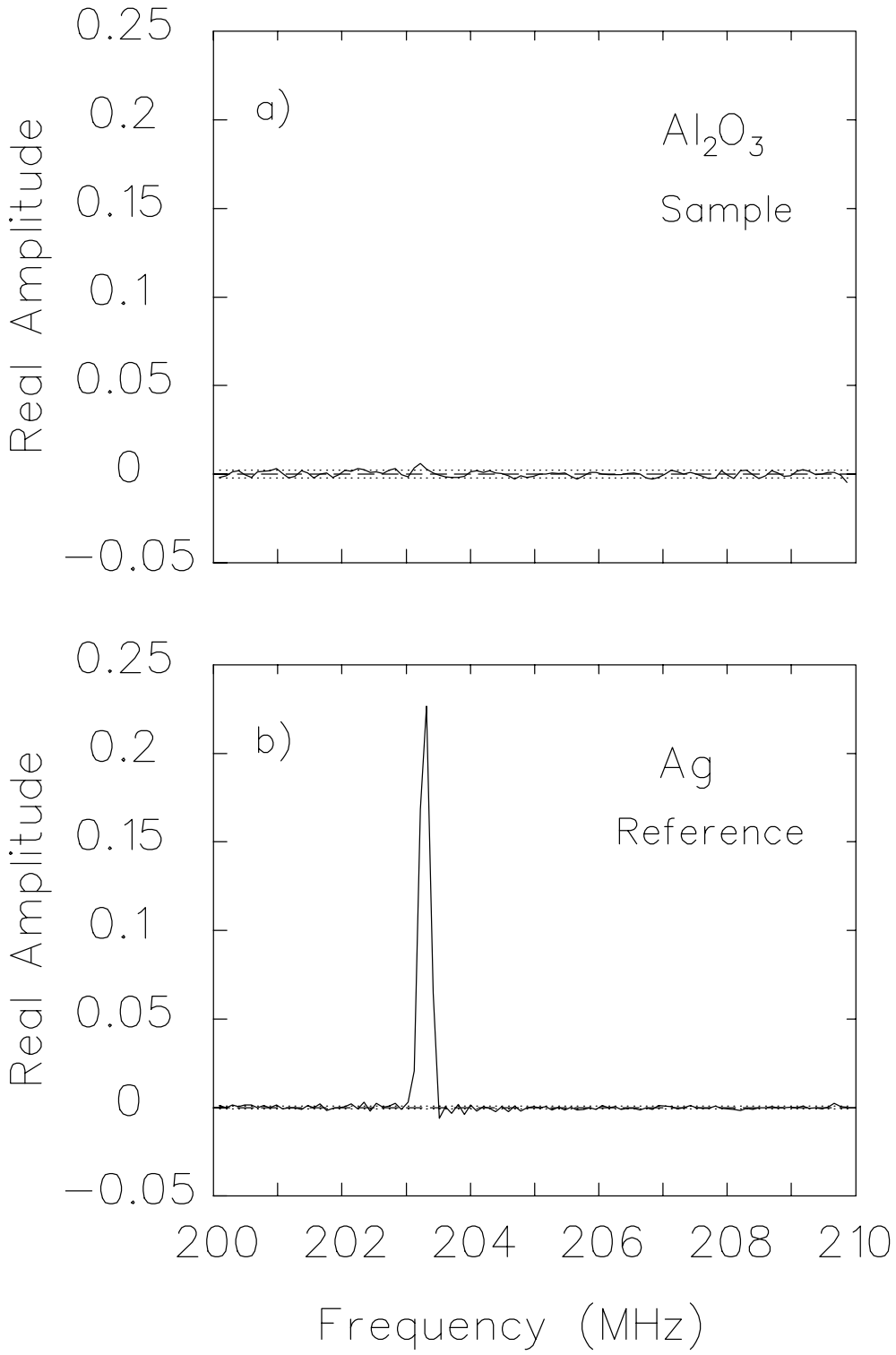

Figure 3.21: Real amplitude of muon precession signal in a transverse magnetic field of 1.45 T. In a) Al_2O_3 at the sample position and b) Ag foil at the reference position [76].

3.2 Electronics

The time-differential (TD) electronics corresponding to the setup described above is shown in Fig. 3.22. Before we describe the sequence of events that takes place in electronics let us consider a few general points relevant to our detection system. When a charged particle such as a muon or a positron passes through a plastic scintillator it deposits energy which is converted to photons. For example, a typical 'surface' muon with a kinetic energy of 4 MeV passing through a 2.5 mm thick scintillator generates about 4600 photons. The thickness of the muon counter (1.4 mm) is chosen to ensure almost 100% efficiency in μ^+ detection. On the other hand, a positron with the kinetic energy of 50 MeV passing through the same counter gives rise to about 500 photons. In this way, one can easily distinguish the pulses originating from different particles by setting up an appropriate threshold level on a discriminator for the muon to eliminate positrons and other background particles. In our setup the positron detectors have a thickness of 6 mm. A positron ($\langle E_{\rm kin}\rangle$ = 35 MeV) passing through such a counter produces about 2000 scintillating photons which is sufficient to guarantee a very high positron detection efficiency. Light produced by the particles is then guided to the photomultipliers (PMs) held well outside of the magnet and shielded with iron and μ-metal since the PM tubes do not work in high magnetic fields.

A good start event is defined logically as a muon with no prior muon with a pile-up time P and no post muon within the data gate D (S=TM$\cdot\overline{P}$ where TM indicates a triggered muon counter). A good stop event E=$\Pi \cdot \overline{P}$ consists of a single positron Π within the data gate time D. This ensures that the digitized time between the S and E signals corresponds to the decay of a single muon. The measured time range is limited by the data gate length D which is typically set at $\sim 5\tau_\mu$. A single slot VME based TDC (B980 TDC) is used to digitize the time. This module is an eight-channel TDC

with a timing resolution of 48.828 psec (50 ns/1024) and a full time range of 25.6 μsec (or 524288 bins per histogram). The reference and the sample events are separated according to the following logic. When a good event occurs and the μ_{in} (μ_{in} indicates that the internal muon counter is triggered) signal present then such an event was routed to the sample section of the histogramming memory module. The same sequence applies to the reference event given that the μ_{in} is not triggered. The 256 nsec delays are present in positron electronics in order to accumulate the events that occur *before* the muon is detected. This provides a convenient measure of the uncorrelated events (random background $\mathcal{B}$) observed in $\mu\mathcal{SR}$ experiments.

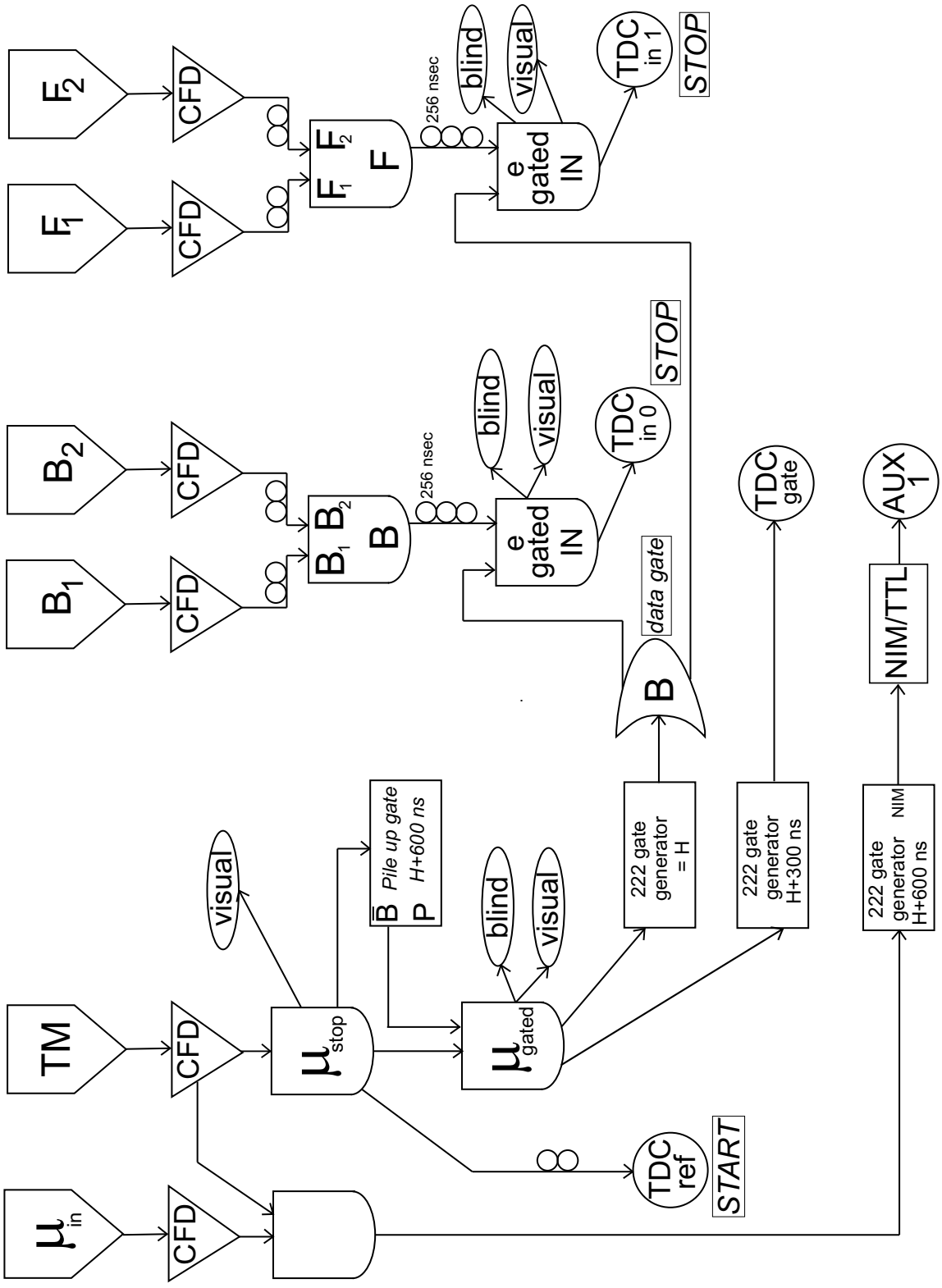

Figure 3.22: Electronics scheme with a multi-channel VME clock.

Chapter 4

HOPG Results and Discussion

4.1 Introduction

Graphite is a semimetal representing one of the four known carbon based crystal structures (see Fig. 4.23). Monocrystalline graphite may have either a hexagonal or a rhombohedral lattice. In the hexagonal lattice the atoms in one layer are exactly above or under the centres of the hexagons of the neighboring layers. Figure 4.24 illustrates the hexagonal graphite crystal structure. A right angle prism having a regular rhomb as its base serves as a unit cell for the graphite lattice and is described by the fundamental translation vectors $\boldsymbol{a}_1$, $\boldsymbol{a}_2$ and $\boldsymbol{a}_3$

$$\boldsymbol{a}_1 = (a_o, 0, 0),\ \boldsymbol{a}_2 = (a_o/2, \sqrt{3}a_o/2, 0),\ \boldsymbol{a}_3 = (0, 0, c_o) \tag{4.65}$$

where $|\boldsymbol{a}_1| = |\boldsymbol{a}_2| = a_o = \sqrt{3}$ and $|\boldsymbol{a}_3| = c_o = 6.7076$ Å. A unit cell of the hexagonal lattice contains 4 carbon atoms. The perfect graphite lattice is included in the spatial symmetry group $P6_3/mmc$ (or D^4_{6h}) [77].

HOPG (highly oriented pyrolytic graphite) has crystalline order extended to about 1 μm within a basal plane, and to about 0.1 μm along the $\boldsymbol{c}$ direction. HOPG has no long-range in plane alignment with the a-axes of adjacent crystallites randomly oriented. However, HOPG shows a high degree of c-axis alignment with misalignment angles of less than 1 degree between adjacent crystallites [78]. HOPG is the material of choice for fundamental studies when large size crystals are required.

Within a single layer the carbon atoms form a perfect hexagonal lattice which is a consequence of the equivalence of the three bonds of the carbon atoms with the three nearest neighbors in the layer. The described arrangement takes place in the sp^2-hybridization and is illustrated in Fig. 4.24. The carbon atoms in a plane are linked by directed σ-bonds, whereas the overlapping of unhybridized p-orbitals forming the isotropic π-bonds are mostly responsible for the semimetallic properties of graphite. The high mobility of π electrons causes a high electric in-plane conductivity. Thus at non-zero temperatures, the single graphite layer resembles in its properties a quasi 2D metal.

Graphite has a small free carrier concentration ($n_c = 3 \times 10^{18}$ cm^{-3}) and a correspondingly narrow conduction band width (0.023 eV). The low carrier density lifts the electron gas degeneracy in graphite [80],[81] and is responsible for the variation of the Fermi energy with temperature as shown in Fig. 4.25a. The galvanometric measurements [82] performed over a wide temperature range show a substantial increase in carrier density from 3×10^{18} cm^{-3} at 4.2 K to about 18×10^{18} cm^{-3} at RT (see Fig.4.25b). This increase is especially noticeable around 50 K, close to the graphite degeneracy temperature of 100 K. The temperature dependent Fermi level and the carrier density indicate that unlike normal metals where the degree of smearing of the Fermi surface is very small (~ 0.025 eV), in graphite the large number of free carriers can participate in the scattering process (see Fig. 4.26a). Because of the low carrier concentration ($2r_s \sim 81$ a.u.), one can also anticipate that a implanted muon is significantly underscreened in such a material compared to a normal metal. Consequently, the Thomas-Fermi wave vector $k_{\mathrm{T-F}} \propto n_c^{1/6}$ in graphite is only 0.34 Å^{-1} (see Eq. 1.6).

Graphite also has historic significance since it was the first material on which muon spin rotation was performed to confirm parity violation in weak interactions. However very little work has been done on it since that time. For example, it is known that the Knight shift at room temperature is unusually large [83]. There has also been a recent

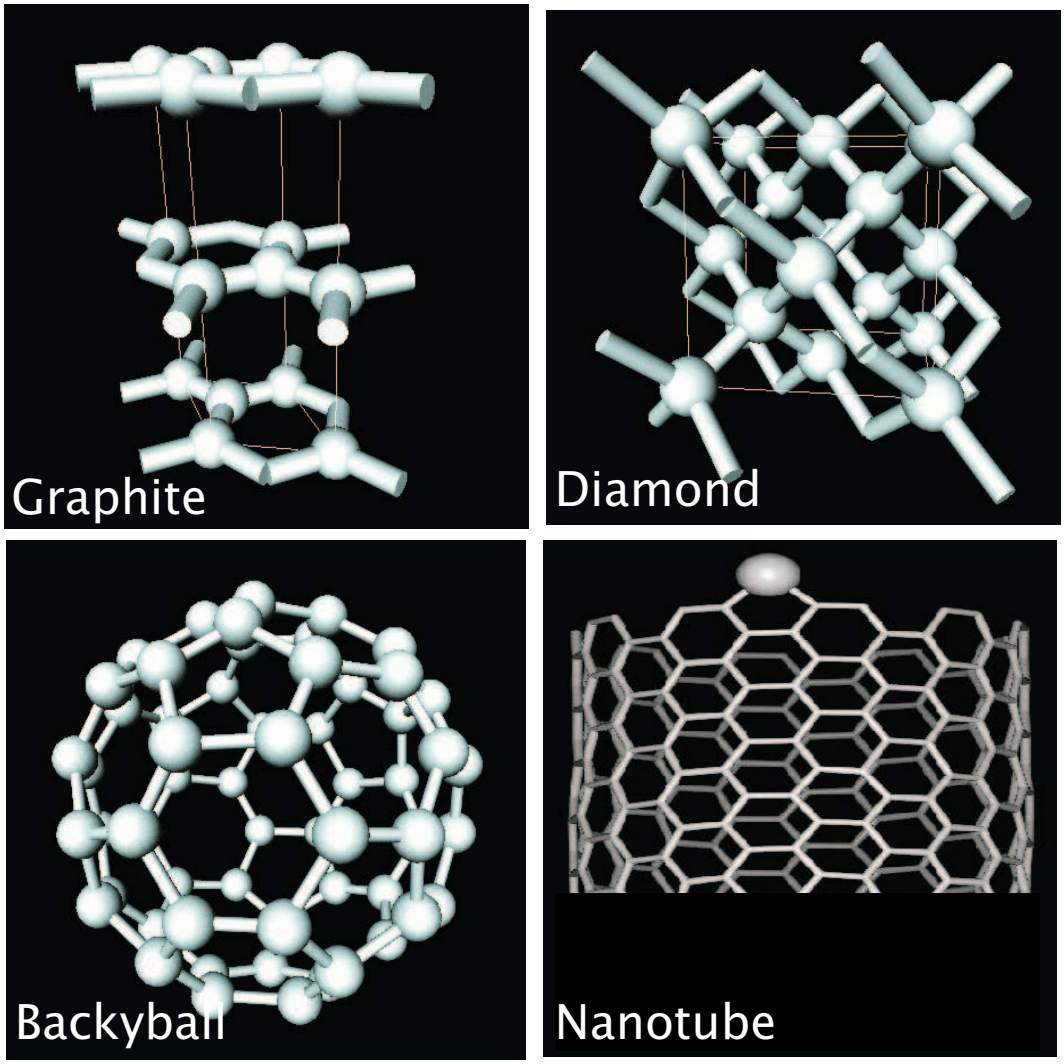

Figure 4.23: All presently known forms of carbon based structures: graphite, diamond, buckyball and nanotube (from Ref. [79]).

study of the spin relaxation state at high temperatures which we shall discuss later. Additional scientific motivation for understanding the behaviour of hydrogen in graphite is that related compounds are used as the negative electrode in lithium batteries. It has been reported [84],[85] that there is a strong correlation between lithium capacity and the content of hydrogen in graphitic compounds.

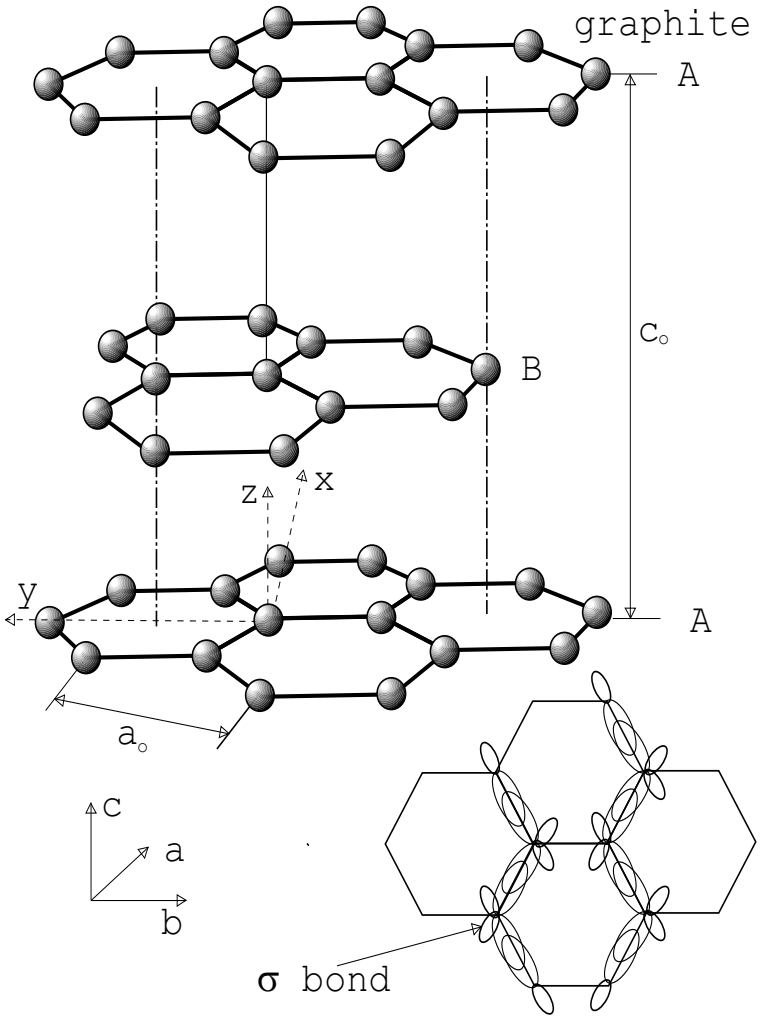

Figure 4.24: Top: A hexagonal crystal lattice of graphite. The letters A and B denote non-equivalent graphite layers. Bottom: An overlap of the carbon wave functions involved in $\sigma-$bonds formation.

4.2 Experiment

All measurements have been performed on the M20 or M15 beamlines at TRIUMF, which provide a beam of nearly 100% spin polarized positive surface muons with a mean momentum of 28 MeV/c. The spin polarization was rotated perpendicular to the axis

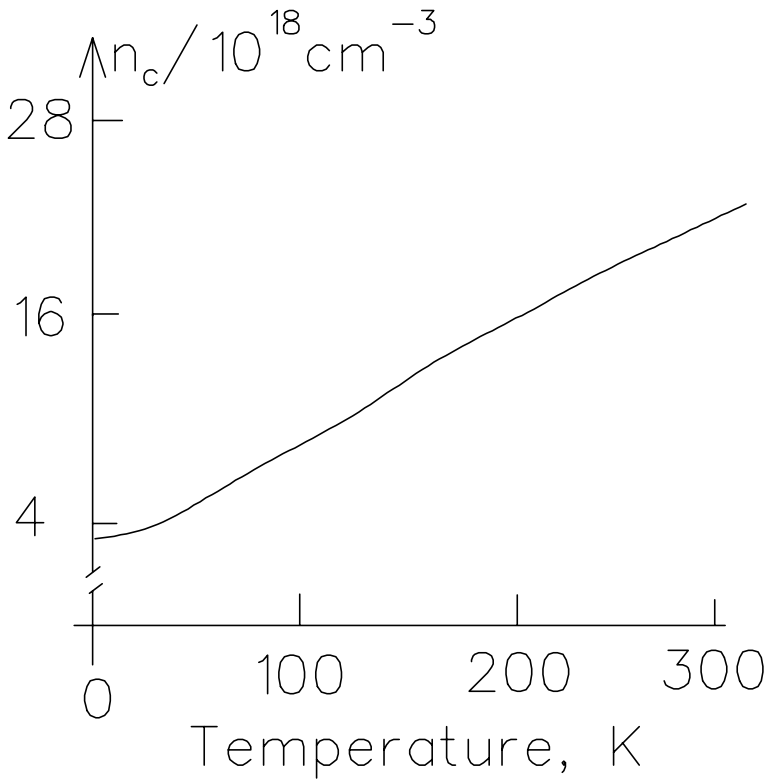

Figure 4.25: Concentration of free carriers as a function of temperature in graphite. From ref. [82]

of the superconducting solenoid and muon beam direction. The samples were cut from highly oriented pyrolytic graphite with ***c*** axis aligned to better than 2 degrees. A single piece or five pieces were used depending on whether the field was applied in parallel or perpendicular to the average ***c*** direction respectively. The magnitude of the applied magnetic field was chosen to be 1.45 T in order to attain the most accurate Knight shift.

4.3 Graphite Results

Figure 4.27 shows the temperature dependence of the measured Knight shift with respect to the silver reference measured with the magnetic field parallel and perpendicular to the

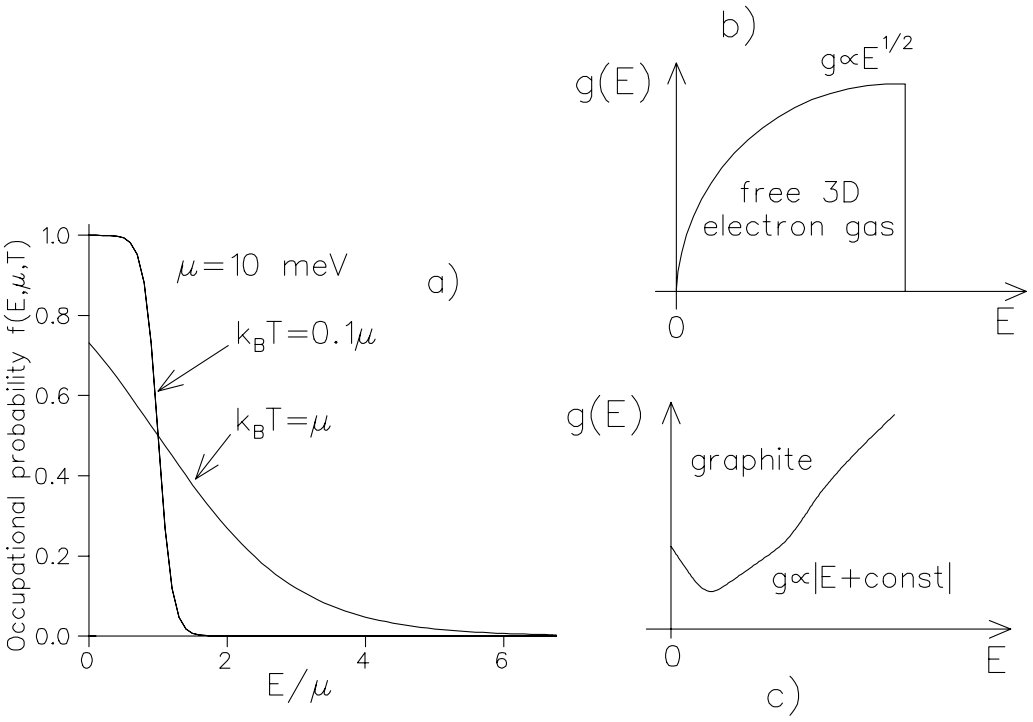

Figure 4.26: a) Fermi-Dirac distribution at low and high temperatures. The chemical potential is fixed at 10 meV. Unlike normal metals, graphite has a rather low degeneracy temperature of $T \approx$100 K. Figures b) and c) illustrate the difference between the density of states for a non-interacting 3D electron gas and graphite.

c axis of HOPG graphite. The magnitude of the Knight shift in the sample without correcting for bulk magnetization is defined according to the following formula:

$$\mathcal{K}_s = (B_s - H)/H \tag{4.66}$$

where B_s is the total magnetic field at the muon site in the sample and H is the external applied field. Subtracting the known Knight shift of the reference ($\mathcal{K}_r$) from both sides one obtains the Knight shift in the sample in terms of the measured or known quantities:

$$\mathcal{K}_s - \mathcal{K}_r = \frac{B_s - B_r}{H} \tag{4.67}$$

$$= \frac{f_s - f_r}{\gamma_\mu H} \tag{4.68}$$

$$\cong \frac{f_s - f_r}{f_r} \tag{4.69}$$

where $f_s = \gamma_\mu B_s$ is the observed muon precession frequency in the sample, f_r is the muon precession frequency in the reference, $\mathcal{K}_r$ is the known Knight shift in the reference (94 ppm) and where $\gamma_\mu H$ has been approximated by f_r. Several corrections to this

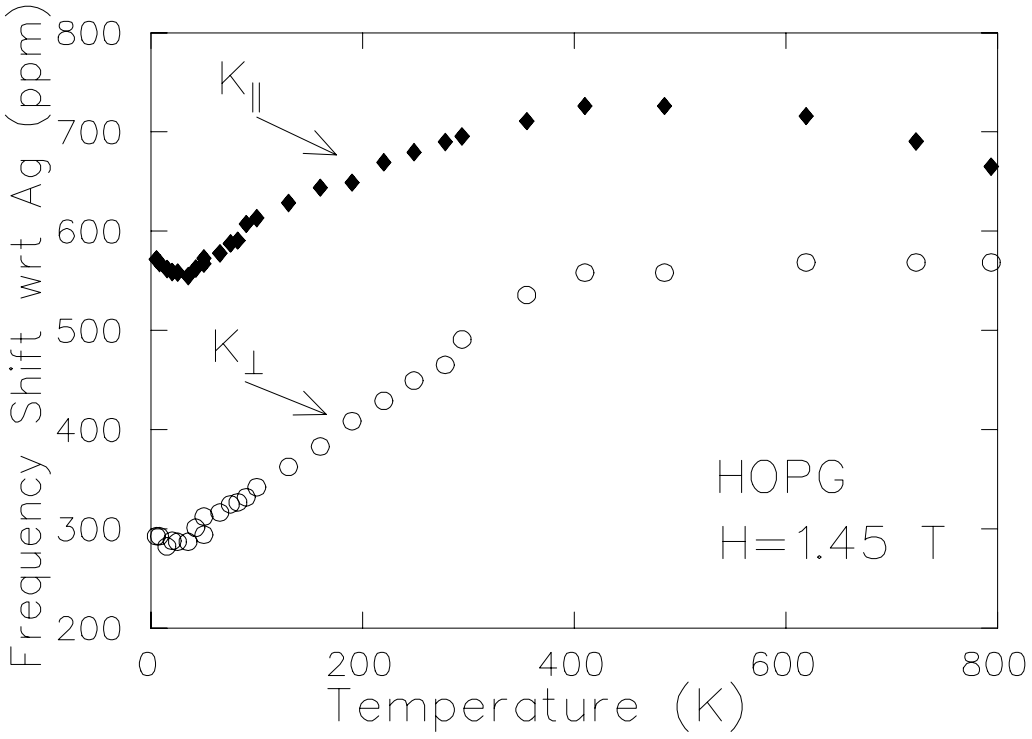

Figure 4.27: Shift in muon precession frequency in HOPG relative to Ag as a function of temperature in an applied magnetic field of 1.45 T. $\mathcal{K}_\parallel$ and $\mathcal{K}_\perp$ are defined by Eq. (4.72).

formula are needed. First, the external field at the reference and sample positions are not identical. This shift was determined to be about 7 ppm by mounting a second piece of silver at the sample position. Also, we are interested in the induced frequency shift due to the hyperfine interaction with the electrons (B_{hf}) whereas the total magnetic B_s field in Eq. (4.69) has other contributing terms originated from the bulk magnetization

of the sample [60]:

$$B_s = H + B_{hf} + B_{\rm dem} + B_L + B_{\rm dip} \tag{4.70}$$

where H is the applied magnetic field, $B_{\rm dem}$ is the demagnetization field, B_L is the Lorentz field, and $B_{\rm dip}$ is dipolar field from moments within the fictitious Lorentz sphere surrounding the muon. $B_{\rm dem}$ and B_L are the macroscopic contributions to the magnetic field and can be evaluated as follows:

$$B_{\rm dem} = -\mathcal{N}M, \qquad B_L = \frac{4\pi}{3}M, \qquad M = \chi H \tag{4.71}$$

where $\mathcal{N}$ is the geometry dependent demagnetization factor, M is bulk magnetization and χ is the total magnetic susceptibility of the sample. The dipolar field ($B_{\rm dip}$) can be evaluated numerically as a sum of $\sum_i \boldsymbol{b}_i(\boldsymbol{r}_\mu - \boldsymbol{r}_i)$ over the individual carbon atoms inside a Lorentz sphere of a sufficiently large radius (for more details see Sections 2.3.3 and 2.3.4). This term is opposite in sign to the sum of $B_{\rm dem}$ and B_L and is quite sensitive to the muon site. For example if one assumes that the muon adopts an interplane equilibrium position then the overall correction is just a few ppm for $\mathcal{K}_\parallel$ and almost zero for $\mathcal{K}_\perp$. On the other hand if the muon were located at a C-H bond length [86] ($\sim$1.19 Å) from a carbon atom there is a substantial correction for $\mathcal{K}_\parallel$ but almost none for $\mathcal{K}_\perp$ (see Fig. 4.28). We suspect the latter is most likely since the difference between $\mathcal{K}_\parallel$ and $\mathcal{K}_\perp$ has a temperature dependence close to that of the bulk magnetic susceptibility of graphite. In this case the Knight shift is almost isotropic and has a temperature dependence close to that of $\mathcal{K}_\perp$.

A few remarks about the Knight shift data in Fig. 4.28 are in order. First, the magnitude is anomalously large compared to normal metals considering the small Pauli spin susceptibility in graphite 0.016×10^{-6} emu/g. For example in a simple metal like Ag the ratio between the Pauli spin susceptibility and the muon Knight shift (+94 ppm) is about 270 times smaller than what is observed in graphite. The parallel Knight shift at

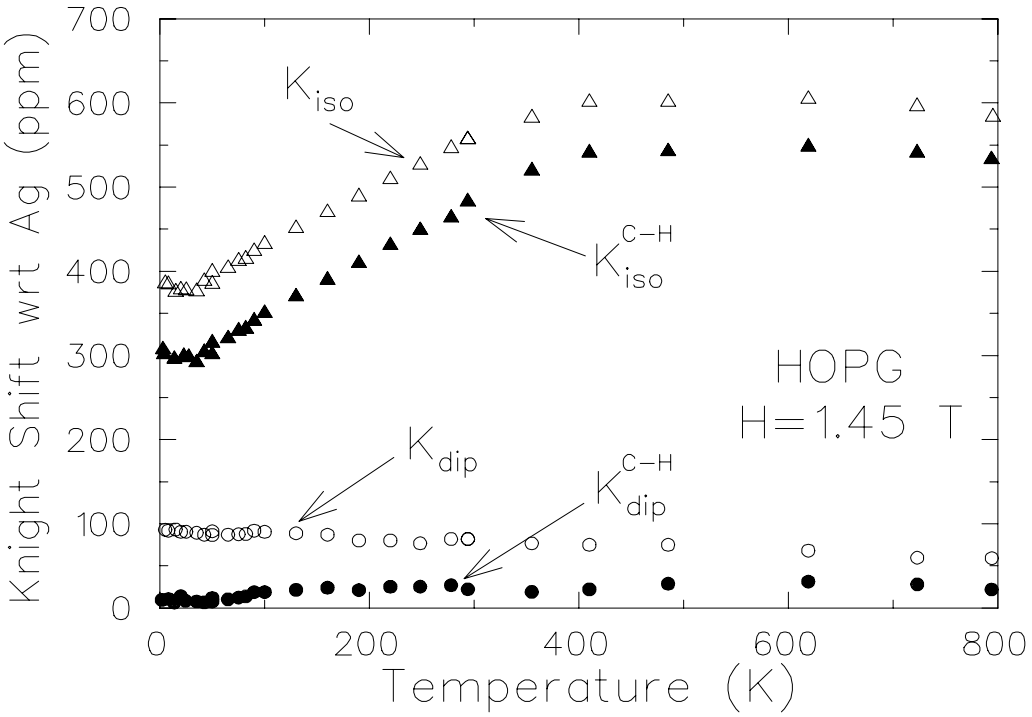

Figure 4.28: Temperature dependence of the isotropic $\mathcal{K}_{\rm iso}$ and axial or dipolar $\mathcal{K}_{\rm dip}$ parts of the muon Knight shift in graphite. The filled circles and triangles represent the corrected value of the Knight shift assuming that a muon is at the C-H bond distance from a carbon atom. The open circles and triangles represent the corrected Knight shift assuming that μ^+ is in the interplane position.

300 K is close to that of a previous measurement on a graphite single crystal [83] if the larger correction is made assuming a C-H bond length (about +250 ppm at RT). Second, the Knight shift has at most a small anisotropy in contrast with the bulk magnetic susceptibility where $\chi_\parallel/\chi_\perp \approx$49. These observations establish that the local electronic structure around the muon has a much different magnetic response than the conduction electrons of graphite. In particular the local spin susceptibility at the muon is orders of magnitude larger and far more isotropic than expected from just electrons at the Fermi surface. Last, the frequency shift displays an unusual temperature dependence since it

rises steadily with temperature above from about 20 K up to 500 K. Note that there is a slight upturn in $\mathcal{K}_{\parallel}$ below 20 K which we attribute to the influence from the dHvA oscillations which we discuss below.

This behaviour of the Knight shift in graphite is in a marked contrast to that seen in conventional free electron metals where $\mathcal{K}_{\mu}$ is temperature independent and proportional to the Pauli spin susceptibility. On the other hand the observed increase in the Knight shift with temperature is not predicted for a simple Kondo impurity where spin susceptibility is temperature independent below the Kondo temperature and falls like $1/(T+T_K)$ above T_K. Thus although there is good evidence for local moment formation the temperature dependence suggests that the behaviour is more complex than expected from a simple Kondo impurity. In order to elucidate the origin of the unusual temperature dependence of the Knight shift we may calculate the isotropic ($\mathcal{K}_{\rm iso}$) and the dipolar ($\mathcal{K}_{\rm dip}$) contributions as follows

$$\mathcal{K}_{\rm iso} = \frac{1}{3}(\mathcal{K}_{\parallel} + 2\mathcal{K}_{\perp}) \qquad \mathcal{K}_{\rm dip} = \frac{1}{3}(\mathcal{K}_{\parallel} - \mathcal{K}_{\perp}). \tag{4.72}$$

The linear part of the isotropic Knight shift was fit to the following model [87] which is valid for $T \ll T_K$ and $\mu_B H \ll k_B T$:

$$\mathcal{K}_{\rm iso}(T) = J_o(T)\Big(\frac{1}{2\pi T_K} - 0.433\frac{T^2}{T_K^3}\Big), \tag{4.73}$$

$$\text{where} \qquad J_o(T) = \beta(1+\alpha T) \tag{4.74}$$

The fit gives a scaling parameter β =3.0860(4), α =0.0032(4) K^{-1} and a Kondo temperature T_K of 1852(40) K (see Fig.4.29). Note that in order to fit the initial rise of $\mathcal{K}_{\rm iso}$ with temperature the Kondo coupling constant is allowed to vary as $1+\alpha T$. Additional evidence for this comes from $1/T_1$ (see below). The Korringa-like spin relaxation rate with the conduction electrons is also anomalous. Normally Korringa relaxation of muon polarization is too slow to be detectable on the $\mu\mathcal{SR}$ timescale. However, if there is a

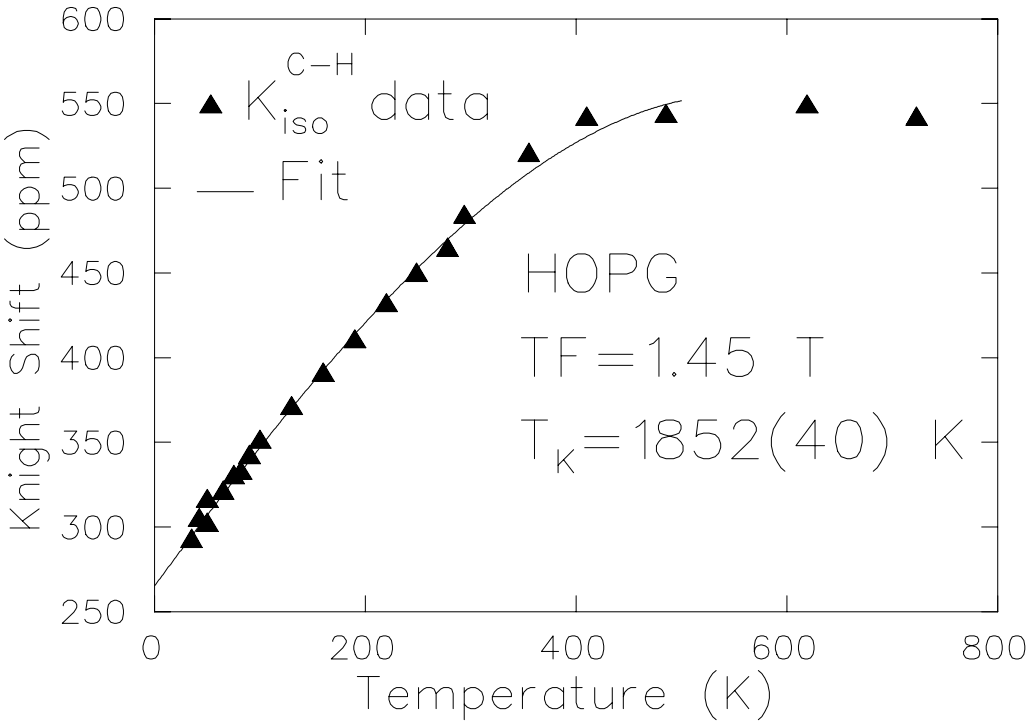

Figure 4.29: Temperature dependence of the isotropic $\mathcal{K}_{\rm iso}$ part of the Knight shift in graphite. A solid line is the best fit to Eq. (4.74); the parameters extracted from the fit are given in the main text. The limited dataset between 35 K and 485 K is used to fit the experimental data which corresponds to applicable temperature range T$\ll$T$_K$ for the model.

local moment as indicated by the large Knight shift, the muon spin relaxation should be enhanced by the indirect coupling between the muon spin and conduction electrons through the bound electron[18]. This is confirmed by the appreciable muon spin relaxation rate at 896 K (see Fig. 4.30). While $1/T_1$ is close to the detection limit at 295 K (see Fig 4.31) it increases steadily at higher temperatures in a non-linear fashion. Recall for nuclei in a normal metal the magnitude of $1/T_1$ is predicted to rise linearly with temperature (see Eq. 2.45). The observed relaxation rate in Fig. 4.30 rises faster than that predicted from Korringa relaxation [88] (see filled circles in Fig. 4.30). This breakdown

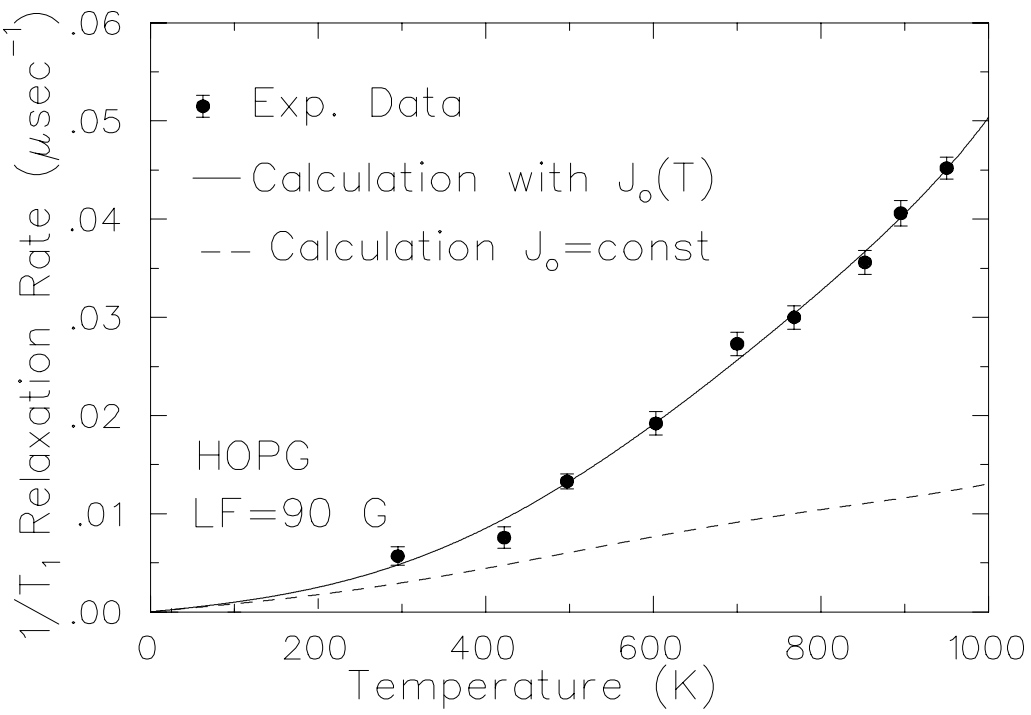

Figure 4.30: Temperature dependence of the longitudinal relaxation rate $1/T_1$ in pure graphite measured above RT. The solid and dashed lines represent our estimates.

of the Korringa law is attributed to a number of factors, the most important of which is the crossover from degenerate to non degenerate electron behaviour as k_BT exceeds about 100 K. In addition the fact that the Knight shift increases with temperature suggests that the coupling constant $J_o(T)$ increases with temperature as was indicated by the Knight shift . One can estimate $1/T_1$ in the first Born approximation without the usual assumption of degenerate statistics

$$1/T_1 = J_o^2(T) \int g^2(E) f(E,T)(1 - f(E,T)) dE \tag{4.75}$$

where $J_o(T)$ is proportional to the coupling constant between the muon and conduction electrons, $g(E)$ is the phenomenological density of states for graphite, and $f(E,T)$ is the Fermi-Dirac distribution with a Fermi energy (chemical potential) fixed at 23 meV. The

density of states is estimated as [89]:

$$g(E) = 4(0.092/\gamma_o^2)\,|E - 0.5(\gamma_2 + \Delta) + \text{constant}| \tag{4.76}$$

where γ_o, γ_2 and Δ (all in eV) are from band structure theory [90],[91] (also see Fig. 4.26c). Equation (4.75) predicts a non-linear behaviour of $1/T_1$ at high temperature as observed. This can be understood as follows: Recall the linear behaviour in normal metals arises from the fact that only the electrons with k_BT of the Fermi surface participate in the scattering due to Pauli blocking. However at high temperatures in graphite there are two new effects. First, a large fraction of the electrons are already involved in the scattering due to the crossover into non degenerate statistics. This weakens the temperature dependence. On the other hand the density of states is strongly energy dependent near the Fermi energy as can be seen from Eq. (4.76). This causes an increase in the overall number of free carriers available for scattering and a stronger than linear behaviour in T. In graphite these two opposing effects compete. The fit to equation (4.75) to a single temperature independent parameter J_o =0.1080(6) is shown as a dashed line in Fig. 4.30. The same model with a temperature dependent coupling constant $J_o(T) = J_o(1 + \alpha T)$ (J_o =1.4125(4) and α =0.0032(4) K^{-1}, where α is the same constant used to fit $\mathcal{K}_{\text{iso}}$) reproduces the experimental data rather well (see a solid line in Fig. 4.30).

4.4 Discussion on The Graphite Results

The results in Fig. 4.28 show that the isotropic part of the Knight shift dominates and grows with temperature whereas the dipolar part is much smaller and almost temperature independent. Given the evidence for a local moment we adopt a local picture of the center similar to what is used to describe muonium in semiconductors. Then the isotropic part of the Knight shift arises from a contact interaction with a $1s$ hydrogen-like orbital centered on the muon whereas the dipolar part is attributed to spin density

localized on the nearest neighbor carbon(s). The small hyperfine anisotropy required to explain the observed Knight shift anisotropy is similar to what is observed for a muonium substituted free radical or bond centered muonium in covalent semiconductors (such as GaAs [92]). In these cases the vast majority of the spin density rests on the neighboring atoms. Thus while the dipolar part of the Knight shift in graphite is much less than the isotropic part it is possible that most of the magnetic moment is not on the muon but rests on the neighboring carbon atoms. For example recent theoretical calculations for muonium interacting with a single graphene plane (see Fig. 4.31) predict that the hydrogen/muonium atom bonds to one carbon with the majority of the spin density on the six neighboring carbons. Of course this is a crude approximation to graphite since the muonium would be sandwiched between two graphene layers. Nevertheless, it is likely that a similar structure exists in graphite.

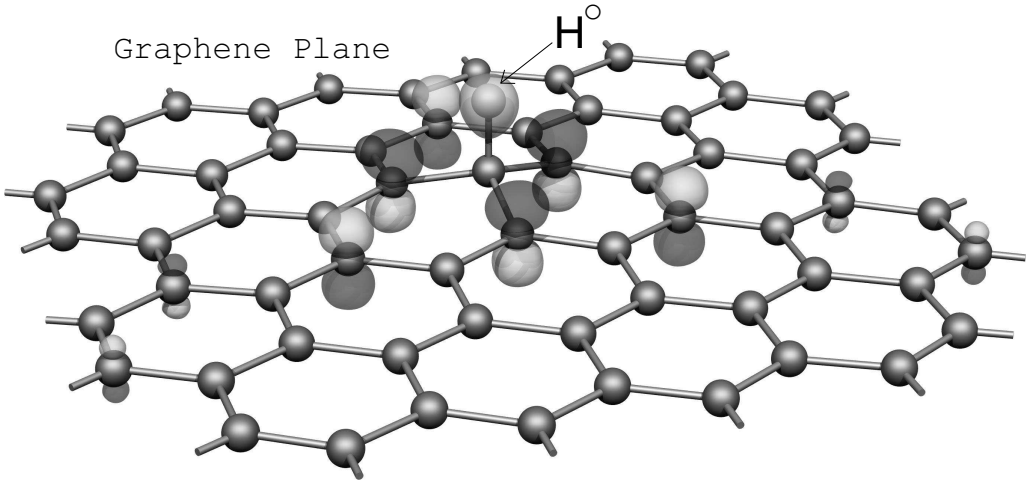

Figure 4.31: Molecular orbital simulation [93] on a single sheet of graphite reveals the existence of a loosely bound radical for a hydrogen atom. Note that the spin density is not on a single carbon but rather distributed among nearby carbon atoms.

Consider the temperature dependence of $\mathcal{K}_{\rm iso}$ which *increases* with temperature (see

Fig. 4.29). This is difficult to understand given the magnetic susceptibility of any local moment should decrease with temperature. We suggest that the increase in $\mathcal{K}_{\rm iso}$ and $1/T_1$ (see Fig. 4.30) is due to a small temperature induced change in the electronic structure. For example the contact interaction may increase with temperature as the C-Mu bond length increases. This can be understood since in the limit where the C-Mu bond is broken the contact interaction on the muon can increase to that of free muonium. Around 500 K the predicted $1/(T + T_K)$ decrease for a Kondo impurity behaviour takes over and $\mathcal{K}_{\rm iso}$ gradually decreases.

As mentioned previously $\mathcal{K}_{\parallel}$ displays a slight upturn at low temperatures below 20 K (see Fig. 4.27). In order to determine the origin of this we measured the bulk magnetic susceptibility in a SQUID magnetometer on the same sample of HOPG graphite. The magnetic field scan data taken at 3 K (see Fig. 4.32) show very pronounced dHvA oscillations caused by the periodic change in the density of states at the Fermi energy brought about by the changing energy spacing between Landau levels. To understand the possible influence of this on the temperature dependence of the Knight shift we measured the bulk susceptibility as a function of temperature for several applied fields shown as an inset of Fig. 4.32. As we expected the low temperature behaviour of the bulk susceptibility depends strongly on the magnetic field. At 1.45 T where our $\mu\mathcal{SR}$ measurements are performed the susceptibility shows an upturn at low temperatures whereas at 2.6 T it turns down. This is most likely the explanation for the low temperature feature seen in $\mathcal{K}_{\parallel}$ (see Fig. 4.27). Note that the effect is less noticeable for $\mathcal{K}_{\perp}$. This confirms our hypothesis that the observed frequency shift for a field parallel to the $\boldsymbol{c}$-axis is strongly influenced by the bulk magnetic susceptibility.

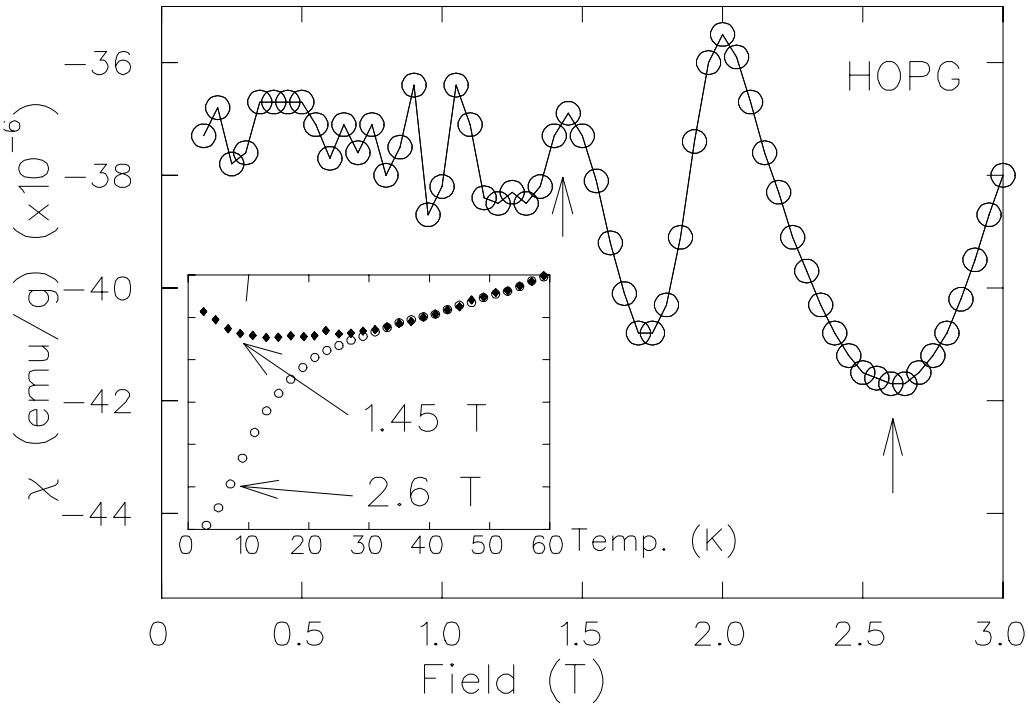

Figure 4.32: Oscillations of the magnetic susceptibility in pyrolytic graphite for $H\|$c and T=2.4 K. A magnitude of the applied magnetic field used for the muon Knight shift measurements is indicated by an arrow. The inset shows the low temperature part of the magnetic susceptibility in single-crystal graphite with $H\|$c taken in a magnetic field of 1.45 T and 2.6 T. The apparent change in the shape of the curves follows the de Haas-van Alphen oscillations.

4.5 $\mu\mathcal{SR}$ in Lithium Intercalated Graphite (LiC_6)

For comparison, additional $\mu\mathcal{SR}$ measurements were also taken on lithium intercalated compound LiC_6 which, unlike graphite, is a good metal. LiC_6 belongs to a class of materials in which Li ions form an ordered lattice in between the graphite sheets. Figures 4.33 and 4.34 illustrate the LiC_6 crystal structure in hard sphere approximation.

Angle-resolved photoemission results [94] show that the Li intercalant is fully ionized with one electron per Li atom transferred to the graphite layers which leads to the highly

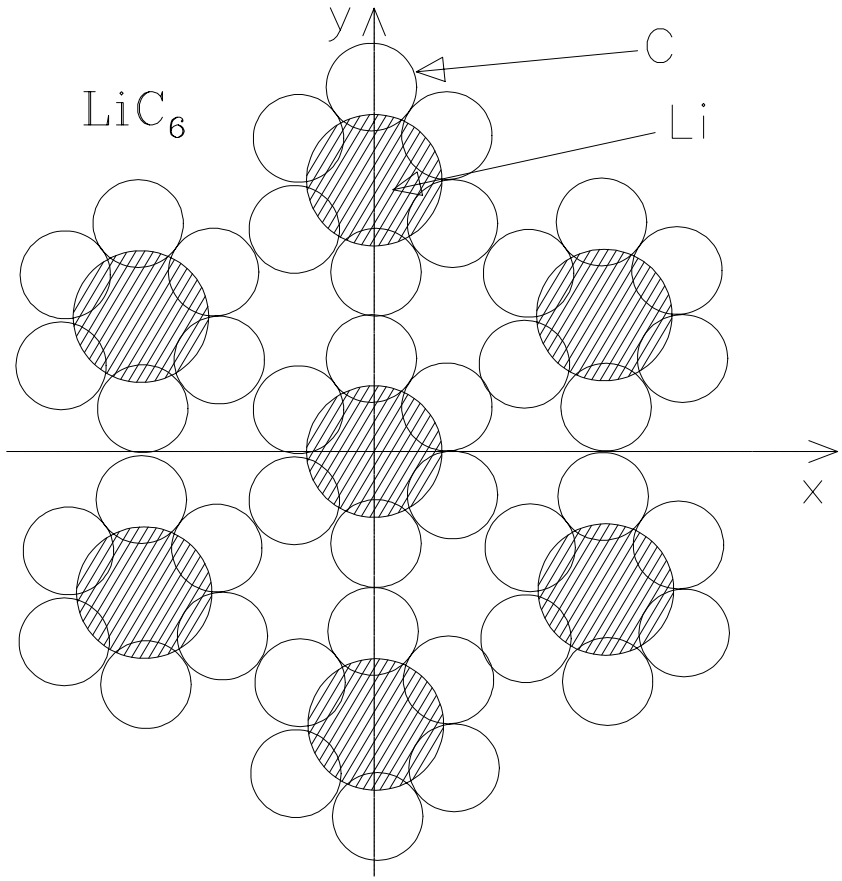

Figure 4.33: The $x-y$ cross-section of metallic Li and carbon C balls.

increased metallicity. Lithium intercalated compounds are extremely unstable in air and require special handling. In our case, the sample of LiC_6 was sealed in a small Al vessel equipped with a thin (50 μm) Kapton window to allow muons to enter the sample.

The muon Knight shift was measured in an external magnetic field of 1.45 T applied along the $\boldsymbol{c}$ axis (see Fig. 4.35). Note that the magnitude of the Knight shift is about -100 ppm and temperature independent. This is typical for simple metals where the Knight shift tracks the Pauli spin susceptibility[95]. As one might expect the increased carrier concentration from Li appears to destroy (or screen out) the local moment seen in pure

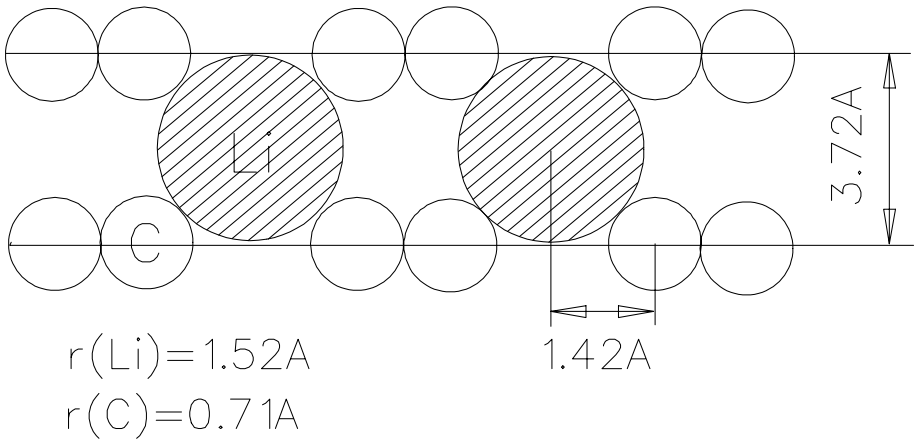

Figure 4.34: LiC_6: The close-packed arrangement in the $x-z$ plane.

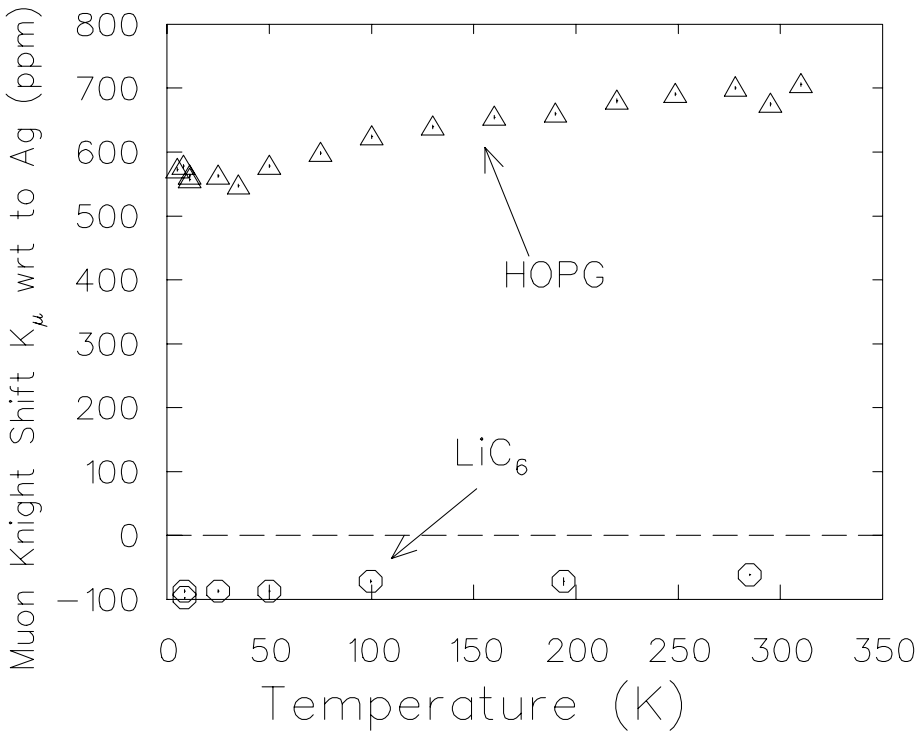

Figure 4.35: Temperature dependence of the muon Knight shift in LiC_6. For comparison, the same quantity measured in HOPG is represented by the open triangles.

graphite. The unusual feature in LiC_6 is the sign of Knight shift (*negative*) which implies that the spin density at the muon site is polarized opposite to the conduction electrons. This suggests that the muon is not in direct contact with the conduction electrons. One possibility is that the increased Fermi level favors the formation of a Mu^- ion which should bond to the Li^+. We know that the electronic band created by Li^+ [96] lies above the Fermi level throughout the whole Brillouin zone and is therefore unoccupied. However a local level created by a $MuLi^+$ may be below the Fermi surface and lead to a neutral Mu^-Li^+ complex. A similar mechanism has been proposed to explain a hydrogen complex formation in MC_8 (M=K, Rb and Sc) alkali-metal intercalation compounds [97]. This could explain the negative Knight shift. Thus, the external field likely polarizes the conduction electrons which are located primarily in the carbon plane. If there is little direct spin density on MuLi compound, then core polarization of the molecular orbitals for Mu^-Li^+ could lead to a net negative frequency shift. Note that similar core polarization effects lead to a negative contact interaction for bond centered muonium in silicon [98].

Finally, we note that as we expected the increased carrier concentration in LiC_6 dramatically influences the Knight shift compared to that of graphite. The high density of electrons leads to the substantially reduced frequency shift making it comparable to that of simple metals. The Knight shift relative to the χ_s^{Li} (*i.e.* $\mathcal{K}_\mu^{\mathrm{LiC_6}}/\chi_s^{\mathrm{Li}} \approx 48$ compared to $\mathcal{K}_\mu^{\mathrm{HOPG}}/\chi_s^{\mathrm{HOPG}} \approx 270$) is much reduced implying that the local moment is destroyed.

Chapter 5

CPC Results and Discussion

5.1 Unperturbed CPC Chain

In this chapter we present results of an experiment designed to test the predicted magnetic properties of perturbed one dimensional (1D) antiferromagnetic (AFM) S=1/2 chains characterized by a gapless spectrum of magnetic excitations. An ideal experimental system is one where the interaction between impurities can be neglected. The muon and the technique of muon spin rotation are naturally suited to this problem since there is typically only one muon (*i.e.* impurity) in a sample at any given time. Furthermore, the muon acts as both the impurity and a local probe of the magnetic susceptibility. We anticipate that the positively charged muon distorts the crystal lattice and thereby alters the Heisenberg exchange coupling between the magnetic ions in the vicinity of the muon. The resulting modification of the local susceptibility is detected in the muon frequency shift. It is worth noting that although the muon possesses a magnetic dipole moment, which couples to the magnetic moments on the spin chain, this direct magnetic interaction is negligible compared to the indirect effect of the Coulomb interaction.

Dichlorobis (pyridine) copper II ($CuCl_2{\cdot}2NC_5H_5$) or CPC is a linear S=1/2 antiferromagnetic chain. CPC has a monoclinic crystal structure and consists of coplanar units assembled into polymeric chains in which each Cu^{2+} ion is surrounded by four chlorine anions and two nitrogen atoms (see Fig. 5.36). Each Cu^{2+} ion has two closer $Cl^-_{(1)}$ ions (2.28 Å) located in the $a-b$ plane and two more distant $Cl^-_{(2)}$ ions (3.05 Å) located on

adjacent planes in the chain. The angle between the copper–chlorine and the copper–nitrogen bonds is close to 90^o. The in-chain copper ions are separated by a distance of 3.57 Å, compared to the interchain nearest-neighbor separation of $b = 8.59$ Å[99]. This large interchain separation assures a high degree of one-dimensionality. In order to verify the effect of the μ^+ perturbation and to test the theory we first measured the bulk susceptibility without the perturbing influence of the muon. A precise value of J was extracted by performing d.c. susceptibility measurements in fields of 0.9 T and 1.45 T. The data were fit to the theory of Eggert and Affleck [52] and a value for the interchain coupling J was obtained. Although the theoretical procedure was developed to deal with the impurity problem, the unperturbed case is also an important test of the theory. Within experimental limits the measured susceptibility $\chi(T)$ is close to that reported earlier [100],[101] but more accurate. Note that all previously reported results were analyzed on a finite size chain using numerical methods within the conventional Bonner-Fisher (B-F) model based on the following Hamiltonian [102]

$$\mathcal{H}_{B-F} = \sum_i (-2J\mathbf{S}_i \cdot \mathbf{S}_{i+1} + g\mu_B H S_i^z) \tag{5.77}$$

where J is the nearest neighbor exchange coupling constant, $\boldsymbol{S}_i$ is the spin on the i^{th} site, g is the isotropic $g-$factor, μ_B is the Bohr magneton and $\boldsymbol{H}$ is the applied magnetic field. In the past, the Bonner-Fisher model has proven to be adequate in analyzing experimental data at high temperature and in the vicinity of a characteristic peak observed in the chain susceptibility. However, the B-F model is known to fail in the low T limit. This breakdown was first observed in d.c. susceptibility measurements in the early 1970's [101]. The procedure developed recently by Eggert, Affleck and Takahashi correctly describes the experimental data in a wide range of temperatures including the low temperature region where the theory predicts a divergent slope of $\chi(T)$ as $T \to 0$ and an inflection point at $T \sim 0.087J$ [103],[104]. Figure 5.37 illustrates the d.c. susceptibility of CPC

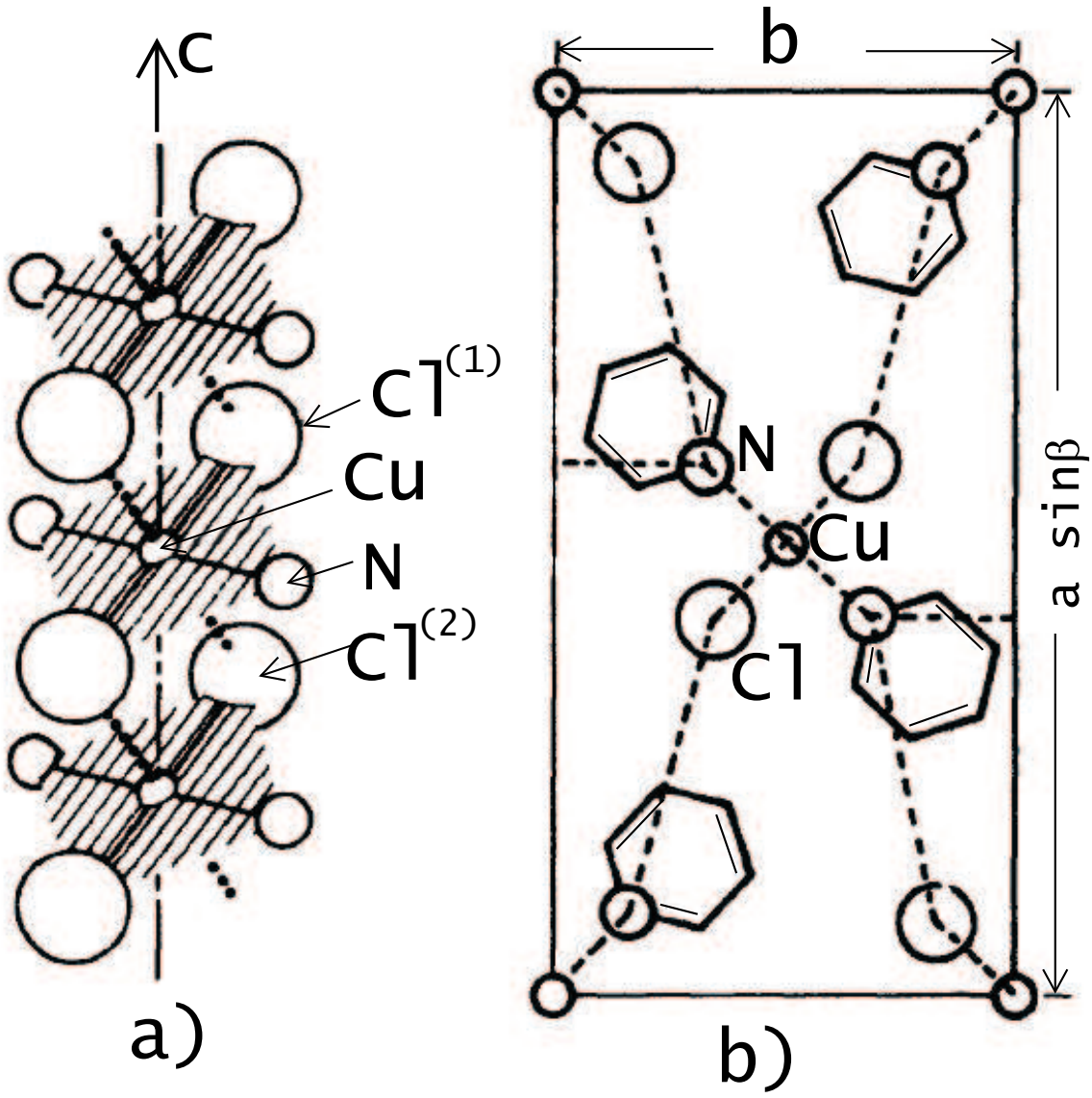

Figure 5.36: CPC crystal structure. a) The chain of Cu^{2+} ions. b) The CPC unit cell as viewed down along the $\boldsymbol{c}$ axis ($a = 17$ Å , $b = 8.59$ Å and $\beta = 91^o.52'$). Dashed lines indicate the superexchange paths. From ref. [100].

along with the best fit curve according to the Eggert–Affleck calculation. The measured bulk susceptibility follows a Curie law at high temperatures, goes through a maximum

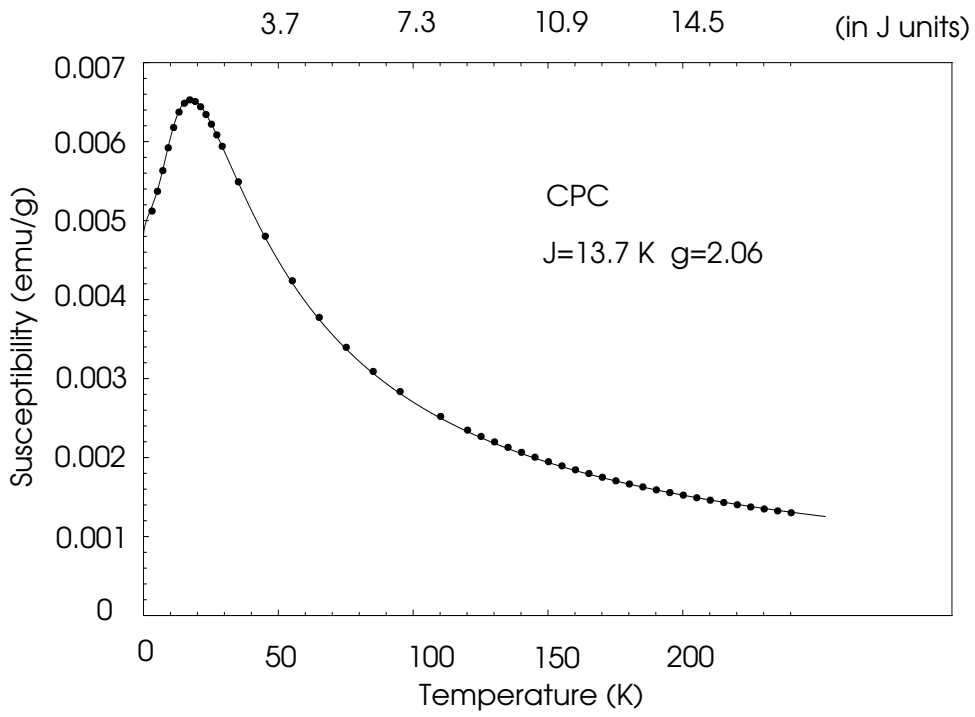

Figure 5.37: Theoretical QMC fit to the SQUID CPC data: The data were taken in an applied magnetic field of 1.45 T. The fit is provided courtesy of S. Eggert.

around T=17.8 K and then the slope starts increasing again. As seen in Fig. 5.37, the theoretical fit to the experimental data is excellent over the entire temperature range with deviations of less than 1%. The best fit yields a value of the intrachain coupling J of 13.7(1) K and a $g-$factor of 2.06(1). The estimate of J is about 2% larger than previously reported. This extremely good fit constitutes strong evidence for the validity of the Eggert–Affleck procedure.

5.2 $\mu\mathcal{SR}$ in CPC – Effect of Perturbation

Frequency shift measurements on a powdered sample of CPC have been performed on the M20 beamline at TRIUMF by utilizing the same Knight shift apparatus described

in Section. 3.1. The magnitude of the applied magnetic field $|\boldsymbol{H}| = 0.4$ T was chosen to provide a good balance between the muon frequency shift and the amplitude of the $\mu\mathcal{SR}$ signal. To determine the number of signals (n) and their approximate frequency values, Fast Fourier transforms of the time spectra have been performed. Then the data have been fitted in the time domain to a TF relaxation function with a Gaussian envelope $G_{xx}(t)$:

$$N_i(t) = N_i^o\{\exp(-t/\tau_\mu)[1 + \sum_{j=1}^{n} A_i^{o(j)} G_{xx}^{(j)}(t)\cos(\omega_\mu^{(j)} t + \phi_i^{(j)})] + \mathcal{B}_i\}. \tag{5.78}$$

First we will describe the low temperature region because it is only at the low temperatures that the impurity effects become important. As seen in Figs. 5.38 and 5.39, the spin precession signal and the Fast Fourier Transform (FFT) of the precession signal revealed a significant difference in muon behavior between low and high temperature regions. At temperatures above 100 K one observes a narrow single frequency line. As the temperature decreases, the line becomes noticeably broadened and eventually splits into several frequency lines as the temperature drops below 25 K (see Fig 5.39). The best least-square fits show that there are two fast relaxing signals (labeled as FR1 and FR2) with small asymmetries $A_\mu^{\mathrm{FR1}} = 6\%$ and $A_\mu^{\mathrm{FR2}} = 3\%$ and one slow relaxing signal (SR) with a large asymmetry $A_\mu^{\mathrm{SR}} = 15\%$. The temperature dependence of the relaxation rates of the FR1, FR2 and SR signals is shown in Fig. 5.40. It is clear that muons occupy more than one interstitial site. Above 30 K the line merges due to the decreasing local spin susceptibility.

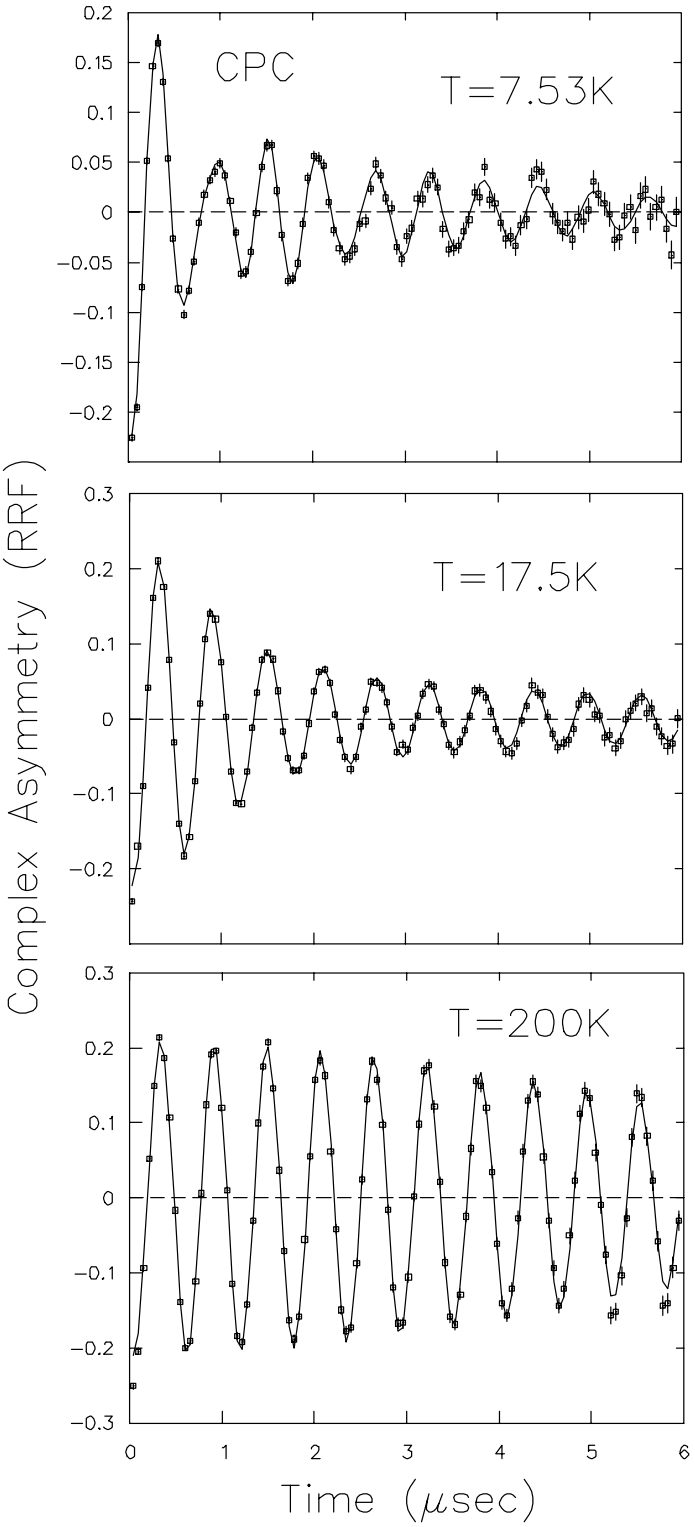

Figure 5.38: The CPC signal measured at the temperatures of 7.53 K, 17.5 K and 200 K. The complex asymmetry time spectrum is displayed in the Rotating Reference Frame (RRF=53 MHz).

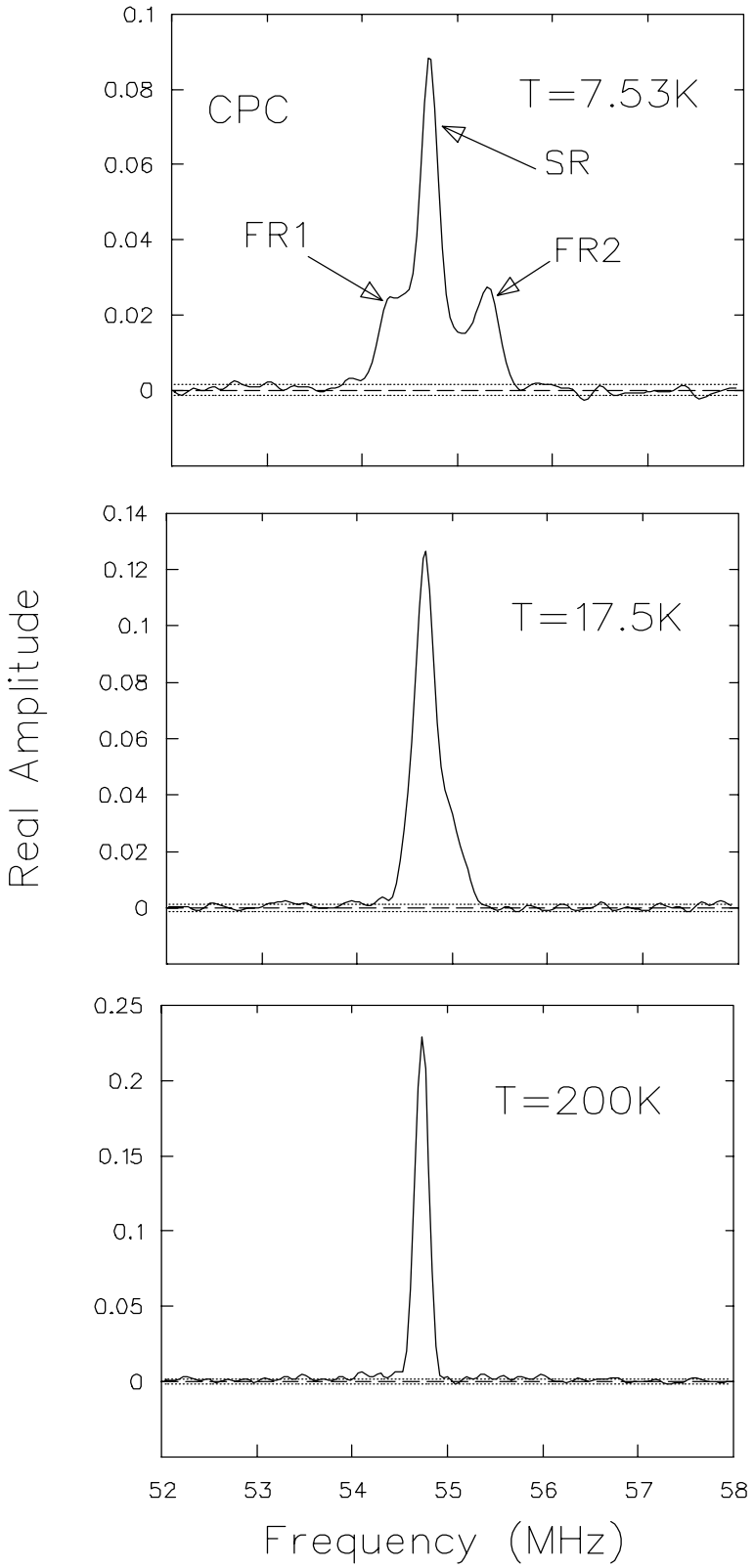

Figure 5.39: The evolution of the FFT transforms with temperature.

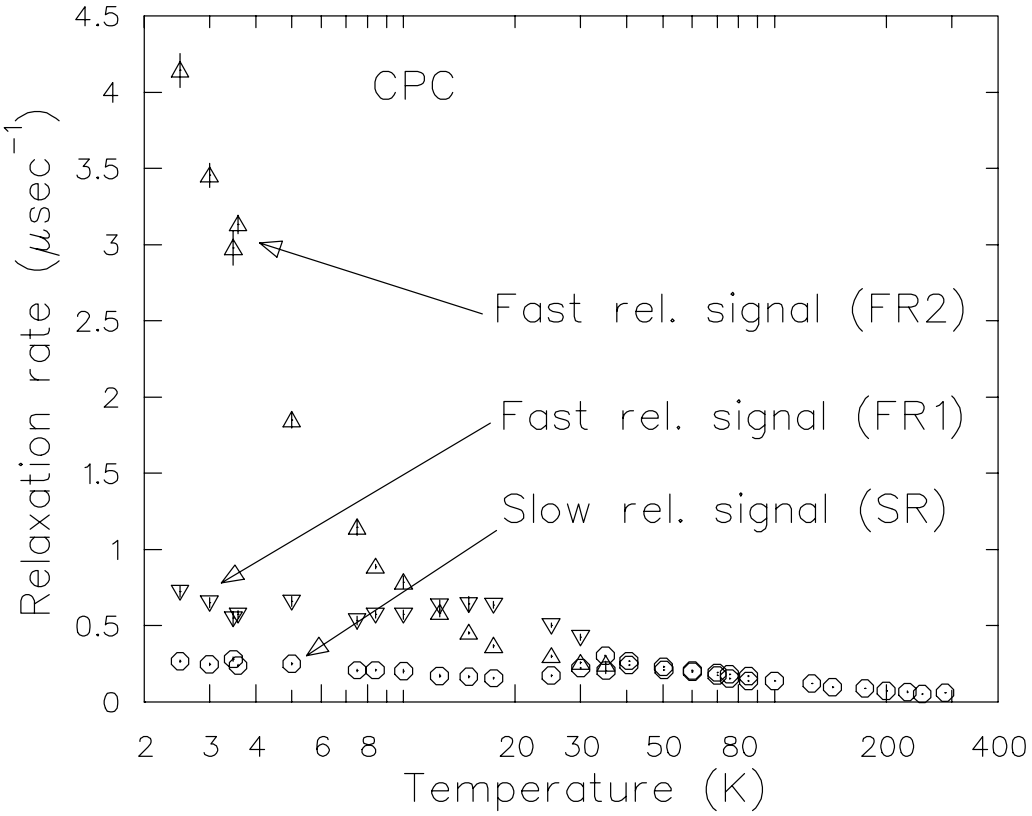

Figure 5.40: Relaxation rates as a function of temperature in CPC.

Figures 5.41, 5.42 and 5.43 show the temperature dependence of the measured frequency shifts of the fast relaxing signals and the slow relaxing signal observed at low temperatures. A few important observations are in order. First, since the experiment was performed on a powdered CPC sample, the dipolar interaction contributes only to the linewidth and thus the frequency shift should depend only on the contact interaction (see Eq. (1.23)). The contact hyperfine interaction in CPC is attributed to either, direct overlap of the wave function tails of the magnetic electrons with the μ^+, or to the super–transferred hyperfine field arising from covalency effects. Considering the localized nature of the Cu^{2+} *d*-orbital, the latter effect is more likely. The implanted muon can

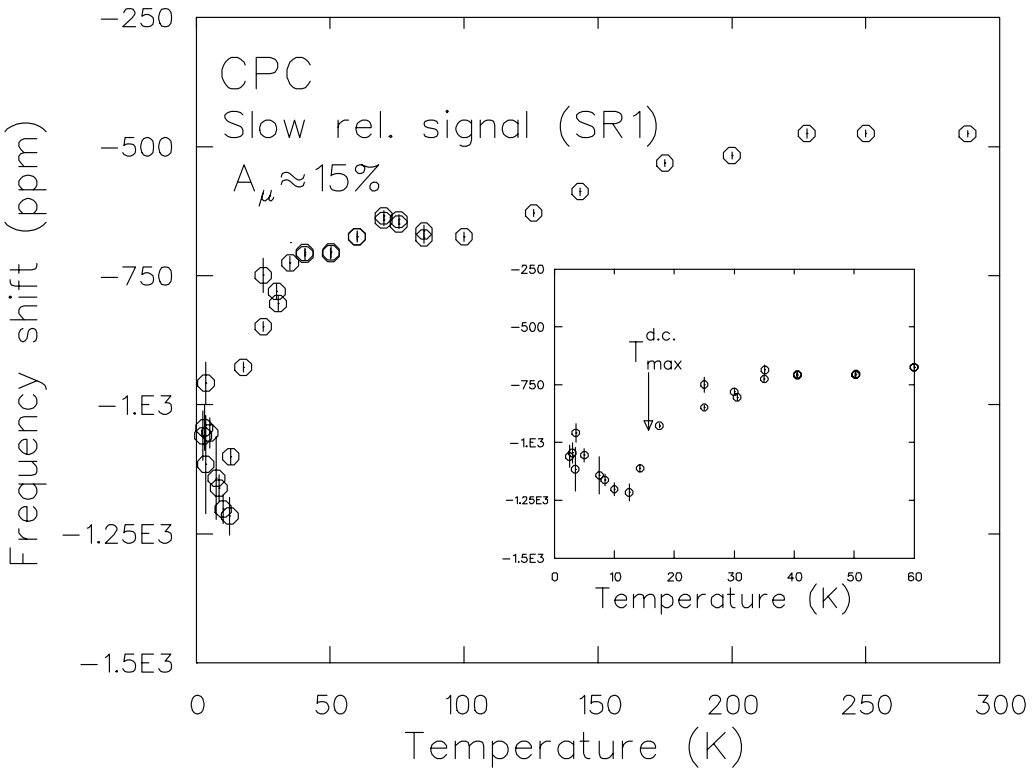

Figure 5.41: Temperature dependence of the frequency shifts in CPC measured in an applied magnetic field of 0.4 T. An inset shows the low temperature part of the frequency shift of the slow relaxing (SR) signal.

be viewed as competing for bonding to the Cl^- ions, which leads to some degree of spin density transfer onto the μ^+. This perturbation may not necessarily be exactly at the link–symmetric location, but should still significantly affect the exchange path between two of the copper ions. In CPC one can identify at least three inequivalent sites where the muon may localize. Two of them can be associated with a muon interacting with two chlorine ions (*i.e.* Cl^-–μ^+–Cl^-). Note that a similar complex has been identified in a variety of ionic solids containing fluorine [50]. The two fast relaxing signals (FR1 and FR2) can be attributed to these two sites where muons locked between two chloride ions. The temperature dependence of the Knight shift of the FR1 and FR2 signals suggests

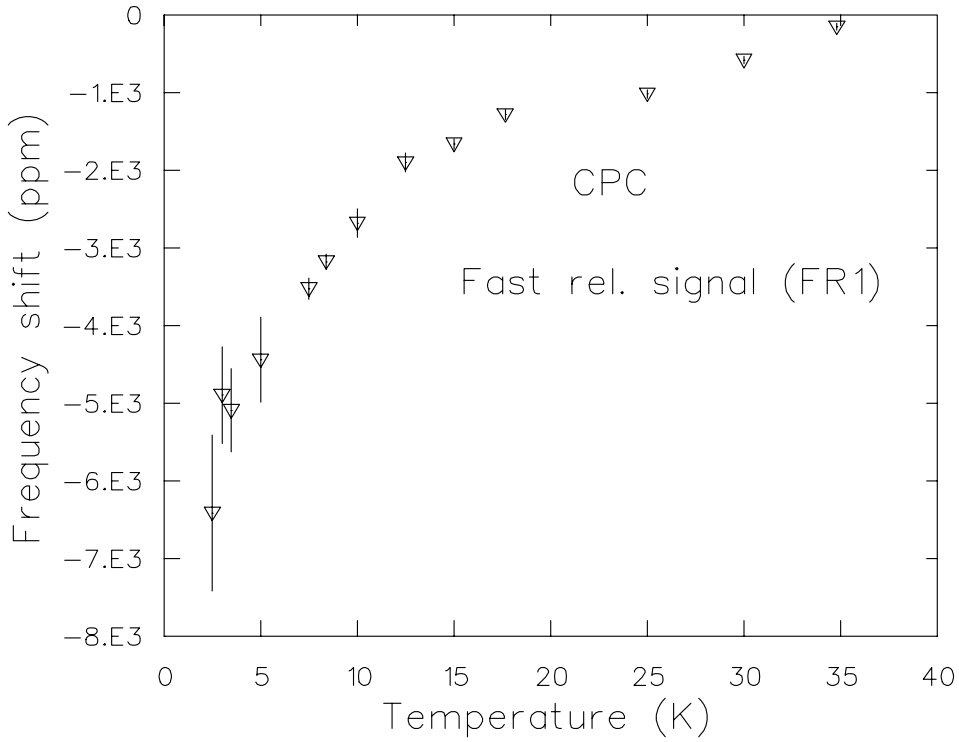

Figure 5.42: Temperature dependence of the frequency shift of FR1 $\mu\mathcal{SR}$ signals in CPC.

that the muon perturbation at these lattice sites is strong. In contrast, the frequency shift of the SR signal practically follows the bulk magnetic susceptibility and displays a minimum around 14 K in the vicinity of a characteristic peak seen in the d.c. susceptibility (see inset in Fig. 5.41). This indicates that the SR signal is attributed to the muons whose influence on the chain is weak. Considering the large interchain distance in CPC (8.59 Å), one can speculate that it is likely that the SR signal is associated with the muons thermalized in the space between chains, far from the super-exchange path.

Second, there is qualitative agreement with the E-A theory in that the muon charge *significantly* disturbs the coupling between Cu^{2+} ions. This is clear from the fact that the temperature dependence of the muon frequency shift of the FR1 and FR2 $\mu\mathcal{SR}$ signals

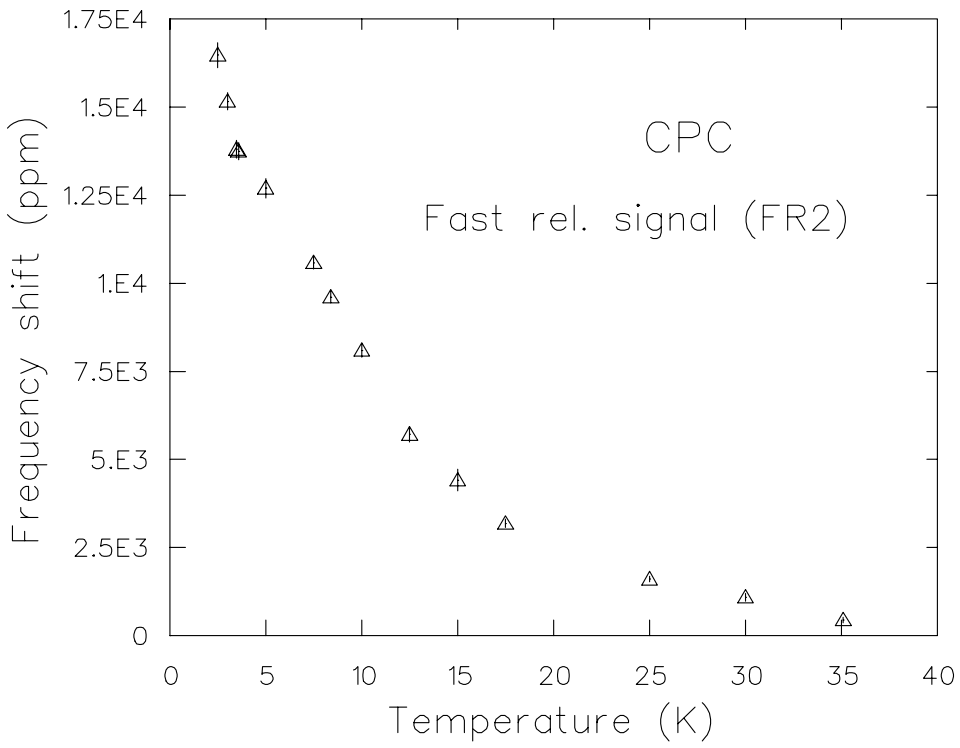

Figure 5.43: The low temperature part of the frequency shift of the FR2 $\mu\mathcal{SR}$ signal in CPC.

is substantially different from that of the unperturbed CPC susceptibility. Also, the characteristic maximum (at about 18 K) seen in the unperturbed d.c. susceptibility is completely 'washed out', which is clear evidence for a strong perturbation. Among the unexpected features is the small dip around 100 K (see Fig. 5.41). One of the possible explanations is a muon transition into the sites discussed above.

Finally we note that, although the precise location(s) of the muon and the resulting symmetry of the chain distortion are still unknown, we have definitely observed a dramatic impurity effect. In particular, the local spin susceptibility around the muon in CPC deviates significantly from the bulk magnetic susceptibility at least for two of the muon sites, as predicted by the Affleck–Eggert theory.

Chapter 6

Summary

6.1 Graphite and LiC_6

In conclusion, we have studied the local electronic structure for muons implanted in HOPG graphite by means of the muon Knight shift measurements from 3 K to 900 K. The measured Knight shift in graphite is unusually large and temperature dependent which indicates the formation of a local moment. This is in contrast to normal metals where the Knight shifts are small and scale with the Pauli susceptibility. The isotropic part of the Knight shift is much larger than the dipolar part and rises with temperature. We have interpreted these results in terms of a local model where the spin density is predominantly on the neighboring carbons, which is similar to what is observed in some semiconductors (*e.g.* GaAs). This is also consistent with recent molecular orbital calculation for hydrogen on a single graphite sheet. The increase in the isotropic part of the Knight shift, which measures the contact interaction, indicates that the local electronic structure changes with temperature. At very low temperatures the observed upturn in $\mathcal{K}_{\|}$ is attributed to the the bulk susceptibility, which is influenced by the De Haas–van Alphen effect at low T.

In addition, the measured muon spin relaxation rate $1/T_1$ is unusually large and deviates from the Korringa relation for metals. This is attributed in part to a strong energy dependence in the density of states coupled with a small Fermi energy. A phenomenological model based on the specific graphite density of states and the temperature dependent

coupling constant $J(T)$ describes the $1/T_1$ data rather well. The large extracted value of the Kondo temperature , T_K=1852(40) K, is consistent with the strong-coupling limit picture. It is also worth noting that the conventional Kondo problem has only been extensively studied for normal metals where k_BT is much less than E_F, *i.e.* the degenerate electron gas. The situation in graphite is quite different: there, E_F is comparable to k_BT.

Similar muon precession measurements on LiC_6 which is more metallic, produced a small, negative and temperature independent Knight shift. The reduced value of the Knight shift is expected because of the increased carrier concentration in LiC_6 that appears to screen out the local moment at a much higher temperature than in pure graphite. The observed negative frequency shift is unusual for normal metals and is possibly attributable to core polarization of a Li^+Mu^- complex. A similar mechanism has been proposed to explain a hydrogen complex formation in related intercalated compounds KC_8 and RbC_8.

6.2 CPC

The local magnetic susceptibility around the muon in quasi the one dimensional spin 1/2 antiferromagnetic chain compound CPC has been investigated using muon spin rotation/relaxation. A recent theory by Eggert and Affleck (EA) predicts that the local magnetic susceptibility near an impurity in a spin 1/2 chain is dramatically different compared to the bulk magnetic susceptibility. This behaviour is attributed to the gapless spectrum of magnetic excitations and may be considered the magnetic equivalent of the Kondo effect in normal metals. There is considerable experimental evidence that in most two and three dimensional magnetic compounds the muon impurity has a negligible effect *i.e.* the local magnetic susceptibility tracks the bulk susceptibility. To verify

the EA theory, we compared the local spin susceptibility as measured by the muon spin precession frequency with the bulk magnetic susceptibility measured in a SQUID magnetometer. The theoretical fit to the experimental unperturbed susceptibility data is excellent over the entire temperature range. The best fit yields a value of the intrachain coupling constant of $J = 13.7(1)$ K and a g-factor of 2.06(1). This estimate of J is about 2% larger than previously reported.

In CPC the measured muon frequency shift shows a dramatic difference between the local and bulk magnetic response. The Fast Fourier transforms display complex multiple frequency spectra present at low temperatures below 30 K. This probably represents localization of the muon at magnetically inequivalent sites. The characteristic maximum around 18 K seen in the unperturbed d.c. susceptibility is completely washed out in the frequency shift of the fast relaxing signals, which is clear evidence for a strong perturbation and thus supports the validity of the Eggert–Affleck theory.

Bibliography

[1] P. Debye and E. Hückel, *Z. Phys.* **24**, 185 and 305 (1923).

[2] J. P. van Dyke et al., *Nucl. Mater.* **67-70**, 533 (1978).

[3] N. F. Lane and R. C. Cloney, *Nucl. Mater.* **69-70**, 582 (1978).

[4] Z. P. Popovic and M. J. Scott, *Phys. Rev.* **B5**, 2109 (1972).

[5] E. Zaremba, L. M. Sander, H. B. Shore and J. H. Rose, *J. Physics* **F7**, 1763 (1977).

[6] P. Jena and K. S. Singwi, *Phys. Rev.* **B17**, 3518 (1978).

[7] F. Guinea and F. Flores, *J. Phys.* **C13**, 4137 (1980).

[8] J.K. Norskov, *Phys. Rev.* **B20**, 446 (1979).

[9] M. Manninen et al., *Solid State Comm.* **23**, 795 (1977).

[10] K. H. Chow, B. Hitti and R. F. Kiefl, in *Identification of Defects in Semiconductors*, edited by M. Stavola (Academic Press, New York, 1998).

[11] B. Bech Nelsen, K. Bonde Nelsen and J. R. Byberg, *Materials Science Forum* **143-147**, 909 (1994).

[12] Yu. V. Gorelkinskii and N.N. Nevinnyi, *Physica* **B**, 155 (1991).

[13] K. H. Chow, R. F. Kiefl, B. Hitti, T. L. Estle and R. L. Lichti, *Phys. Rev. Lett.* **84**, 2251 (2000).

[14] C. Rizzuto, *Rep. Prog. Phys.* **37**, 147 (1974).

[15] G. Gruner, *Adv. Phys.* **23**, 941 (1974).

[16] A. C. Hewson, *The Kondo Problem to Heavy Fermions* (Cambridge University Press, Cambridge, 1993).

[17] P. Nozieres, *J. Low Temp. Phys.* **17**, 31 (1974).

[18] W. A. MacFarlane et al, *Phys. Rev. B* **58**, 1004 (1998).

[19] W. A. MacFarlane, R. F. Kiefl et al., *Hyp. Int.* **105**, 77 (1997).

[20] R.F. Kiefl and T.L. Estle, in *Hydrogen in Semiconductors* 547 , Ed. by J. Pancove and N.M. Johnson (Academic Press, New York, 1990).

[21] O. Hartman, *Hyp. Int.* **4**, 828 (1978).

[22] T.M.S. Johnston et al., *Hyp. Int.* **106**, 71 (1997).

[23] N. W. Ashcroft and N. D. Mermin, *Solid State Physics* (1976) pp. 340-345 (Harcourt Brace College Publishers).

[24] J. Lindhard, *Kgl. Danske Videnskab. Selskab Mat.-Fys. Medd.*, **28** (1954).

[25] J. Freidel, *Phil. Mag* **43**, 153 (1952).

[26] W. Kohn and L. J. Sham, *Phys. Rev.* **140**, A1133 (1965).

[27] C.O. Almbladh, U. von Barth, Z.D. Popovic and M.L. Stott, *Phys. Rev.* **B14**, 2250 (1976).

[28] P. W. Andreson, *Phys. Rev.***124**, 41 (1961).

[29] J. Kondo, *Prog. Theor. Phys.***28**, 846 (1962).

[30] J. Kondo, *in Kinzoku Densi Ron* (in Japanese), Shokabo, Tokyo, (1983).

[31] L. G. Wieglson, *Rev. Mod. Phys.* **47** 773; *Nobel Symposia* **24**, 68 (Academic Press New-York, 1974)

[32] P. Noziéres, *J. Low Temp. Phys.* **17**, 31 (1974).

[33] K. Yamada, *Prog. Theor. Phys.* **53**, 970 (1975); *Prog. Theor. Phys.* **54**, 316 (1975).

[34] P. W. Wiegmann , *Sov. Phys. Phys. JETP Lett.* **31**, 392 (1980).

[35] N. Andrei, *Phys. Rev. Lett.* **45**, 379 (1980).

[36] E. S. S⊘rensen and I. Afleck, *Phys. Rev.* **B53**, 9153 (1996).

[37] V. Borzikin and I. Affleck, *Phys. Rev. Lett.* **45**, 379 (1980).

[38] P. Jena anf K. S. Singwi, *Phys. Rev.* **B17**, 3518 (1978); *Phys. Rev.* **B17**, 301 (1978).

[39] D. E. Ellis and B. Lindgren, *Hyper. Interact.* **17-19**, 279 (1984).

[40] S. Estreicher and P. F. Meier, *Phys. Rev.* **B27**, 642 (1983).

[41] A. Mainwood and A. M. Stoneham, *J. Less-Common Met.* **4**, 271 (1976).

[42] Adachi et al., *J. Phys. Soc. Japan* **44**, 1039 (1978).

[43] C. D. Gellat et al., *Phys. Rev.* **B17**, 1940 (1978).

[44] M. Gupta and A. J. Freeman, *Phys. Rev.* **B17**, 3029 (1978).

[45] B. M. Klein and W. E. Pickett, *Phys. Rev.* **29**, 1597 (1984).

[46] A. Luther and I. Peschel, *Phys. Rev.* **B12**, 3908 (1975).

[47] S. Eggert and I. Affleck, *Phys. Rev.* **B46**, 10 866 (1992).

[48] I. Affleck et al., *J. Phys.* **A22**, 511 (1989).

[49] S. Eggert and I Affleck, *Phys. Rev. Lett.* **75**, 934 (1995).

[50] J. H. Brewer, S. R. Kreitzman et al., *Phys. Rev.* **B33**, 7813 (1986).

[51] D. Clarke, T. Giamarchi and B. Shraiman, *Phys. Rev.* **B48**, 7070 (1993).

[52] S. Eggert and I. Affleck, *Phys. Rev.* **B46**, 10866 (1992); S.Eggert, UBC Ph.D. Thesis (unpublished).

[53] E. Leader and E. Predazzi, *An Introduction to Gauge Theories and Modern Particle Physics: Electroweak Interactions, the 'New Particles' and the Patron Model*, vol. 1, (Cambridge Univ. Press, 1995).

[54] D. E. Groom et al. (Particle Data Group), *Eur. Phys. Jour.* **C15**, 1 (2000) (URL: http://pdg.lbl.gov).

[55] G. Woan, *The Cambridge Handbook of Physics Formulas*, p.9, (Cambridge Univ. Press, 2000).

[56] J. Chappert and R. I. Grynszpan, *in Muons and Pions in Material Research*, p.35 (1984).

[57] V. Storchak, J.H. Brewer, G.D. Morris, D.J. Arseneau and M. Senba, *Phys. Rev.* **B59**, 10559 (1999).

[58] G. H. Eaton and S. H. Kilcoyne *in Muon Science: Muon Physics, Chemistry and Materials*, p.11, (The Scottish Universities Summer School in Physics, 1999).

[59] J.L. Beveridge, J. Doornbos, D.M. Garner, D.J. Arseneau, I.D. Reid and M. Senba, *Nucl. Instr.& Meth.* **A240**, 316-322 (1985).

[60] A. Schenck, *Muon Spin Rotation Spectroscopy: Principles and applications in solid state physics* 128, (Adam Highler Ltd. Bristol and Boston, 1985).

[61] M. H. Levitt, *Spin Dynamics: Basics of nyclear magnetic resonance* 128, (John Willey and Sons, Ltd., 2001).

[62] A. Abragam, *The Principles of Nuclear Magnetism*, (Oxford Univ Press, London, 1970).

[63] P. W. Anderson, *J. Phys. Soc. Jpn.* **9**, 316 (1954).

[64] R. Kubo and K. Tomita, *J. Phys. Soc. Jpn.* **9**, 888 (1954).

[65] R. Kubo and T. Toyabe, *In: Magnetic Resonance and Relaxation (ed. R Blinc)*, (North- Holland, Amsterdam, 1967).

[66] Y. J. Uemura et al., *Sol. State. Commun.* **31**, 731 (1979).

[67] S. F. J. Cox, *J. Phys. C: Solid Stae Phys.* **20**, 3187 (1987).

[68] A. Schenck and F. N. Gygax, in *Handbook of Magnetic Materials* Vol. **9**, 57 (Ed. by Buschow K H J (Elsevier, Amsterdam, 1995).

[69] J. Winter, in *Magnetic Resonance in Metals* (Oxford: Clarendon, 1971).

[70] M. Manninen, *Phys. Rev.* **B27**, 53 (1983).

[71] F. N. Gygax et al., *L. Less-Common Metals* **101**, 97 (1984).

[72] O. Hartmann et al., *Hyp. Int.* **6**, 47 (1979).

[73] A. Schenck, *Helv. Phys. Acta* **54**, 471 (1982).

[74] P. G. Akishin and I. A. Gaganov, *J. of Magn. and Magn. Mat.* **110**, 175 (1992).

[75] J. A. Osborn, *Phys. Rev.* **67**, 351 (1945).

[76] J. Chakhalian, R.F. Kiefl et al., *Hyper. Interact.* **106**, 245 (1997).

[77] R. W. G. Wyscoff, *in Crystal Structure* vol. **1**, (1960).

[78] A. W. Moore , *Chemistry and Physics of Carbon* vol. **17**, (New York: Dekker, 1981).

[79] URL: http://www.ill.fr/dif/3D-crystals.

[80] V.V. Kechin, A.I. Likhter and G.M. Stepanov, *Sov. Phys.-Solid State* **10**, 987 (1969).

[81] S. Ono and K. Sugihara, *J. Phys. Soc. Jpn.* **21**, 861 (1966).

[82] R.O. Dillon, I.L. Spain and J.W. McClure, *J. Phys. Chem. Solids* **38**, 635 (1977).

[83] F.N. Gygax, A. Hintermann, A. Schenck, W. Studer and A.J. Van Der Wal, *Hyp. Int.* **15-19**, 383 (1983).

[84] Tao Zheng, J.S. Xue and J.R. Dahn, *Chem. of Mat.* **8**, 389 (1996).

[85] J.R. Dahn, Tao Zheng, J.S. Xue and Yinghu Liu, *Science* **270**, 590 (1995).

[86] Dake Yu et al., *Chem. Phys.* **142**, 229 (1990).

[87] V.I. Mel'nikov, *JETP Lett.* **5**, 414 (1982).

[88] J. Korringa, *Physica* **XVI**, 601 (1950).

[89] J.C. Slonczewski and P.R. Weiss, *Phys. Rev.* **109** (1958).

[90] J.W. McClure, *Phys. Rev.* **108**, 612 (1957).

[91] J.W. McClure, *Phys. Rev.* **119**, 606 (1960).

[92] S.F.J. Cox and M.C.R. Symons, *Chem. Phys. Lett.* **126**, 516 (1986).

[93] S. F. J. Cox et al., *J. Phys.: Condens.Mat.* **13**, 2169 (2001).

[94] M.S. Dresselhaus and G. Dresselhaus, *Adv. in Phys.* **30**, 255 (1981).

[95] M. Manninen, *Phys. Rev.* **B27**, 53 (1983).

[96] N.A.W. Holzwarth, S. Rabii and L.A. Girifalco, *Phys. Rev.* **B15**, 5190 (1978).

[97] K. Ichimura, E. Takamura and M. Sano, *Synth. Met.* **40**, 355 (1991).

[98] R.F. Kiefl et al., *Phys. Rev. Lett.* **60**, 224 (1988).

[99] J. D. Dunitz, *Acta Crystallog.* **10**, 307 (1957).

[100] W. Duffy, Jr. et al., *Phys. Rev.* **5**, 2220 (1974).

[101] K. Takeda, S. Matsukawa and H. Haseda, *J. Phys. Soc. Japan* **30**, 1330 (1971).

[102] J. C. Bonner and M. E. Fisher, *Phys. Rev.* **B51**, A640 (1964).

[103] S. Eggert, I. Affleck and M. Takahashi, *J. Phys. Rev. Lett* **73**, 332 (1994).

[104] S. Eggert, *Phys. Rev.* **53**, 5116 (1996).

[105] S. Eggert and I. Affleck, *Phys. Rev. Lett.* **75**, 934 (1995).

[106] E. Holzschuh et al, *Hyper. Interact.* **8**, 77 (1980).

[107] E. Holzschuh et al, *hyper. Interact.* **8**, 615 (1981).

[108] E. Holzschuh et al, *Phys. Rev.* **B27**, 5295 (1983).

[109] C. Boekema, *Hyper. Interact.* **17-19**, 305 (1984).